LUND UNIVERSITY

Microsphere-based modeling of electro-active polymers

Thylander, Sara

2016

Document Version:
Publisher's PDF, also known as Version of record

Link to publication

Citation for published version (APA):
Thylander, S. (2016). *Microsphere-based modeling of electro-active polymers*. [Doctoral Thesis (compilation), Lund University]. Department of Construction Sciences, Lund University.

Total number of authors:
1

Microsphere-based modeling of electro-active polymers

Doctoral Dissertation by

Sara Thylander

Till mamma, pappa, Ulrika & Maria

Preface

This thesis is the result of my Ph.D studies conducted at the Division of Solid Mechanics at Lund University. I would like to take this opportunity to thank the people who have helped me during this time and in my work. First of all I would like to thank my supervisor, Prof. Andreas Menzel, for giving me this opportunity and for sharing his knowledge and expertise (which seems to be endless) with me. I would also like to thank my co-supervisor, Prof. Matti Ristinmaa, whose support was crucial for me in completing this task.

I am extremely grateful to have had the privilege to share my time at the division with a great group of colleagues. A special thank you is given to Prof. Mathias Wallin for introducing me to the topic of Finite Element modeling and who has continued to inspire me throughout the years. My experimental work has relied on the expertise and enthusiasm of Assoc. Prof. Stephen Hall, the skills of our technician Zivorad Zivkovic as well as on great aid from Ph.D Jonas Engqvist. To my fellow Ph.D-students, to whom I owe hours of discussions and help, I extend my deepest gratitude. A special thank you goes to Johan Hektor, whose happy and easygoing nature has proved very helpful to me.

Related to my time spent at the Technical University of Dortmund, I am grateful for the welcoming atmosphere, as well as for help in my work, provided by the staff of the Division of Mechanics.

I am also, of course, very thankful for my friends outside of work for distracting me from work as much as possible and for making me laugh during stressful times. A special thanks goes to Julius Kratzer who has been the unfortunate main recipient of much of my work-related anxiety and frustration over the years. Finally, I would like to thank my family, to which I dedicate this work, for all their love and support.

Malmö, September 2016

Sara Thylander

Abstract

This thesis deals with constitutive models of electro-active polymers used for simulations of electromechanically and time-dependent processes. The modeling framework is based on statistical mechanics arguments combined with a numerical averaging technique, referred to as the microsphere formulation. A microsphere model, originally proposed for modeling of rubber, is in this work extended to capture the non-linear, time-dependant and electrostrictive behaviour of dielectric elastomers. The developed model is shown, through various homogeneous deformation and finite element examples, to produce physically sound results.

Dielectric elastomers represent a subgroup of electroactive polymers wherein the deformation, upon an applied electric field, is caused by the Coulomb forces between two compliant electrodes on the surfaces of the elastomer. Dielectric elastomer actuators (DEAs) offer advantages over more traditional materials in applications where soft, lightweight and noiseless actuators capable of large strains are needed. Existing applications based on DEAs include for example loudspeakers, tunable lenses and energy harvesting generators.

The non-linear and viscous behaviour inherent in DEAs impose drawbacks in relation to applications. Consequently, the possibility to predict and control these phenomena is crucial for future development of DEA applications. For this reason, the proposed microsphere model is calibrated to a common DEA material. Representative boundary value problems, chosen to mimic existing DEA applications, are then elaborated using the calibrated model. Furthermore, the possibility of controlling the viscous effects is successfully achieved.

Lastly, in order to gain a deeper understanding of the material behaviour, experimental investigations of a typical dielectric elastomer are performed. These investigations study the electromechanically coupled and time-dependent response of an acrylic-based DEA through full-field deformation measurements by use of digital image correlation.

Populärvetenskaplig sammanfattning

Elektroaktiva polymerers (EAPs) främsta egenskap är deras förmåga att kunna omvandla elektrisk energi till mekanisk energi (och vice versa). Den typ av EAPs som behandlas inom ramen för detta arbete kallas för dielektriska elastomerer och är en undergrupp av elektroniska elektroaktiva polymerer. De karakteriseras av en väldigt låg elastisk styvhet, kapabel till stora elastiska deformationer, och av en hög energidensitet. En dielektrisk elastomer placerad mellan två elektroder som kopplas till en strömkälla kommer komprimeras på grund av den elektriska fältstyrka som byggs upp mellan elektroderna, då materialet inte leder ström. Eftersom materialet dessutom anses vara inkompressibelt kommer ytan vinkelrätt mot det elektrisk fältet att öka. Dielektriska elastomerer aktiverade på detta sätt kan ersätta mer tradionella material inom flera högteknologiska områden såsom justerbara linser, mikropumpar, högtalare och som generatorer i system som utvinner förnyelsebar energi. Dess likheter med muskler, som också reagerar på elektriska signaler med deformation och är väldigt elastiska, har gett dem smeknamnet artificiella muskler.

Denna avhandling berör till största delen matematiska modeller av dielektriska elastomerer och tillhörande simuleringar av olika randvärdesproblem. Även experiment på dielektriska elastomerer under inverkan av elektromekaniskt kopplade laster har utförts. Inom ramen för modellering har arbetet koncentrerats kring den så kallade mikrosfär-metoden. Utnyttjande av mikrosfär-metoden möjliggör användandet av en-dimensionella fria energier, baserade på till exempel statistisk mekanik. Via en medelvärdesbildning över ytan på mikrosfären är det möjligt att transformera de en-dimensionella storheterna till tre-dimensionella motsvarigheter som representerar responsen av kontinuumet. Metoden, som tidigare använts med framgång på gummiliknande material under mekanisk last, har i denna avhandling utökats för att inkorporera elektromekaniska kopplingar. Metoden visades ge tillförlitliga resultat även för dielektriska elastomerer utsatta för ett elektriskt fält. För att anpassa modellen till specifika val av dielektriska elastomerer har experiment, både gjorda inom ramen för detta arbete och rapporterade i litteraturen, använts för att kalibrera och förfina modellen ytterligare.

List of appended papers

This doctoral thesis is based on the following papers:

Paper A

S. Thylander, A. Menzel and M. Ristinmaa (2012)
An electromechanically coupled micro-sphere framework: application to the finite element analysis of electrostricitve polymers.
Smart Materials and Structures 21 (2012), 094008 (10 pp)
Smart Material and Structures 22 (2013), 039501 (2 pp)

Paper B

S. Thylander, A. Menzel and M. Ristinmaa (2016)
A non-affine electro-viscoelastic microsphere model for dielectric elastomers: Application to VHB 4910 based actuators.
Journal of Intelligent Material Systems and Structures (2016)
doi: 10.1177/1045389X16651157 (13pp)

Paper C

S. Thylander, A. Menzel and M. Ristinmaa (2016)
Towards control of viscous effects in acrylic-based actuator applications.
Smart Materials and Structures 25 (2016), 095034 (13 pp)

Paper D

S. Thylander, A. Menzel, M. Ristinmaa, S. Hall and J. Engqvist
Measurements of the electro-viscoelastic response of an acrylic elastomer using three-dimensional surface digital image correlation.
To be submitted for publication

Own contribution

The author of this thesis has taken the main responsibility for the preparation and writing of all papers. In all papers, the development of the model and analysis of results have been conducted in collaborations with the co-authors. The numerical implementations has been made by the main author. Planning and preparation of experiments in paper D have been done in collaboration with the co-authors while the experimental measurements have been carried out by the main author.

Contents

1 Introduction

Electroactive polymers (EAPs) refer to a group of polymeric materials that have the ability to convert electrical energy into mechanical energy. In response to an applied electric field, an EAP will react with a significant change in size and shape. Deformation in polymers caused by an electric field was first discovered by Wilhelm Röntgen in 1880. The large actuated strains found in EAPs today is, however, a result of a series of new polymers developed since the early 1990. Large strains together with the purely polymeric benefits of low weight, low cost, commercial availability and the fact that they can be manufactured into complex shapes has attracted the attention from both industry and scientists. For an overview of the history of the research field and possible applications see for instance Bar-Cohen (2004); Smith (2005) and Kim and Tadokoro (2007).

EAP materials are usually divided into two main groups, electronic and ionic, depending on the type of actuation mechanism. Deformation of electronic electroactive polymers (EEAPs) is driven by electric fields and Coulomb forces, while in ionic electroactive polymers (IEAPs) the deformation involves movement and diffusion of ions. Within each group several subgroups are found. While dielectric-, ferroelectric- and electrostrictive polymers all refer to subgroups of EEAPs, ionic polymer gels and conductive polymers refer to subgroups of IEAPs. This thesis focuses on the first type of EAPs, i.e. electronic electroactive polymers, more specifically on the subgroup referred to as dielectric elastomers. A common usage of dielectric elastomers is as actuators. The main setup of a dielectric elastomer actuator (DEA) is a thin elastomeric membrane, sandwiched between two compliant electrodes. While the deformation in some EEAPs is driven by polarization of dipoles within the material that reorient at the application of an electric field, the deformation in DEAs is mainly caused by the so-called Maxwell effect. At large electric fields the Coulomb forces between the electrodes will force the electrodes toward each other, causing the actuator to compress in the direction parallel to the electric field. Due to the nearly incompressible nature of polymers the membrane will expand in the plane perpendicular to the electric field.

In the design process of EAP applications, both an in-depth knowledge of the material behaviour as well as predictive tools are essential. While physical tests and experiments are of great value in this process, accurate mathematical models of the response of EAPs will, from a control perspective, be of fundamental aid. The material response of electroactive polymers is complex and involves processes on multiple temporal and spatial scales. As such, appropriate constitutive models of EAPs involve consideration of micro-to-macro transitions, electromechanical coupling, viscous time-dependent effects and non-linear finite deformations, to name a few. In pursuit of incorporating these phenomena into a constitutive model, we have chosen to make use of the so-called micro-sphere approach. In short, the micro-sphere approach enables generalization of one-dimensional constitutive equations based on, for example, statistical mechanics of long molecular chains, to the three-dimensional continuum setting. The micro-sphere framework by Miehe et al, see (Miehe et al., 2004; Miehe and Göktepe, 2005), as proposed for modeling of rubber, is in this work extended to include electromechanical coupling. The related material parameters are identified

and used to solve representative boundary value problems, chosen to mimic potential or existing DEA applications. The effects of mechanical dissipation and control of these, as well as experimental investigations of acrylic-based DEAs are also included.

2 Mechanics and electrostatics

In this section the essential kinematic relations, electric quantities, and underlying balance equations that govern an electromechanically coupled problem are briefly reviewed. For detailed information regarding theory of nonlinear electroelasticity the reader is referred to Eringen and Maugin (1990) and Kovetz (2000).

2.1 Kinematics

Let the positions of particles, in a stress-free reference configuration $\mathcal{B}_0$, be denoted by $\boldsymbol{X}$ and by $\boldsymbol{x}$ in the current configuration $\mathcal{B}_t$. The motion of the body is described by the mapping $\boldsymbol{\varphi}(\boldsymbol{X}, t)$ where t represents time. The deformation gradient is given by $\boldsymbol{F} = \nabla_{\boldsymbol{X}} \boldsymbol{\varphi}$ with the important related relations $J = \det(\boldsymbol{F}) > 0$ and $\mathrm{cof}(\boldsymbol{F}) = J\boldsymbol{F}^{-\mathrm{t}}$. Due to the nearly incompressible nature of most elastomers, an intermediate volume preserving configuration, denoted $\bar{\mathcal{B}}_t$, is introduced. A multiplicative split of the deformation gradient into an isochoric and a volumetric part is made, such that

$$\boldsymbol{F} = J^{1/3} \bar{\boldsymbol{F}}, \tag{1}$$

where $\det\left(\bar{\boldsymbol{F}}\right) = 1$ follows. Based on this split the following related right Cauchy-Green tensors used are

$$\boldsymbol{C} = \boldsymbol{F}^{\mathrm{t}} \cdot \boldsymbol{F} \quad \text{and} \quad \bar{\boldsymbol{C}} = \bar{\boldsymbol{F}}^{\mathrm{t}} \cdot \bar{\boldsymbol{F}}, \tag{2}$$

where again, $\det\left(\bar{\boldsymbol{C}}\right) = 1$, follows. For more details regarding kinematics of solid continua, see for example Ogden (1997).

2.2 Electric field quantities

In this work, the electric quantities of interest are the electric field, electric displacement and polarization, denoted here as $\boldsymbol{E}$, $\boldsymbol{D}$ and as $\boldsymbol{\Pi}$ in the material configuration $\mathcal{B}_0$ and as $\boldsymbol{e}$, $\boldsymbol{d}$ and $\boldsymbol{\pi}$ in the spatial configuration $\mathcal{B}_t$. The interdependency between the three quantities in matter are governed by

$$\boldsymbol{d} = \varepsilon_0 \boldsymbol{e} + \boldsymbol{\pi}, \tag{3}$$

in the spatial configuration where ε_0 is the vacuum electric permittivity. In vacuo, $\boldsymbol{\pi} = \boldsymbol{0}$ holds, i.e. eq. (3) simplifies to $\boldsymbol{d} = \varepsilon_0 \boldsymbol{e}$. In material quantities the same relation reads

$$\boldsymbol{D} = J\varepsilon_0 \boldsymbol{E} \cdot \boldsymbol{C}^{-1} + \boldsymbol{\Pi}, \tag{4}$$

where $\boldsymbol{E} = \boldsymbol{e} \cdot \boldsymbol{F}$, $\boldsymbol{D} = \boldsymbol{d} \cdot \mathrm{cof}(\boldsymbol{F})$ and $\boldsymbol{\Pi} = \boldsymbol{\pi} \cdot \mathrm{cof}(\boldsymbol{F})$. In this thesis, $\boldsymbol{E}$ is taken as the independent electric variable while $\boldsymbol{D}$ is described by a constitutive equation so that $\boldsymbol{\Pi}$ is given by eq. (4).
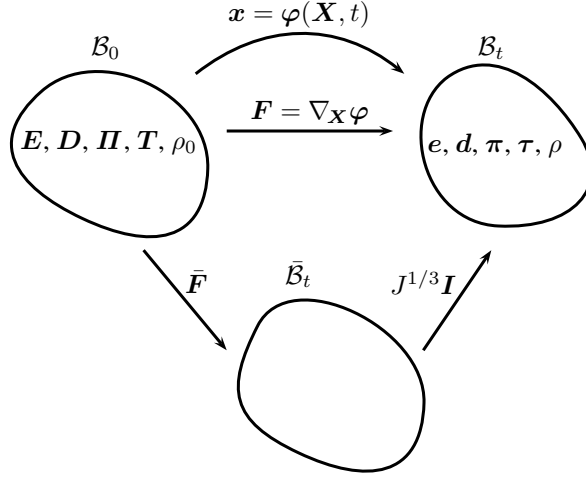
Figure 1: Schematic figure of referential, intermediate and current configuration and their respective quantities.

2.3   Balance of linear momentum

The quasi-static local form of the balance of linear momentum, in the presence of electromechanical interactions, reads

$$\nabla_{\boldsymbol{x}} \cdot \boldsymbol{\sigma} + \boldsymbol{f}_e + \rho \boldsymbol{f} = \boldsymbol{0} \tag{5}$$

where $\boldsymbol{f}_e$ represents the electrical body force and $\boldsymbol{f}$ the mechanical body force per unit mass and ρ is the mass density. The introduction of electromechanical interactions renders the Cauchy stress, $\boldsymbol{\sigma}$ to be, in general, unsymmetric. The influence of electrostatic forces are accounted for by the electric body force, which in this work takes the following form

$$\boldsymbol{f}_e = \nabla_{\boldsymbol{x}} \boldsymbol{e} \cdot \boldsymbol{\pi} = \nabla_{\boldsymbol{x}} \cdot \left[\boldsymbol{e} \otimes \boldsymbol{d} - \frac{1}{2} \left[\boldsymbol{e} \cdot \boldsymbol{e} \right] \boldsymbol{I} \right] . \tag{6}$$

By shifting the electrical body force to form a total, symmetric stress tensor $\boldsymbol{\tau} = \boldsymbol{\sigma} + \boldsymbol{e} \otimes \boldsymbol{d} - \frac{1}{2}\varepsilon_0 \left[\boldsymbol{e} \cdot \boldsymbol{e} \right] \boldsymbol{I}$, the balance of linear momentum takes the following form

$$\nabla_{\boldsymbol{x}} \cdot \boldsymbol{\tau} + \rho \boldsymbol{f} = \boldsymbol{0} \tag{7}$$

in the current configuration $\mathcal{B}_t$. The material counterpart in $\mathcal{B}_0$ then reads

$$\nabla_{\boldsymbol{X}} \cdot \boldsymbol{T} + \rho_0 \, \boldsymbol{f} = \boldsymbol{0} \, , \tag{8}$$

where $\boldsymbol{T} = \boldsymbol{\tau} \cdot \mathrm{cof}(\boldsymbol{F})$ and $\rho_0 = J \rho$ were used. See figure 1 for a schematic overview of configurations and respective quantities.

2.4   Gauss's law

The special case of Maxwell's equations in the absence of magnetic fields, free electric charges and time dependencies renders the Gauss's law wherein the spatial vectorial

3

fields $\boldsymbol{d}$ and $\boldsymbol{e}$ satisfy

$$\nabla_{\boldsymbol{x}} \cdot \boldsymbol{d} = 0 \quad \text{and} \quad \nabla_{\boldsymbol{x}}^{\mathrm{t}} \times \boldsymbol{e} = \boldsymbol{0} \,. \tag{9}$$

The material counterparts read

$$\nabla_{\boldsymbol{X}} \cdot \boldsymbol{D} = 0 \quad \text{and} \quad \nabla_{\boldsymbol{X}}^{\mathrm{t}} \times \boldsymbol{E} = \boldsymbol{0} \,. \tag{10}$$

The curl-free electric field together with the scalar-valued electric potential field yield the following forms of the electric field

$$\boldsymbol{e} = -\nabla_{\boldsymbol{x}} \phi \quad \text{and} \quad \boldsymbol{E} = -\nabla_{\boldsymbol{X}} \phi \,, \tag{11}$$

in the spatial and material configuration respectively.

3   Thermodynamics

The constitutive equations relating the deformation and the electric field to stress and electric displacement need to be formulated in a way that fulfils the laws of thermodynamics. The related dissipation inequality provides the constitutive equations as well as the evolution laws for the internal variables. This section summarises the local form of the first and second law of thermodynamics and the corresponding dissipation inequality for electromechanically coupled matter. As mentioned earlier, the analysis is restricted to electrostatics. Furthermore, free electric charges and electromagnetic coupling is not considered. For a full thermodynamic background the reader is referred to Eringen (1989); Eringen and Maugin (1990); Maugin (1999); Kovetz (2000) and McMeeking and Landis (2005).

3.1   First and second law of thermodynamics

The local forms of the first and second law of thermodynamics for dielectric solids and in terms of spatial arguments read

$$\rho \dot{\epsilon} = [\, \boldsymbol{\sigma} + [\, \boldsymbol{e} \cdot \boldsymbol{\pi} \,] \, \boldsymbol{I} \,] : \boldsymbol{l} + \boldsymbol{e} \cdot \dot{\boldsymbol{\pi}} - \nabla_{\boldsymbol{x}} \cdot \boldsymbol{q} + \rho h \,, \tag{12}$$

$$\rho \dot{\eta} \geq \rho h / \theta - \nabla_{\boldsymbol{x}} \cdot [\, \boldsymbol{q} / \theta \,] \,, \tag{13}$$

where $\dot{\bullet}$ refers to the material time derivative and ϵ is the internal energy per unit mass, so that $\dot{\epsilon}$ denotes the rate of change of internal energy per unit mass. Furthermore, $\boldsymbol{l} = \nabla_{\boldsymbol{x}} \dot{\boldsymbol{\varphi}}$ represents the spatial velocity gradient, $\boldsymbol{q}$ the spatial heat flux, θ the absolute temperature, h the heat source per unit mass and η is the specific entropy. The corresponding referential formulation reads

$$\rho_0 \dot{\epsilon} = [\, \boldsymbol{P} + [\, \boldsymbol{F}^{-\mathrm{t}} \cdot \boldsymbol{E} \,] \otimes \boldsymbol{\Pi} \,] : \dot{\boldsymbol{F}} + \boldsymbol{E} \cdot \dot{\boldsymbol{\Pi}} - \nabla_{\boldsymbol{X}} \cdot \boldsymbol{Q} + \rho_0 h \,, \tag{14}$$

$$\rho_0 \dot{\eta} \geq \rho_0 h / \theta - \nabla_{\boldsymbol{X}} \cdot [\, \boldsymbol{Q} / \theta \,] \,, \tag{15}$$

where $\dot{\boldsymbol{F}} = \nabla_{\boldsymbol{X}} \dot{\boldsymbol{\varphi}} = \boldsymbol{l} \cdot \boldsymbol{F}$, $\boldsymbol{P} = \boldsymbol{\sigma} \cdot \mathrm{cof}(\boldsymbol{F})$ and $\boldsymbol{Q} = \boldsymbol{q} \cdot \mathrm{cof}(\boldsymbol{F})$ were used.

4

3.2 Dissipation inequality

The dissipation inequality, here presented for the isothermal case, is obtained by introducing the Helmholtz free energy, $\psi = \epsilon - \theta\,\eta$, in eq. (12) and (13) such that

$$-\rho\dot{\psi} + [\,\boldsymbol{\sigma} + [\,\boldsymbol{e}\cdot\boldsymbol{\pi}\,]\,\boldsymbol{I}\,] : \boldsymbol{l} + \boldsymbol{e}\cdot\dot{\boldsymbol{\pi}} \geq 0\,. \tag{16}$$

In material quantities (using eq. (14) and (15) instead) the dissipation inequality reads

$$-\rho_0\dot{\psi} + [\,\boldsymbol{P} + [\,\boldsymbol{F}^{-t}\cdot\boldsymbol{E}\,]\otimes\boldsymbol{\Pi}\,] : \dot{\boldsymbol{F}} + \boldsymbol{E}\cdot\dot{\boldsymbol{\Pi}} \geq 0\,. \tag{17}$$

Using a second Legendre transformation between $\psi(\boldsymbol{F},\boldsymbol{\Pi},\boldsymbol{K})$ and $\Psi(\boldsymbol{F},\boldsymbol{E},\boldsymbol{K})$ so that $\Psi = \psi - \frac{1}{\rho_0}\boldsymbol{\Pi}\cdot\boldsymbol{E}$ and where $\boldsymbol{K}$ represents some internal variables governing the viscous time-dependent response the material version of the dissipation inequality can be rewritten as

$$-\rho_0\dot{\Psi} + [\,\boldsymbol{P} + [\,\boldsymbol{F}^{-t}\cdot\boldsymbol{E}\,]\otimes\boldsymbol{\Pi}\,] : \dot{\boldsymbol{F}} - \boldsymbol{\Pi}\cdot\dot{\boldsymbol{E}} \geq 0\,. \tag{18}$$

Finally, an augmented free energy $\Omega = \rho_0\Psi - \frac{1}{2}\varepsilon_0 J\boldsymbol{C}^{-1} : [\,\boldsymbol{E}\otimes\boldsymbol{E}\,]$, as proposed in Dorfmann and Ogden (2005), is introduced so that eq. (18) then reads

$$\left[-\boldsymbol{T} + \frac{\partial\Omega}{\partial\boldsymbol{F}}\right] : \dot{\boldsymbol{F}} + \left[-\boldsymbol{D} - \frac{\partial\Omega}{\partial\boldsymbol{E}}\right] \cdot \dot{\boldsymbol{E}} - \frac{\partial\Omega}{\partial\boldsymbol{K}} \cdot \dot{\boldsymbol{K}} \geq 0\,. \tag{19}$$

The following forms of the total stress $\boldsymbol{T}$ and the electric displacement $\boldsymbol{D}$,

$$\boldsymbol{T} = \frac{\partial\Omega}{\partial\boldsymbol{F}} \quad \text{and} \quad \boldsymbol{D} = -\frac{\partial\Omega}{\partial\boldsymbol{E}}\,, \tag{20}$$

together with

$$\mathcal{D}_{red} = -\frac{\partial\Omega}{\partial\boldsymbol{K}} \cdot \dot{\boldsymbol{K}} \geq 0\,, \tag{21}$$

ensures the dissipation inequality to be unconditionally fulfilled.

4 Constitutive framework

The underlying concept for the constitutive framework used in this thesis is based on modeling of rubbery polymers. An overview of constitutive models for rubbery polymers can be found in Boyce and Arruda (2000). Within this field of constitutive models both macroscopic continuum and micro-mechanically based formulations can be found. The constitutive framework in this thesis falls into the latter category and is, in large parts, based on the micro-mechanically motivated microsphere model introduced by Miehe et al. (2004). The microsphere model is in Paper A extended to include electromechanical coupling for finite element simulation of electrostrictive polymers.

Microsphere models share similarities with the earlier so-called microplane models, first proposed by Bažant and Oh (1983) for modeling of quasi-brittle structures undergoing small strains. The microplane theory was later extended to account for

thermodynamic consistency and finite deformations, see Carol et al. (2001) and Carol et al. (2004). Common for both approaches is the idea that the macroscopic response is found by superimposing the response in all directions over the surface of a unit microsphere. Both model approaches have proven useful in a number of applications and research fields, in addition to the above mentioned, e.g in modeling of phase transformations of polycrystalline materials, see Ostwald et al. (2015) as well as for modeling of biological tissue, see Alastrué et al. (2009).

Polymers consist of long molecular chains interlinked to form a three-dimensional network through crosslinks at certain, so-called, junction points. In modeling this type of material, one-dimensional micromechanically motivated constitutive relations are provided using the framework of statistical mechanics.

4.1   Statistics of long-chain molecules

Within the context of statistical mechanics an idealised model of a single chain is introduced. The simplest statistical model considers a single, freely jointed, molecular chain consisting of N number of segments of equal length l. The end-to-end distance is denoted by the vector $\boldsymbol{r}$ which in an unstrained state takes the value $r_0 = \sqrt{N} l$ and at the fully extended state assumes the value $r_L = N l$, see for example James and Guth (1944); Treloar (1975); Kawakatsu (2004) and Strobe (2007) for an introduction of statistical micromechanics of polymers. Corresponding dimensionless kinematic descriptions of the individual chains involve the stretch, $\lambda = r/r_0$ and the corresponding fully extended chain-locking stretch defined as $\lambda_L = r_L/r_0 = \sqrt{N}$.

A key ingredient in the elasticity of rubbers is the number of conformations available to the single chain. In a polymer network the number of conformations are limited by the neighbouring chains. Extensions of the classical theories within molecular statistics to include these effects has therefore been proposed, see Heinrich et al. (1988) for an overview.

4.2   Micro-sphere model

In the context of polymers the microsphere model can be interpreted to be composed of a continuous distribution of polymer chain orientations in space. The macroscopic free energy of the network, Ω, is evaluated by a direction average of the microscopic counterpart, Ω, through integration over the surface of the unit microsphere $\mathbb{U}^2$. In general, such integrations cannot be performed analytically but are approximated by a numerical integration scheme, i.e.

$$\Omega = n \frac{1}{4\pi} \int_{\mathbb{U}^2} \Omega \, \mathrm{d}A \approx n \sum_{i=1}^{\mathrm{nid}} \Omega_i \, \omega_i \,, \tag{22}$$

where n denotes the number of chains in the network, i refers to a referential unit integration direction $\boldsymbol{n}_i \in \mathbb{U}^2$ and ω_i denotes non-negative integration weights constrained by $\sum_{i=1}^{\mathrm{nid}} \omega_i = 1$.

To describe the deformation of an individual chain in the polymer network, two kinematic variables, the length stretch λ_f and the area-stretch λ_c, are introduced

$$\lambda_f = \frac{r}{r_0} \quad \text{and} \quad \lambda_c = \left[\frac{d_0}{d} \right]^2 , \tag{23}$$

where r and r_0 refer to the deformed and undeformed end-to-end distance of the polymer chain. d and d_0 refer to the deformed and undeformed diameter of an imagined tube surrounding the polymer chain so that the number of possible conformations available to the chain is constrained. In terms of electrical quantities the following scalar electric field type quantity is introduced

$$E = -\frac{\Delta\phi}{r_0} , \tag{24}$$

where $\Delta\phi$ is the difference in electric potential over a single polymer chain. Next, the kinematic and electric quantities referring to the underlying unit microsphere are introduced. The macroscopic kinematic quantities $\bar{\boldsymbol{F}}$, $\text{cof}(\bar{\boldsymbol{F}})$ and the electric field $\boldsymbol{E}$, are projected onto the integration directions such that

$$\lambda_{f_i} = \|\bar{\boldsymbol{F}} \cdot \boldsymbol{n}_i\|, \quad \lambda_{c_i} = \|\bar{\boldsymbol{F}}^{-\text{t}} \cdot \boldsymbol{n}_i\| \quad \text{and} \quad E_i = \boldsymbol{E} \cdot \boldsymbol{n}_i . \tag{25}$$

Finally, the transformation between macro- and microscopic variables needs to be defined. In general these transformations are either affine or non-affine. In this work, the following notation is used for the affine and non-affine relations respectively

$$\Omega = \begin{cases} n \left\langle \Omega\left(x\right) \right\rangle & \text{affine} \\ n \, \Omega\left(\left\langle x \right\rangle\right) & \text{non-affine} \end{cases} \tag{26}$$

where $\langle \bullet \rangle$ is introduced, for brevity, as an alternative notation for the directional average procedure introduced in eq. (22).

When considering viscous effects, as is done in Paper B, a reduced microscopic dissipation is introduced and related to the macroscopic counterpart in eq. (21), by means of the direction average, such that

$$\mathcal{D}_{red} = \langle \mathcal{D}_{red,mic} \rangle \geq 0 . \tag{27}$$

5 Dielectric elastomers

The particular subgroup of EAPs in focus of this thesis is the dielectric elastomers. Owing to its combination of large actuated strains, relatively fast response and high specific energy the dielectric elastomer actuators are today found as transducers in a broad range of applications including adaptive optics, loudspeakers, Braille displays, micropumps and energy harvesting systems, among many others. The viscous time-dependent behaviour associated with most elastomers impose a drawback and limit the number of possible applications. To this end the possibility to control these effects by regulating the applied electric potential is elaborated in Paper C.

The increase in use of DEAs and of areas of applications has inspired a large number of experimental investigations. One of the most common investigated elastomer for DEA applications is VHB 4910 from 3M. It is characterised as an acrylic-based elastomer with a highly non-linear elastic and viscoelastic response, a relatively high dielectric constant and can give actuated areal strains greater than 100%, see e.g. Pelrine et al. (2000). Experimental investigations of VHB 4910 includes for example Kofod et al. (2003); Wissler and Mazza (2007); Di Lillo et al. (2012); Sahu et al. (2015) and Hossain et al. (2015).

Due to lack of full-field measurements of dielectric elastomers found in the literature and the difficulty of measuring the thickness during electric loading, the use of three-dimensional surface digital image correlation (DIC) is included in Paper D. By correlating pixel subsets between a series of images during loading, the surface displacement field is resolved. Furthermore, by assuming the deformation to be incompressible and homogeneous through the thickness, the out-of-plane deformation field is also obtained, see figure 2 for results found in Paper B.
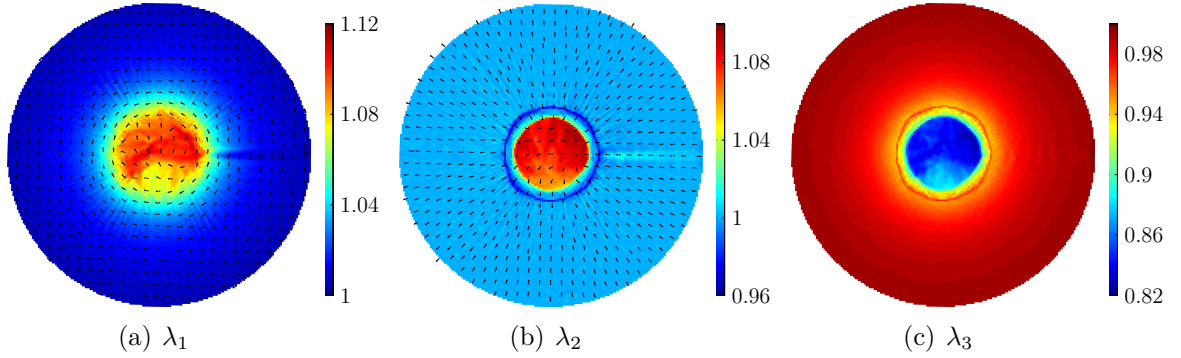

(a) λ_1 (b) λ_2 (c) λ_3

Figure 2: Resulting principal stretch fields resulting from electric activation of a circular VHB 4910 membrane with an initial equi-biaxial stretch $\lambda_x \times \lambda_y = 2 \times 2$. Arrows in the two first columns indicate corresponding principal directions.

6 Summary and future work

This thesis concerns the modeling of electro-active polymers, more specifically of the so-called dielectric elastomers. The basic configuration of a dielectric elastomer actuator consists of a thin polymeric membrane sandwidched between two compliant electrodes. Under the application of an electric field the actuator will contract in the direction of the applied field and expand in the area perpendicular to the applied field. In dielectric elastomers this mechanism is mainly attributed to the Maxwell effect. The constitutive model developed in this work is based on an extension of a microsphere formulation, originally proposed for large strain behaviour of rubber, to include electromechanical coupling. The model is further calibrated to fit the response of a typical DEA elastomer and the possibility of controlling viscous effects in existing applications is elaborated. Finally, an experimental investigation of the

electromechancial and time-dependent behaviour of the same material is investigated using digital image correlation.

A reliable, robust and micromechanically motivated constitutive model of EAPs offers considerable possibilities for future research. Generally, experimental investigations are of great importance in validation of proposed models as well as in understanding of underlying phenomena yielding the material response. In that pursuit, combining full-field measurements of deformation on multiple length-scales, as is performed in e.g. Engqvist et al. (2014), could be elaborated. Furthermore, the electromechanical part of the free energy developed in this thesis is not, as the mechanical parts of the free energy, fully microscopically motivated. Models of the electrical response, based on the physical structure of the polymer chain network, as is elaborated in for example Cohen et al. (2016), would greatly facilitate in understanding the material behaviour as well as enhance the constitutive model.

7 Summary of appended papers

Paper A: A modelling framework for electroactive polymers is established. The framework combines the micro-sphere approach with general finite element method techniques to solve electromechanically coupled boundary value problems. The free energy function used is based on a neo-Hooke-type contribution for the elastic part and terms quadratic in the electric field for coupled electro-elastic and purely electric part. No viscous effects are considered. Both homogeneous and inhomogeneous numerical examples are presented which show that the framework is capable of producing physically sound results.

Paper B: The framework developed in Paper A is extended to include micromechanically motivated elastic parts and non-affine kinematics. The new free energy introduced includes an isochoric-volumetric split capable of capturing the behaviour of nearly incompressible elastomers as well as time-dependent viscous effects. The model is calibrated to fit the response of VHB 4910, which is a popular candidate for dielectric actuators, both through homogeneous deformation and inhomogeneous finite element deformation examples.

Paper C: In paper C the possibility to control the viscous time-dependent behaviour associated with dielectric elastomers is elaborated by regulating the applied electric potential. The constitutive model used is taken from Paper B. Both homogeneous deformation examples and inhomogeneous finite element boundary value problems, chosen to mimic existing applications, are investigated. Control of both force and displacement quantities is successfully achieved.

Paper D: Motivated by the work in paper B an experimental investigation of VHB 4910 is performed. A circular and biaxially pre-stretched membrane is electrically actuated using graphite powder electrodes. The deformation is measured using three-dimensional surface digital image correlation. The resulting strain field reveals inhomogeneous deformations not visible using conventional measurement techniques. Special emphasis is placed on the out-of-plane deformation and its connection to common instabilities found in dielectric elastomer actuators.

References

Alastrué, V., Martínez, M., Doblaré, M., Menzel, A., 2009. Anisotropic micro-sphere-based finite elasticity applied to blood vessel modelling. J. Mech. Phys. Solids 57 (1), 178–203.

Bar-Cohen, Y. (Ed.), 2004. Electroactive Polymer (EAP) Actuators as Artificial Muscles: Reality, Potential, and Challenges, 2nd Edition. SPIE Press.

Bažant, Z. P., Oh, B. H., 1983. Microplane model for fracture analysis of concrete structures. Proc. Symp. Interact. Non-Nucl. Munitions Struct., 49–55.

Boyce, M. C., Arruda, E. M., 2000. Constitutive Models of Rubber Elasticity: A Review. Rubber Chem. Technol. 73 (3), 504–523.

Carol, I., Jirásek, M., Bažant, Z., 2001. A thermodynamically consistent approach to microplane theory. Part I. Free energy and consistent microplane stresses. Int. J. Solids Struct. 38 (17), 2921–2931.

Carol, I., Jirásek, M., Bažant, Z. P., 2004. A framework for microplane models at large strain, with application to hyperelasticity. Int. J. Solids Struct. 41 (2), 511–557.

Cohen, N., Menzel, A., deBotton, G., 2016. Towards a physics-based multiscale modelling of the electro-mechanical coupling in electro-active polymers. Proc. R. Soc. A 472 (2186).

Di Lillo, L., Schmidt, A., Carnelli, D. A., Ermanni, P., Kovacs, G., Mazza, E., Bergamini, A., 2012. Measurement of insulating and dielectric properties of acrylic elastomer membranes at high electric fields. J. Appl. Phys. 111 (2), 024904.

Dorfmann, A., Ogden, R. W., 2005. Nonlinear electroelasticity. Acta Mech. 174 (3), 167–183.

Engqvist, J., Hall, S. A., Wallin, M., Ristinmaa, M., Plivelic, T. S., 2014. Multi-scale measurement of (amorphous) polymer deformation: simultaneous x-ray scattering, digital image correlation and in-situ loading. Exp. Mech. 54 (8), 1373–1383.

Eringen, A. C., 1989. Mechanics of Continua. Krieger.

Eringen, A. C., Maugin, G. A., 1990. Electrodynamics of Continua I – Foundations and Solid Media. Springer.

Heinrich, G., Straube, E., Helmis, G., 1988. Rubber elasticity of polymer networks: Theories. Springer Berlin Heidelberg, Berlin, Heidelberg, pp. 33–87.

Hossain, M., Vu, D. K., Steinmann, P., 2015. A comprehensive characterization of the electro-mechanically coupled properties of VHB 4910 polymer. Arch. Appl. Mech. 85 (4), 523–537.

James, H. M., Guth, E., 1944. Theory of the Elasticity of Rubber. J. Appl. Phys. 15 (4), 294–303.

Kawakatsu, T., 2004. Statistical Physics of Polymers: An Introduction. Springer-Verlag.

Kim, K., Tadokoro, S. (Eds.), 2007. Electroactive Polymers for Robotic Applications: Artificial Muscles and Sensors. Springer.

Kofod, G., Sommer-Larsen, P., Kornbluh, R., Pelrine, R., 2003. Actuation response of polyacrylate dielectric elastomers. J. Intel. Mat. Syst. Str. 14 (12), 787–793.

Kovetz, A., 2000. Electromagnetic Theory. Oxford University Press.

Maugin, G. A., 1999. The Thermomechanics of Nonlinear Irreversible Behaviours: An Introduction. World Scientific.

McMeeking, R. M., Landis, C. M., 7 2005. Electrostatic forces and stored energy for deformable dielectric materials. ASME J. Appl. Mech. 72 (4), 581–590.

Miehe, C., Göktepe, S., 2005. A micro–macro approach to rubber-like materials. Part II: The micro-sphere model of finite rubber viscoelasticity. J. Mech. Phys. Solids 53 (10), 2231–2258.

Miehe, C., Göktepe, S., Lulei, F., 2004. A micro-macro approach to rubber-like materials—Part I: the non-affine micro-sphere model of rubber elasticity. J. Mech. Phys. Solids 52 (11), 2617–2660.

Ogden, R. W., 1997. Non-linear Elastic Deformations. Dover.

Ostwald, R., Bartel, T., Menzel, A., 2015. An energy-barrier-based computational micro-sphere model for phase-transformations interacting with plasticity. Comput. Methods Appl. Mech. Engng. 293, 232–265.

Pelrine, R., Kornbluh, R., Pei, Q., Joseph, J., 2000. High-speed electrically actuated elastomers with strain greater than 100%. Science 287 (5454), 836–839.

Sahu, R., Patra, K., Szpunar, J., 2015. Experimental study and numerical modelling of creep and stress relaxation of dielectric elastomers. Strain 51 (1), 43–54.

Smith, R. C., 2005. Smart Material Systems – Model Development. Frontiers in Applied Mathematics. SIAM.

Strobe, G., 2007. The Physics of Polymers, 3rd Edition. Springer.

Treloar, L. R. G., 1975. Physics of Rubber Elasticity, 3rd Edition. Clarendon Press.

Wissler, M., Mazza, E., 2007. Mechanical behavior of an acrylic elastomer used in dielectric elastomer actuators. Sens. Act. A: Phys. 134 (2), 494–504.

Paper A

S. Thylander, A. Menzel and M. Ristinmaa

*An electromechanically coupled micro-sphere framework:
application to the finite element analysis of electrostricitve polymers*

An electromechanically coupled micro-sphere framework: application to the finite element analysis of electrostrictive polymers

Sara Thylander[a], Andreas Menzel[a,b] and Matti Ristinmaa[a]

[a] Division of Solid Mechanics, Lund University

P.O. Box 118, S-221 00 Lund, Sweden

[b] Department of Mechanical Engineering, Institute of Mechanics, TU Dortmund

Leonhard-Euler-Str. 5, D-44227 Dortmund, Germany

Abstract

The number of industrial applications of electroactive polymers (EAPs) is increasing and, consequently, the need for reliable modelling frameworks for such materials as well as related robust simulation techniques continuously increases. In this context, we combine the modelling of nonlinear electroelasticity with a computational micro-sphere formulation in order to simulate the behaviour of EAPs. The micro-sphere approach in general enables the use of physics-based constitutive models like, for instance, the so-called worm like chain model. By means of the micro-sphere formulation, scalar-valued micromechanical constitutive relations can conveniently be extended to a three-dimensional continuum setting. We discuss several electromechanically coupled numerical examples and make use of the finite element method to solve inhomogeneous boundary value problems. The incorporated material parameters are referred to experimental data for an electrostrictive polymer. The numerical examples show that the coupled micro-sphere formulation combined with the finite element method results in physically sound simulations that mimic the behaviour of an electrostrictive polymer.

1

1 Introduction

Along with the commercialisation of electroactive polymers (EAPs) the interest in smart materials and structures is continuously growing. With their low weight, capability of large strains, low cost and scalability, EAP applications become not only more realistic but close to being present in every day life. With the ability to transform electrical energy into mechanical energy together with the capacity to change size and shape, EAPs find applications as actuators and sensors in several areas such as robotics and biomimetics; see the contributions in Bar-Cohen (2004) and Kwang and Tadokoro (2007). In a comparison made by Kornbluh et al. (1998) between different technologies used for artificial muscle actuators, the performance of the electrostrictive polymer actuator turns out to be the one most similar to biological muscles. Carpi et al(Carpi et al., 2011) identify three main contributors to the increasing interest in EAPs: technological breakthroughs in science, the discovery of new material properties in previously developed EAP, and increased efforts to further develop industrial applications.

EAP materials can be divided into two main groups: electronic EAPs and ionic EAPs, see Bar-Cohen (2004). In electronic EAPs the deformation can be driven by either an applied electric field directly or by the Coulomb force that is generated by the electric potential. In ionic EAPs the deformation can be driven by the transportation of ions or molecules that takes place as the electric field is applied; see Bar-Cohen et al. (2001) and Blythe and Bloor (2005) for further background information. The electronic EAPs are further divided into piezoelectric, electrostrictive and ferroelectric EAPs depending on their relations between strains, the electric field and the polarisation; the reader is referred to Nalwa (1995) and Smith (2005) regarding this topic. In this article the focus is on electronic EAPs, more precisely on a subgroup called dielectric EAPs with an electrostrictive effect. Electrostrictive polymer materials show—at small loading levels— strains that are quadratic in the polarisation, (Bar-Cohen et al., 2001). Typical applications of electrostrictive polymers are artificial muscle actuators, see Kwang and Tadokoro (2007). Dielectric EAP actuators can produce large strains up to 200 % but require a high electric field, 100 [V/μm], to activate these, see Bar-Cohen (2004).

Along with the increased commercial interest in electroactive polymers, the need for experimental investigations, theoretical developments and computational modelling of these materials increases, especially for situations of finite deformations under the action of an electric field. As a consequence, several research works focus on related experimental investigations, see for instance (Diaconu et al., 2008; York et al., 2010; Potter et al., 2011), the theoretical modelling, see (McMeeking and Landis, 2005; McMeeking et al., 2007; Dorfmann and Ogden, 2005, 2006; Rudykh and deBotton, 2011), and the numerical simulation, see (Vu et al., 2007; Vu and Steinmann, 2012), of non-linear electroelasticity; for a review the reader is also referred to the contributions in Ogden and Steigmann (2011) and Suo (2010). The modelling of viscous material properties of EAPs is addressed in, for example, Wissler and Mazza (2005); Hong (2011); Ask et al. (2010) and Ask et al. (2012a); see also references cited in these works. Special emphasis on the modelling of EAP-based composites is placed

in, for instance, Hirano et al. (2011); Bertoldi and Gei (2011) and Tian et al. (2012).

To model the electroelastic behaviour of the EAP, use will be made of a micro-plane, also called micro-sphere, theory. The micro-plane theory was first proposed by Bažant and Oh, see Bažant and Oh (1983), for the modelling of materials such as concrete or ceramics, but has since found new areas of applications; see, for example, Carol et al. (2001); Kuhl et al. (2001) and Waffenschmidt and Menzel (2012). The extension of the micro-plane model to the case of finite deformations is often denoted as micro-sphere model. Affine and non-affine formulations have been established in the literature with application to elastic and inelastic rubber-like materials, see Miehe et al. (2004) and Miehe and Göktepe (2005). The aim of this work is to further develop a coupled micro-sphere framework for the computational modelling of non-linear electroelastic behaviour. A key idea of the micro-sphere formulation is to extend one-dimensional constitutive equations to the three-dimensional continuum setting. The particular one-dimensional models used can be based on, for example, a statistical mechanics background so that the material model at the continuum level possesses a sound physical motivation. To give an example, worm-like chain models can conveniently be combined with the micro-sphere framework; the reader is referred to Beatty (1987); Miehe et al. (2004); Kuhl et al. (2006) and Ogden et al. (2006) for detailed background information. Another advantage of the micro-sphere formulation is the possibility to include the modelling of anisotropic material properties and the evolution of these, see for example Menzel and Waffenschmidt (2009) and Waffenschmidt et al. (2012).

The paper is organised as follows: basic equations of non-linear electroelasticity are first briefly presented in section 2. Constitutive equations, along with the introduction of the micro-sphere framework, are established in section 3. In the following section 4 four examples are discussed—two examples under a homogeneous deformation and two inhomogeneous boundary value problems, which are solved by means of a coupled finite element formulation. Finally, the paper is concluded with a brief summary in section 5.

2   Basic equations

In this section the basic equations of electroelasticity are presented, whereby we briefly review essential kinematic relations as well as the underlying balance equations in local form. For detailed background information regarding the theory of nonlinear electroelasticity, see for example Kovetz (2000) and Bobbio (2000) and references cited therein.

2.1   Kinematics

Let the body of interest in the reference configuration be denoted by $\mathcal{B}_0$ and $\mathcal{B}_t$ in the current configuration. Positions of material particles in the reference configuration are characterised by the vectors $\boldsymbol{X}$ and $\boldsymbol{x} = \boldsymbol{\varphi}(\boldsymbol{X}, t)$ in the current configuration,

whereby t represents time. The related so-called deformation gradient $\boldsymbol{F}$ is defined as

$$\boldsymbol{F} = \nabla_{\boldsymbol{X}}\,\boldsymbol{\varphi} \quad \text{with} \quad J = \det(\boldsymbol{F}) > 0\,, \tag{1}$$

and $\text{cof}(\boldsymbol{F}) = \partial_{\boldsymbol{F}} J = J\,\boldsymbol{F}^{-\text{t}}$. The deformation gradient is multiplicative split into a volumetric and isochoric part, i.e.

$$\boldsymbol{F} = J^{1/3}\,\bar{\boldsymbol{F}} \quad \text{so that} \quad \det(\bar{\boldsymbol{F}}) = 1\,. \tag{2}$$

Based on the split of the deformation gradient, two different right Cauchy-Green tensors are introduced, to be specific

$$\boldsymbol{C} = \boldsymbol{F}^{\text{t}} \cdot \boldsymbol{F} \quad \text{and} \quad \bar{\boldsymbol{C}} = \bar{\boldsymbol{F}}^{\text{t}} \cdot \bar{\boldsymbol{F}}\,, \tag{3}$$

with $\det(\bar{\boldsymbol{C}}) = 1$ being obvious.

2.2 Balance equations

In the absence of magnetic fields the electric displacement $\boldsymbol{d}$ and electric field $\boldsymbol{e}$ in the current configuration are governed by the following equations

$$\nabla_{\boldsymbol{x}} \cdot \boldsymbol{d} = 0 \quad \text{and} \quad \nabla_{\boldsymbol{x}}^{\text{t}} \times \boldsymbol{e} = \boldsymbol{0}\,, \tag{4}$$

where the free charge density is set to zero as is common for a dielectric. Due to eq. $(4)_2$ the electric field $\boldsymbol{e}$ can be represented as the gradient of a scalar-valued function, the so-called electric potential $\phi(\boldsymbol{X}, t)$, such that

$$\boldsymbol{e} = -\,\nabla_{\boldsymbol{x}}\,\phi\,. \tag{5}$$

For a given electric field $\boldsymbol{e}$ the electric displacement reads $\boldsymbol{d} = \varepsilon_0\,\boldsymbol{e} + \boldsymbol{p}$ where ε_0 is the vacuum electric permittivity and $\boldsymbol{p}$ is the so-called polarisation vector.

By analogy with the local form of Gauss law in eq. $(4)_1$ the quasi-static local form of the balance of linear momentum reads

$$\nabla_{\boldsymbol{x}} \cdot \boldsymbol{\tau} + \boldsymbol{f}_t^{\text{mec}} = \boldsymbol{0}\,, \tag{6}$$

wherein $\boldsymbol{f}^{\text{mec}}$ characterises mechanical volume forces. The specific format chosen in eq. (6) includes, or rather shifts, electrical volume forces, $\nabla_{\boldsymbol{x}}\,\boldsymbol{e}\cdot\boldsymbol{p}$, to the mechanical flux term and adds these to the generally un-symmetric Cauchy stresses $\boldsymbol{\sigma}$; see Dorfmann and Ogden (2005) and Eringen and Maugin (1990) for additional background and microscopic or rather physics-based derivations. In consequence, the total stress tensor $\boldsymbol{\tau}$ turns out to be symmetric and is given as

$$\boldsymbol{\tau} = \boldsymbol{\sigma} + \boldsymbol{d} \otimes \boldsymbol{e} - \frac{1}{2}\,\varepsilon_0\,[\,\boldsymbol{e} \cdot \boldsymbol{e}\,]\,\boldsymbol{I}\,, \tag{7}$$

wherein $\boldsymbol{I}$ denotes the second-order identity tensor.

4

The balance equations can also be referred to the reference configuration. The electric displacements and the electric field related to the reference configuration are denoted as $\boldsymbol{D}$ and $\boldsymbol{E}$ and by analogy with eq. (4) we obtain

$$\nabla_{\boldsymbol{X}} \cdot \boldsymbol{D} = 0 \quad \text{and} \quad \nabla_{\boldsymbol{X}}^{\text{t}} \times \boldsymbol{E} = \boldsymbol{0}\,. \tag{8}$$

The transformation of electrical and mechanical flux terms in the current configuration, i.e. $\boldsymbol{d}$ and $\boldsymbol{\tau}$, to the reference configuration, here $\boldsymbol{D}$ and $\boldsymbol{T}$, are defined by so-called Piola transformations, i.e.

$$\boldsymbol{D} = \boldsymbol{d} \cdot \text{cof}(\boldsymbol{F}) \quad \text{and} \quad \boldsymbol{T} = \boldsymbol{\tau} \cdot \text{cof}(\boldsymbol{F})\,. \tag{9}$$

From the gradient operation in eq. (5) and the definition of the deformation gradient, the transformation of the electric field

$$\boldsymbol{E} = \boldsymbol{e} \cdot \boldsymbol{F} = -\nabla_{\boldsymbol{X}}\, \phi\,, \tag{10}$$

becomes obvious. With these relations at hand, the quasi-static local balance of linear momentum relation with respect to the reference configuration is found as

$$\nabla_{\boldsymbol{X}} \cdot \boldsymbol{T} + \boldsymbol{f}_0^{\text{mec}} = \boldsymbol{0}\,, \tag{11}$$

with $\boldsymbol{f}_0^{\text{mec}} = J\, \boldsymbol{f}_t^{\text{mec}}$.

3 Constitutive equations

The constitutive framework established in this work is based on two key assumptions or rather frameworks: the existence of an amended free energy function and the so-called micro-sphere approach. Introducing an amended free energy, as used in Dorfmann and Ogden (2005), allows to make use of, say, hyper-elastic forms, from which the electromechanical flux terms can be derived. The micro-sphere framework, applied here in the context of a coupled problem, enables to generalise physics-based one-dimensional constitutive equations to the three-dimensional case. A typical example is the so-called worm like chain model, even though we will restrict the examples investigated in this work to more standard energy representations.

3.1 Hyper-elastic forms based on the amended free energy

A full review of the thermodynamical framework is not included in this contribution—as this is well-documented in the literature, see for instance Eringen (1989) and Maugin (1988). The starting point is instead the existence of an amended free energy function Ω defined in terms of the deformation gradient and the electric field. Adopting an additive split of Ω in volumetric elastic and isochoric electroelastic contributions, as is also common in the modelling of polymers, we assume the following form

$$\Omega(\boldsymbol{F}, \boldsymbol{E}) = \Omega^{\text{vol}}(J) + \Omega^{\text{iso}}(\bar{\boldsymbol{C}}) + \Omega^{\text{mel}}(\bar{\boldsymbol{C}}, \boldsymbol{E}) + \Omega^{\text{ele}}(\boldsymbol{E}) - \frac{1}{2}\varepsilon_0\, J\, \boldsymbol{E} \cdot \boldsymbol{C}^{-1} \cdot \boldsymbol{E}\,, \tag{12}$$

where the explicit dependencies on material placements $\boldsymbol{X}$ is suppressed to simplify notation.

With this form of the amended free energy at hand, the electromechanical flux terms $\boldsymbol{D}$ and $\boldsymbol{T}$ can, based on $\boldsymbol{E}$ and $\boldsymbol{F}$, be introduced by means of derivatives of eq. (12). Based on $\boldsymbol{T} = \partial_{\boldsymbol{F}}\Omega$ we introduce a Piola-Kirchhoff-type referential stress tensor $\boldsymbol{S} = \boldsymbol{F}^{-1} \cdot \boldsymbol{T}$

$$
\begin{aligned}
\boldsymbol{S} \;=\;& 2\,\partial_{\boldsymbol{C}}\Omega \\
=\;& J\,\partial_J \Omega^{\mathrm{vol}}\, \boldsymbol{C}^{-1} + 2\,J^{-2/3}\,\mathbf{P} : [\,\partial_{\bar{\boldsymbol{C}}}\Omega^{\mathrm{iso}} + \partial_{\bar{\boldsymbol{C}}}\Omega^{\mathrm{mel}}\,] \\
& + \varepsilon_0\, J\,\big[\,[\,\boldsymbol{C}^{-1}\cdot\boldsymbol{E}\,] \otimes [\,\boldsymbol{E}\cdot\boldsymbol{C}^{-1}\,] - \tfrac{1}{2}\,[\,\boldsymbol{E}\cdot\boldsymbol{C}^{-1}\cdot\boldsymbol{E}\,]\,\boldsymbol{C}^{-1}\,\big]\,,
\end{aligned}
\tag{13}
$$

with $\mathbf{P}^{\mathrm{T}} = J^{2/3}\,\partial_{\bar{\boldsymbol{C}}}\boldsymbol{C} = [\,\mathbf{I}^{\mathrm{sym}} - \tfrac{1}{3}\,\boldsymbol{C}\otimes\boldsymbol{C}^{-1}\,]$ so that $\mathbf{P} = \mathbf{I}^{\mathrm{sym}} - \tfrac{1}{3}\,\boldsymbol{C}^{-1}\otimes\boldsymbol{C}$. Moreover, $\mathbf{I}^{\mathrm{sym}} = \tfrac{1}{2}\,[\,\boldsymbol{I}\,\overline{\otimes}\,\boldsymbol{I} + \boldsymbol{I}\,\underline{\otimes}\,\boldsymbol{I}\,]$ denotes the fourth-order symmetric identity tensor. By analogy with eq. (13) we obtain the electric displacements as

$$
\boldsymbol{D} \;=\; -\partial_{\boldsymbol{E}}\Omega = -\partial_{\boldsymbol{E}}\Omega^{\mathrm{mel}} - \partial_{\boldsymbol{E}}\Omega^{\mathrm{ele}} - \varepsilon_0\,J\,\boldsymbol{C}^{-1}\cdot\boldsymbol{E}\,.
\tag{14}
$$

We will assume ε_0 to be small compared to the remaining parameters so that the free space charge contribution is neglected.

When solving a set of non-linear equations, by means of Newton-type iteration schemes, including these electromechanical flux terms, we make use of the tangent operators which are defined in terms of second derivatives of Ω with respect to $\boldsymbol{C}$ and $\boldsymbol{E}$. In this regard, we introduce the elasticity related contributions

$$
\begin{aligned}
\mathbf{D}^{\mathrm{vol}} \;=\;& 4\,\frac{\partial^2 \Omega^{\mathrm{vol}}}{\partial\boldsymbol{C}\otimes\partial\boldsymbol{C}} \\
=\;& J\,[\,\partial_J \Omega^{\mathrm{vol}} + J\partial_{JJ}^2 \Omega^{\mathrm{vol}}\,]\,\boldsymbol{C}^{-1}\otimes\boldsymbol{C}^{-1} \\
& - J\,\partial_J \Omega^{\mathrm{vol}}\,[\,\boldsymbol{C}^{-1}\,\overline{\otimes}\,\boldsymbol{C}^{-1} + \boldsymbol{C}^{-1}\,\underline{\otimes}\,\boldsymbol{C}^{-1}\,]\,,
\end{aligned}
\tag{15}
$$

and

$$
\begin{aligned}
\mathbf{D}^{\mathrm{iso,mel}} \;=\;& 4\,\frac{\partial^2[\,\Omega^{\mathrm{iso}} + \Omega^{\mathrm{mel}}\,]}{\partial\boldsymbol{C}\otimes\partial\boldsymbol{C}} \\
=\;& 4\,J^{-4/3}\,\mathbf{P} : \partial^2_{\bar{\boldsymbol{C}}\otimes\bar{\boldsymbol{C}}}[\,\Omega^{\mathrm{iso}} + \Omega^{\mathrm{mel}}\,] : \mathbf{P}^{\mathrm{T}} \\
& + \tfrac{2}{3}\,J^{-2/3}\,\boldsymbol{C} : [\,\partial_{\bar{\boldsymbol{C}}}\Omega^{\mathrm{iso}} + \partial_{\bar{\boldsymbol{C}}}\Omega^{\mathrm{mel}}\,] \\
& \quad [\,\boldsymbol{C}^{-1}\,\overline{\otimes}\,\boldsymbol{C}^{-1} + \boldsymbol{C}^{-1}\,\underline{\otimes}\,\boldsymbol{C}^{-1} - \tfrac{2}{3}\,\boldsymbol{C}^{-1}\otimes\boldsymbol{C}^{-1}\,] \\
& - \tfrac{4}{3}\,J^{-2/3}\,\big[\,\boldsymbol{C}^{-1}\otimes[\,\partial_{\bar{\boldsymbol{C}}}\Omega^{\mathrm{iso}} + \partial_{\bar{\boldsymbol{C}}}\Omega^{\mathrm{mel}}\,] : \mathbf{P}^{\mathrm{T}} \\
& + \mathbf{P} : [\,\partial_{\bar{\boldsymbol{C}}}\Omega^{\mathrm{iso}} + \partial_{\bar{\boldsymbol{C}}}\Omega^{\mathrm{mel}}\,]\otimes\boldsymbol{C}^{-1}\,\big]\,,
\end{aligned}
\tag{16}
$$

by analogy with the so-called elasticity tensors within the framework of finite elasticity. Moreover, the tangent operator referred to second derivatives of Ω with respect to the electric field is defined as,

$$
\mathbf{D}^{\mathrm{mel,ele}} \;=\; \frac{\partial^2[\,\Omega^{\mathrm{mel}} + \Omega^{\mathrm{ele}}\,]}{\partial\boldsymbol{E}\otimes\partial\boldsymbol{E}}\,,
\tag{17}
$$

as well as a, say, mixed contribution

$$\mathbf{D}^{\mathrm{mel}} \,=\, -\,2\,\frac{\partial^2 \Omega^{\mathrm{mel}}}{\partial \boldsymbol{E} \otimes \partial \boldsymbol{C}} \,=\, -\,2\,J^{-2/3}\,\frac{\partial^2 \Omega^{\mathrm{mel}}}{\partial \boldsymbol{E} \otimes \partial \bar{\boldsymbol{C}}} : \mathbf{P}^{\mathrm{T}}\,. \tag{18}$$

3.2   Coupled micro-sphere formulation

As previously mentioned the main advantage of the so-called micro-sphere framework is the transformation of one-dimensional constitutive models to the general three-dimensional case. Such one-dimensional constitutive equations may enable to conveniently include a physically sound background into the model, even though we will not place particular emphasis on this aspect in this work. Furthermore, we restrict the proposed formulation to affine kinematics, but extend the micro-sphere formulation to the electromechanically coupled problem at hand. For more details on micro-sphere formulations see for instance Miehe et al. (2004); Alastrué et al. (2009a) and Alastrué et al. (2009b).

Conceptually speaking, the electromechanical flux terms, here $\boldsymbol{S}$ and $\boldsymbol{D}$, are evaluated by integration over the surface of the unit-sphere $\mathbb{U}^2$. In general, such integrations can not be performed analytically but are approximated by a numerical integration scheme, i.e.

$$\int_{\mathbb{U}^2} \bullet \, \mathrm{d}A \approx \sum_{i=1}^{m} \bullet_i \, w_i\,, \tag{19}$$

wherein $\bullet$ is a scalar quantity, the index i refers to a referential integration direction $\boldsymbol{r}_i \in \mathbb{U}^2$ so that $\bullet_i$ is the value of $\bullet$ in the direction of $\boldsymbol{r}_i$, and w_i represent non-negative integration weights constrained by $\sum_{i=1}^{m} w_i = 1$. Next the kinematic quantities of interest are referred to, or rather projected on, the integration directions, i.e.

$$\bar{\lambda}_i = \|\bar{\boldsymbol{F}} \cdot \boldsymbol{r}_i\| = \sqrt{\boldsymbol{r}_i \cdot \bar{\boldsymbol{C}} \cdot \boldsymbol{r}_i}\,, \tag{20}$$

$$E_i = \boldsymbol{E} \cdot \boldsymbol{r}_i\,. \tag{21}$$

Based on this, the free energy function is introduced within the micro-sphere context and we obtain

$$\Omega(\boldsymbol{F}, \boldsymbol{E}) \approx \Omega^{\mathrm{vol}}(J) + \sum_{i=1}^{m} [\,\Omega_i^{\mathrm{iso}}(\bar{\lambda}_i) + \Omega_i^{\mathrm{mel}}(\bar{\lambda}_i, E_i) + \Omega_i^{\mathrm{ele}}(E_i)\,]\, w_i\,, \tag{22}$$

with the free space contribution including the parameter ε_0 being neglected.

It is recalled that the electromechanical flux terms as well as the related tangent operators are directly based on derivatives of the free energy with respect to mechanical deformation tensors and the electric field. With eqs.(19)-(21) at hand, these derivatives are evaluated in the context of an affine micro-sphere formulation. In view of the derivatives present in the isochoric part of $\boldsymbol{S}$, eq. (13), we obtain

$$\frac{\partial \Omega^{\mathrm{iso}}}{\partial \bar{\boldsymbol{C}}} \,\approx\, \sum_{i=1}^{m} \frac{\partial \Omega_i^{\mathrm{iso}}}{\partial \bar{\lambda}_i^2}\, \frac{\partial \bar{\lambda}_i^2}{\partial \bar{\boldsymbol{C}}}\, w_i = \frac{1}{2} \sum_{i=1}^{m} \frac{1}{\bar{\lambda}_i}\, \frac{\partial \Omega_i^{\mathrm{iso}}}{\partial \bar{\lambda}_i}\, \boldsymbol{r}_i \otimes \boldsymbol{r}_i\, w_i\,, \tag{23}$$

7

and the micro-sphere-based evaluation of $\partial_{\bar{C}}\Omega^{\mathrm{mel}}$ follows by analogy. Note that the overall representation of $\boldsymbol{S}$ remains unaffected by the micro-sphere formulation and that solely the direct derivatives of Ω in eq. (13) have to be replaced. The micro-sphere-based representation of the electric displacements in eq. (14) leads to

$$-\frac{\partial\Omega^{\mathrm{mel}}}{\partial\boldsymbol{E}} \approx -\sum_{i=1}^{m}\frac{\partial\Omega_i^{\mathrm{mel}}}{\partial E_i}\frac{\partial E_i}{\partial\boldsymbol{E}}\,w_i = -\sum_{i=1}^{m}\frac{\partial\Omega_i^{\mathrm{mel}}}{\partial E_i}\,\boldsymbol{r}_i\,w_i\,, \tag{24}$$

and the representation of $-\partial_{\boldsymbol{E}}\Omega^{\mathrm{ele}}$ follows along the same lines of derivation. Note that not only the weighting factors w_i are constrained but also the integration directions, for instance by $\sum_{i=1}^{m}\boldsymbol{r}_i\,w_i = \boldsymbol{0}$. Practically speaking, any weighted summation over odd-order moments in $\boldsymbol{r}_i$ vanish identically, whereas weighted summations over even-order moments in $\boldsymbol{r}_i$ result in identity-type tensors. In fact, this property restricts $\partial_{E_i}\Omega_i^{\mathrm{mel}}$ to be of odd order in E_i. To give an example, let this derivative be linear in E_i. We then observe the relation $\sum_{i=1}^{m}E_i\,\boldsymbol{r}_i\,w_i = \sum_{i=1}^{m}\boldsymbol{E}\cdot\boldsymbol{r}_i\otimes\boldsymbol{r}_i\,w_i$ which, for $\boldsymbol{E}\neq\boldsymbol{0}$, does not vanish.

The general form of the tangent operators in eqs. (16)-(18) include first- and second-order derivatives to be specified within the micro-sphere context. The first-order derivatives are already included in the electromechanical flux terms, see eq. (23) and (24). The second-order derivatives present in the elasticity-type tensor in eq. (16) take the representation

$$\frac{\partial^2\Omega^{\mathrm{iso}}}{\partial\bar{\boldsymbol{C}}\otimes\partial\bar{\boldsymbol{C}}} \approx \frac{1}{4}\sum_{i=1}^{m}\frac{1}{\bar{\lambda}_i^2}\left[\frac{\partial^2\Omega_i^{\mathrm{iso}}}{\partial\bar{\lambda}_i\,\partial\bar{\lambda}_i} - \frac{1}{\bar{\lambda}_i}\frac{\partial\Omega_i^{\mathrm{iso}}}{\partial\bar{\lambda}_i}\right]\boldsymbol{r}_i\otimes\boldsymbol{r}_i\otimes\boldsymbol{r}_i\otimes\boldsymbol{r}_i\,w_i\,. \tag{25}$$

and the micro-sphere form of $\partial^2_{\bar{\boldsymbol{C}}\otimes\bar{\boldsymbol{C}}}\Omega^{\mathrm{mel}}$ follows by analogy. The second-order derivatives with respect to $\boldsymbol{E}$, as included in eq. (17), now result in

$$\frac{\partial^2\Omega^{\mathrm{mel}}}{\partial\boldsymbol{E}\otimes\partial\boldsymbol{E}} \approx \sum_{i=1}^{m}\frac{\partial^2\Omega_i^{\mathrm{mel}}}{\partial E_i\,\partial E_i}\,\boldsymbol{r}_i\otimes\boldsymbol{r}_i\,w_i\,. \tag{26}$$

Note that $\partial^2_{E_i\,E_i}\Omega_i^{\mathrm{mel}}$ must be of even order in E_i so that $-\partial^2_{\boldsymbol{E}\otimes\boldsymbol{E}}\Omega^{\mathrm{mel}}$ does not vanish. The same form as in eq. (26) is also applied to the representation of $-\partial^2_{\boldsymbol{E}\otimes\boldsymbol{E}}\Omega^{\mathrm{ele}}$. In view of the, say, mixed contribution in eq. (18), we obtain

$$-\frac{\partial^2\Omega^{\mathrm{mel}}}{\partial\boldsymbol{E}\otimes\partial\bar{\boldsymbol{C}}} \approx -\frac{1}{2}\sum_{i=1}^{m}\frac{1}{\bar{\lambda}_i}\frac{\partial^2\Omega_i^{\mathrm{mel}}}{\partial E_i\,\partial\bar{\lambda}_i}\,\boldsymbol{r}_i\otimes\boldsymbol{r}_i\otimes\boldsymbol{r}_i\,w_i\,. \tag{27}$$

Note that $\partial^2_{E_i\,\bar{\lambda}_i}\Omega_i^{\mathrm{mel}}$ must be of odd order in E_i so that $-\partial^2_{\boldsymbol{E}\otimes\bar{\boldsymbol{C}}}\Omega^{\mathrm{mel}}$ does not vanish.

4   Numerical examples

To show the applicability of the proposed model, several numerical examples are used for illustrative purposes. To set the stage, we first specify the particular free energy

Table 1: First and second derivatives of the free energy function of the micro-sphere model.

$$
\begin{aligned}
\partial_J \Omega^{\mathrm{vol}} &= \kappa^* [\, J - 1 \,] & \partial^2_{JJ} \Omega^{\mathrm{vol}} &= \kappa^* \\
\partial_{\bar\lambda_i} \Omega^{\mathrm{iso}} &= \mu^* \bar\lambda_i & \partial^2_{\bar\lambda_i \bar\lambda_i} \Omega^{\mathrm{iso}} &= \mu^* \\
\partial_{\bar\lambda_i} \Omega^{\mathrm{mel}} &= 2\, c_1^* \bar\lambda_i E_i^2 & \partial^2_{\bar\lambda_i \bar\lambda_i} \Omega^{\mathrm{mel}} &= 2\, c_1^* E_i^2 & \partial^2_{\bar\lambda_i E_i} \Omega^{\mathrm{mel}} &= 4\, c_1^* \bar\lambda_i E_i \\
\partial_{E_i} \Omega^{\mathrm{mel}} &= 2\, c_1^* \bar\lambda_i^2 E_i & \partial^2_{E_i E_i} \Omega^{\mathrm{mel}} &= 2\, c_1^* \bar\lambda_i^2 & \partial^2_{E_i \bar\lambda_i} \Omega^{\mathrm{mel}} &= \partial^2_{\bar\lambda_i E_i} \Omega^{\mathrm{mel}} \\
\partial_{E_i} \Omega^{\mathrm{ele}} &= 2\, c_2^* E_i & \partial^2_{E_i E_i} \Omega^{\mathrm{ele}} &= 2\, c_2^*
\end{aligned}
$$

function and thereafter investigate the response of the model by means of two homogeneous deformations and two boundary value problems undergoing inhomogeneous deformations which are solved within a coupled finite element framework. The nodal degrees of freedom used for the finite element formulation are the motion $\boldsymbol{\varphi}$ of the body as well as the electric potential ϕ. As both degrees of freedom enter the electromechanical fluxes solely in terms of their first-order gradients in space, identical approximation function are used for both fields. To be specific, we use standard linear Lagrange polynomials. For the numerical integration on the micro-sphere, we adopt the simplest but efficient integration scheme with 21 integration directions for the hemisphere so that $m = 42$; cf. Bažant and Oh (1986) or Alastrué et al. (2009a), and references cited therein, for the comparison of different integration schemes.

4.1 Free energy for the micro-sphere model

In general, the free energy function in eq. (22) can be motivated based on a sound physical background such as statistical mechanics common within, for instance, worm-like-chain-type models. As the main focus of this work, however, is to establish a micro-sphere formulation for electromechanically coupled problems, we choose a neo-Hooke-type elastic contribution in combination with terms quadratic in the electric field. In view of the micro-sphere model, cf. eq. (22), we obtain

$$
\begin{aligned}
\Omega^{\mathrm{vol}}(J) &= \tfrac{1}{2}\, \kappa^* [\, J - 1 \,]^2\,, \\
\Omega^{\mathrm{iso}}_i(\bar\lambda_i) &= \tfrac{1}{2}\, \mu^* [\, \bar\lambda_i^2 - 1 \,]\,, \\
\Omega^{\mathrm{mel}}_i(\bar\lambda_i, E_i) &= c_1^* \bar\lambda_i^2 E_i^2\,, \\
\Omega^{\mathrm{ele}}_i(E_i) &= c_2^* E_i^2\,.
\end{aligned}
\tag{28}
$$

Based on these specifications, the first and second order derivatives, required to determine the electromechanical flux terms and related tangent operators, can be calculated. For convenience of the reader, these derivatives are summarised in table 1.

Furthermore, the material parameters κ^*, μ^*, c_1^*, and c_2^* must be specified. We make use of the parameters κ, μ, and c_1 identified for polyurethane by Ask et al.

Table 2: Material parameters for the continuum model, taken from Ask et al. (2012b), (left) and for the micro-sphere model (right).

$$
\begin{array}{llll}
\kappa = 6.1 & [\text{MPa}] & \kappa^* = 6.1 & [\text{MPa}] \\
\mu = 1.307 & [\text{MPa}] & \mu^* = 3.921 & [\text{MPa}] \\
c_1 = 1.763 \times 10^{-9} & [\text{NV}^{-2}] & c_1^* = 5.289 \times 10^{-9} & [\text{NV}^{-2}] \\
c_2 = 2.938 \times 10^{-9} & [\text{NV}^{-2}] & c_2^* = 8.815 \times 10^{-9} & [\text{NV}^{-2}]
\end{array}
$$

(2012b) but, in this case, transfer these parameters to the micro-sphere model. The relationship between c_1 and c_2 has been identified from Vu et al. (2007), who use a similar constitutive model, so that $c_2^* = c_1^*/0.6$. The specific values are summarised in table 2. A short discussion on the relation between the micro-sphere-related material parameters and the material parameters of the continuum model is included in appendix A, which provides an alternative to directly identify the material parameters of the coupled micro-sphere model.

4.2 Homogeneous deformation

The first two examples are discussed in order to show that the chosen energy function together with the micro-sphere formulation produces physically sound results. To illustrate two different homogeneous deformations, consider a cubical specimen with initial or rather referential dimensions $L \times W \times H = 1 \times 1 \times 1$ [mm].

4.2.1 Compression

In the first example under homogeneous deformation we apply electrical Dirichlet boundary conditions so that a homogeneous electric field is obtained. The Cartesian x-axis is chosen to be aligned with this constant loading direction so that $\boldsymbol{E} = E_x \, \boldsymbol{e}_x = -\Delta\phi/L$. The stretches $\lambda_x = l/L$ and $\lambda_y = \lambda_z = w/W = h/H$ are considered, wherein l, w and h refer to actual or rather spatial dimensions of the specimen, i.e. $l \times w \times h$. Two different displacement Dirichlet boundary conditions are investigated; first we constrain the deformation in the x-direction so that $\lambda_x = 1$ and next, we study the unconstrained and stress-free state. Moreover, the total Piola-type stresses projected on the electrical loading direction, $T_{xx} = \boldsymbol{e}_x \cdot \boldsymbol{T} \cdot \boldsymbol{e}_x$, as well as the electric displacements $D_x = \boldsymbol{D} \cdot \boldsymbol{e}_x$ are considered. The difference in electric potential is linearly decreased from zero to -10 [kV]. Related simulation results are displayed in figures 1-2. Figure 1(a) highlights the relation between the total stress T_{xx} and the electric field E_x for $\lambda_x = 1$. The electrostrictive response at low loading levels, in other words T_{xx} is quadratic in E_x, is clearly shown in this figure, which reflects that the micro-sphere formulation is able to capture electrostrictive response. Due to the low value of c_2^* the value of the total stress T_{xx} remains rather small. Figure 1(b) shows the relation between the the total stress T_{xx} and the transversal stretches $\lambda_y = \lambda_z$ which, for the constrained case considered here, remain rather small within the considered loading
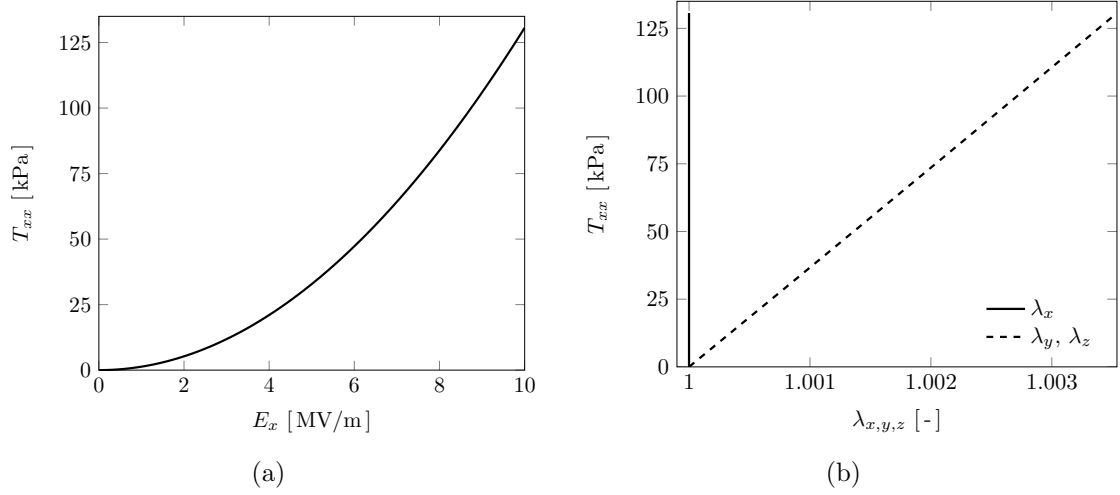
10

Figure 1: Homogeneous deformation, compression for $\lambda_x = 1$: 1(a) longitudinal total stress T_{xx} plotted vs. longitudinal electric field E_x;1(b) longitudinal total stress T_{xx} plotted vs. transverse stretches λ_y and λ_z.
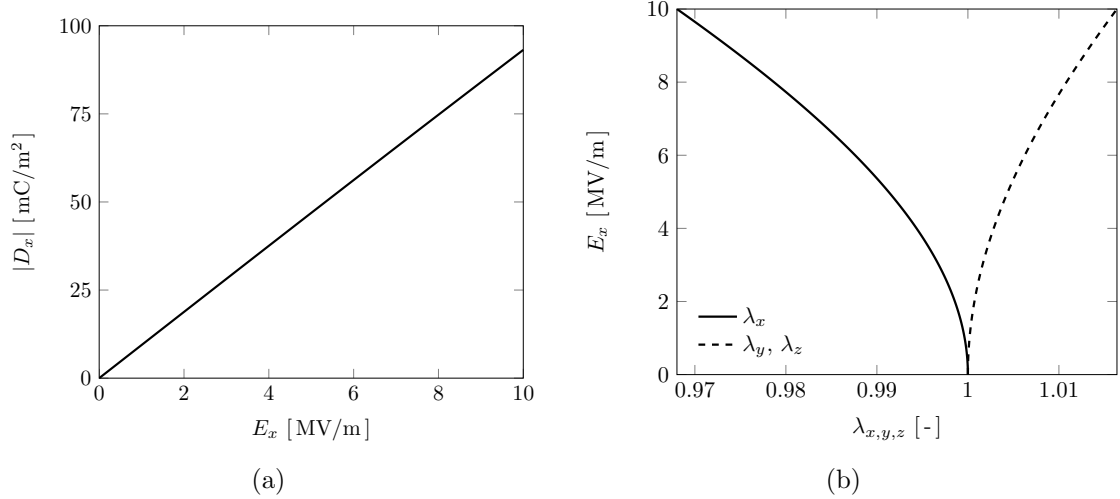

Figure 2: Homogeneous deformation, compression for unconstrained and stress-free state: 2(a) absolute value of longitudinal electric displacement D_x plotted vs. longitudinal electric field E_x; 2(b) longitudinal electric field E_x plotted vs. longitudinal stretch λ_x and transverse stretches λ_y and λ_z.

range. Furthermore, figure 2(a) shows that the micro-sphere formulation allows to include a linear relation between the electric field E_x and the electric displacement D_x for the unconstrained case. This —together with the results visualised in figure 1(a)— reflects that the modelling framework proposed is physically sound. Figure 2(b) shows the relation between the electric field E_x and the stretches of the unconstrained case where a nonlinear relation is additionally highlighted. As the activation of the electric field results in compression with respect to this loading direction, λ_x decreases with increasing absolute values of E_x, whereas the transverse stretches $\lambda_y = \lambda_z$ increase.

4.2.2 Shear

In the second example under homogeneous deformation we shear the specimen $L \times W \times H$ in the x-z plane such that $\boldsymbol{F} = \boldsymbol{I} + \gamma \boldsymbol{e}_x \otimes \boldsymbol{e}_z$, while we simultaneously apply a linearly decreasing difference in electric potential to those surfaces perpendicular to the z-axis such that $\boldsymbol{E} = E_z \boldsymbol{e}_z = -\Delta\phi/H \, \boldsymbol{e}_z$. The specimen is sheared to a maximum of $\gamma = 0.0997$ and two different electrical loadings of $\Delta\phi$ are applied. The total Piola-type stress components $T_{xz} = \boldsymbol{e}_x \cdot \boldsymbol{T} \cdot \boldsymbol{e}_z$ and $T_{zz} = \boldsymbol{e}_z \cdot \boldsymbol{T} \cdot \boldsymbol{e}_z$ are plotted against the shear number for two different values of electrical loading, i.e. $\Delta\phi = -10$ [kV] and $\Delta\phi = -20$ [kV], see figures 3(a) and 3(b) respectively. The case of $\Delta\phi = 0$ [V] is also included to emphasis the influence of the electrical loading.

(a)   (b)
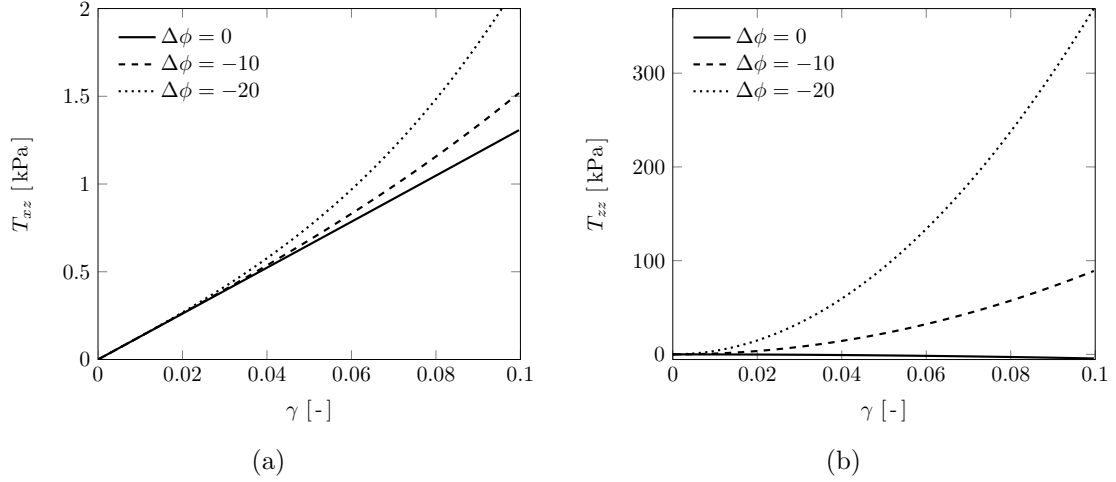
Figure 3: Homogeneous deformation, shear: 3(a) total stress $T_{xz} = \boldsymbol{e}_x \cdot \boldsymbol{T} \cdot \boldsymbol{e}_z$ plotted vs. shear γ for different electrical loading levels $\Delta\phi$ [kV]; 3(b) total stress $T_{zz} = \boldsymbol{e}_z \cdot \boldsymbol{T} \cdot \boldsymbol{e}_z$ plotted vs. shear γ for different electrical loading levels $\Delta\phi$ [kV].

4.3 Plate with hole

To further illustrate the numerical approach when the proposed micro-sphere formulation is used, the inhomogeneous deformation of a plate with a hole is studied. The plate is 120 [mm] long, 40 [mm] wide and 10 [mm] thick. The hole is placed in the centre of the plate with a radius of 10 [mm]. Due to symmetry conditions, only one eighth of the plate is discretised with 122 finite elements. Concerning the loading conditions, we apply a maximum difference in electric potential of $\Delta\phi = 200$ [V] between the two free surfaces of dimension 40×10 [mm]. In order to amplify the deformation—for the purpose of illustration and to activate finite strain states under purely electrical loading—the material parameter c_1^* is increased to the rather non-physical value of 30 [NV^2]. Illustrations of the undeformed specimen with initial dimensions and the electrical loading conditions are given in figure 4. A representative deformation versus loading curve is provided in figure 5. To be specific, the change in distance between two opposite midpoints of the surfaces with prescribed electric potential is plotted

versus the difference in prescribed electric potential $\Delta\phi$. The initial positions of the nodes considered are given by

(i) $X_x^{\Delta x} = \pm\, 20$ [mm] $X_y^{\Delta x} = 60$ [mm] $X_z^{\Delta x} = 0$ [mm]   for $\Delta x'$

(ii) $X_x^{\Delta y} = 0$ [mm] $X_y^{\Delta y} = \pm\, 60$ [mm] $X_z^{\Delta y} = 0$ [mm]   for $\Delta y'$

(iii) $X_x^{\Delta z} = 0$ [mm] $X_y^{\Delta z} = 60$ [mm] $X_z^{\Delta z} = \pm\, 5$ [mm]   for $\Delta z'$

Figure 5 clearly reflects the large strain regime as well as the overall non-linearity of the problem at hand. At small loading levels of $\Delta\phi$ the reduction in longitudinal end-to-end distance, $-\Delta y|_{\boldsymbol{X}^{\Delta y}}$, turns out to non-linearly increase with $\Delta\phi$, while the overall compression state renders the longitudinal end-to-end distance to almost saturate at large loading levels of $\Delta\phi$. We emphasise that this example is made to demonstrate the robustness of the model and will, due to the unrealistically high value of c_1^*, produce large deformations with respect to the actual loading level. Deformed states and respective meshes are highlighted in figure 6 for different electrical loading levels, i.e. $\Delta\phi \in \{50, 100, 200\}$ [V]. In order to further emphasise the inhomogeneous state of deformation, the contour plots in figures 6(a) and 6(b) refer to the projections in longitudinal direction of the spatial total stresses $\boldsymbol{\tau}$ and the electric field $\boldsymbol{E}$, which clearly reflect the inhomogeneous state of deformation.
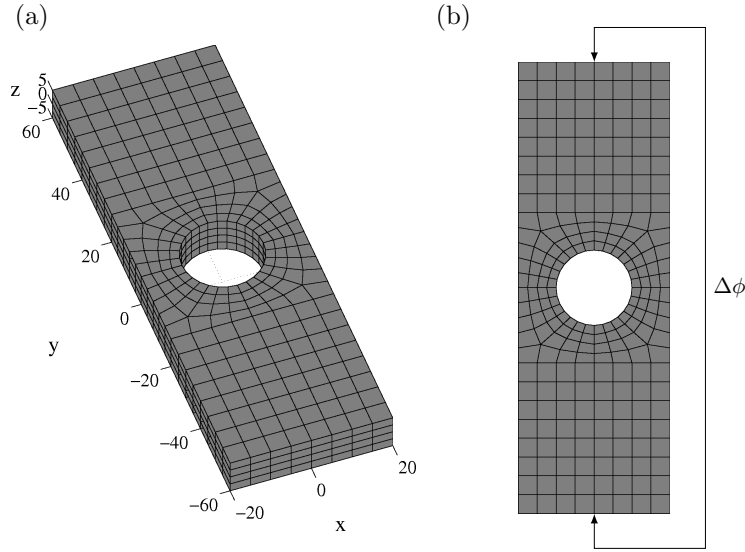

Figure 4: Plate with hole: (a) undeformed mesh with initial dimensions [mm]; (b) electrical boundary conditions.

4.4   Beam-like actuator

This example mimics the behaviour of an electro-active actuator, one of the most common applications of electro-active polymers. The actuator we simulate is built up by sandwiching EAP between two electrodes and thereby enabling the generation of large deformations at moderate strains. The geometry of the actuator is chosen such
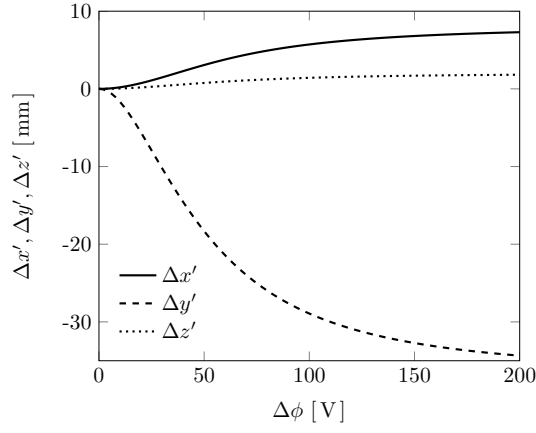
Figure 5: Plate with hole: change in distance in $x-$, $y-$ and $z-$direction, referred to the mechanical displacement of two opposite mid-nodes at the surfaces with prescribed electric potential, vs. the difference in electric potential $\Delta\phi$.
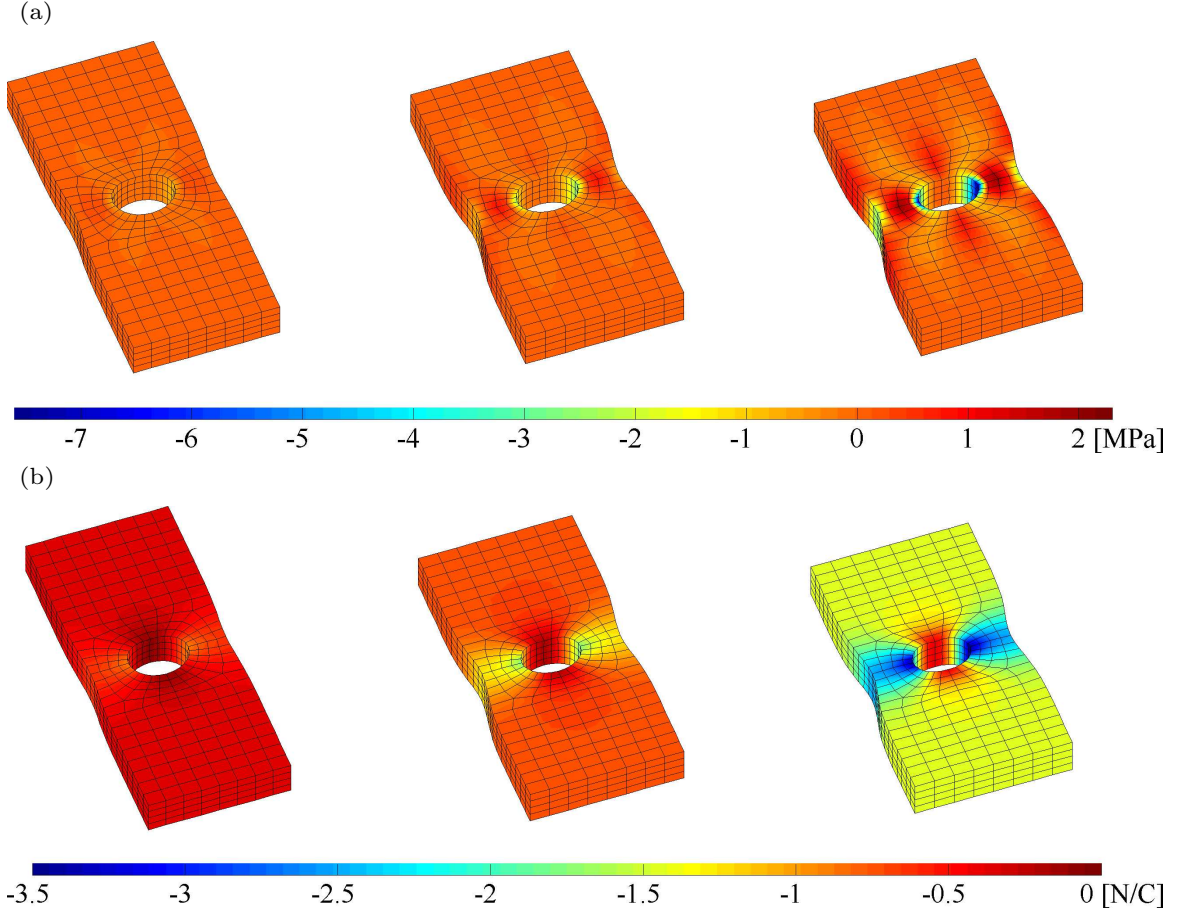
(a)

(b)

Figure 6: Plate with hole: 6(a) contourplots of the spatial total stress $\boldsymbol{\tau}$ projected in longitudinal direction, $\tau_{yy} = \boldsymbol{e}_y \cdot \boldsymbol{\tau} \cdot \boldsymbol{e}_y$, for deformed meshes at $\Delta\phi = \{50, 100, 200\}$ [V]; 6(b) contourplots of electric field $\boldsymbol{E}$ projected in longitudinal direction, $E_y = \boldsymbol{E} \cdot \boldsymbol{e}_y$, for deformed meshes at $\Delta\phi = \{50, 100, 200\}$ [V].

14

that the specimen is 50 [mm] long, 4 [mm] wide and 1 [mm] thick. The beam is fully clamped at one of its ends. The electric potential is prescribed in the mid layer of the beam, $\phi_{\mathrm{mid}} = 0$, as well as on the top surface of the beam, $\phi_{\mathrm{top}} > 0$. An illustration of the geometry and the boundary conditions is shown in figure 7. The Cartesian axes are chosen so that the x-axis coincides with the undeformed longitudinal direction of the beam and undeformed cross-sections are aligned with the y-z-plane. A maximum difference in electric potential $\Delta\phi = \phi_{\mathrm{top}} - \phi_{\mathrm{mid}}$ of 5 [kV] is prescribed. Due to symmetry conditions, only half of the beam is simulated with a total number of 2160 finite elements. The displacements $\boldsymbol{u}$ in x- and z-direction at the beam tip versus the difference in prescribed electric potential $\Delta\phi$ are shown in figure 8. Moreover, figure 9 visualises the deformation of the beam at a loading level of $\Delta\phi = 2.5$ [kV] and $\Delta\phi = 5$ [kV]. The contour plots refer to the electric potential which, in terms of its gradient, clearly reflects the distribution of the electric field.
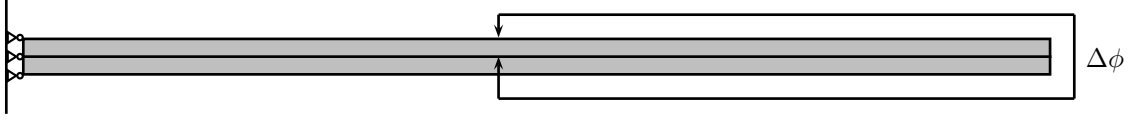

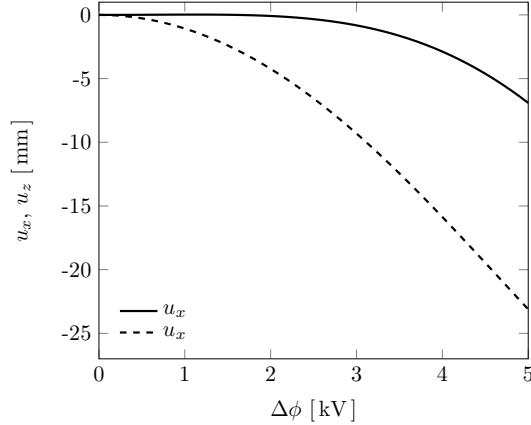**Figure 7:** Beam-like actuator: boundary and loading conditions of the beam-like actuator example.

Figure 8: Beam-like actuator: displacement u_x and u_z at the tip of the beam vs. the difference in prescribed electric potential $\Delta\phi$.

5   Summary

We established a coupled micro-sphere framework for nonlinear electroelasticity in combination with the finite element method. The computational model is shown to be suitable to capture the behaviour of electrostrictive polymers and to simulate physically sound electromechanical response. We fitted the material parameters of the coupled micro-sphere model to those previously identified for an electromechanically coupled continuum model applied to the modelling of polyurethane. The coupled
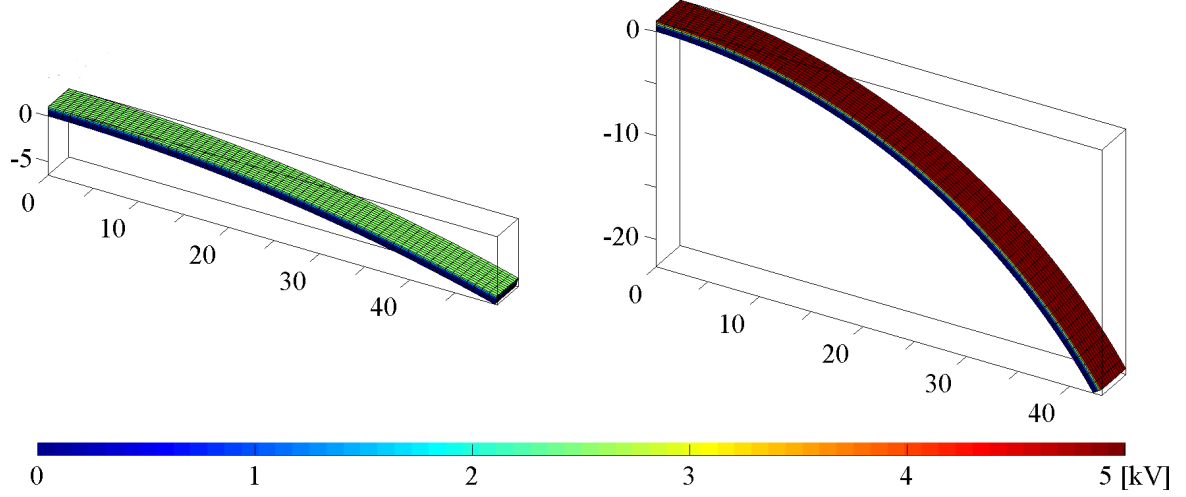
Figure 9: Beam-like actuator: contourplots of the electric potential ϕ on deformed meshes for $\Delta\phi = 2.5$ [kV] and $\Delta\phi = 5$ [kV].

micro-sphere framework established in this work has the main advantage to enable the extension of physics-based one-dimensional constitutive equations, such as the worm like chain model, to the three-dimensional continuum level. The investigation and algorithmic formulation of such micro-electromechanical models, along with the incorporation of dissipation effects such as viscosity, constitute key aspects of future research.

Acknowledgements

A   Material parameters at the micro-sphere level

The material parameters used for the electromechanically coupled micro-sphere model in this work are motivated by those identified in Ask et al. (2012b) where use of the following free energy contributions is made

$$
\begin{aligned}
\Omega^{\text{iso}}(\bar{\boldsymbol{F}}) &= \tfrac{1}{2}\,\mu\,[\,\bar{\boldsymbol{C}} : \boldsymbol{I} - 3\,]\,, \\
\Omega^{\text{mel}}(\bar{\boldsymbol{F}}, \boldsymbol{E}) &= c_1\,\boldsymbol{E} \cdot \bar{\boldsymbol{C}} \cdot \boldsymbol{E}\,, \\
\Omega^{\text{ele}}(\boldsymbol{E}) &= c_2\,\boldsymbol{E} \cdot \boldsymbol{E}\,.
\end{aligned}
\tag{29}
$$

To relate the parameters μ and μ^* we compute the contribution of the respective

16

parameters to the Piola-Kirchhoff stresses. This results in

$$2\frac{\partial \Omega^{\text{iso}}}{\partial \bar{\boldsymbol{C}}} = \mu\,\boldsymbol{I}\,,$$

$$2\sum_{i=1}^{m} \frac{\partial \Omega_i^{\text{iso}}}{\partial \bar{\boldsymbol{C}}}\,w_i = \mu^*\sum_{i=1}^{m} \boldsymbol{r}_i \otimes \boldsymbol{r}_i\,w_i = \frac{1}{3}\,\mu^*\,\boldsymbol{I}\,, \tag{30}$$

from which we conclude that

$$\mu^* \equiv 3\,\mu\,. \tag{31}$$

Eq. (30) includes that the numerical integration scheme on the unit-sphere is restricted to result in a spherical second-order moment of the integration directions, the trace of which is one, in other words $\sum_{i=1}^{m} \boldsymbol{r}_i \otimes \boldsymbol{r}_i\,w_i = \frac{1}{3}\,\boldsymbol{I}$.

We proceed along the same lines of derivation to relate c_2 and c_2^* but now compare the tangent operators related to the purely electric contribution. To be specific

$$\frac{\partial^2 \Omega^{\text{ele}}}{\partial \boldsymbol{E} \otimes \partial \boldsymbol{E}} = 2\,c_2\,\boldsymbol{I}\,,$$

$$\sum_{i=1}^{m} \frac{\partial^2 \Omega_i^{\text{ele}}}{\partial \boldsymbol{E} \otimes \boldsymbol{E}}\,w_i = 2\,c_2^*\sum_{i=1}^{m} \boldsymbol{r}_i \otimes \boldsymbol{r}_i\,w_i = \frac{2}{3}\,c_2^*\,\boldsymbol{I}\,, \tag{32}$$

so that

$$c_2^* \equiv 3\,c_2\,. \tag{33}$$

We obtain the same relation for c_1 and c_1^* when evaluation the, say, coupling term within the energy functions at the initial state of deformation, i.e. $\boldsymbol{F} = \boldsymbol{I}$. In this context we obtain

$$\left.\frac{\partial^2 \Omega^{\text{mel}}}{\partial \boldsymbol{E} \otimes \partial \boldsymbol{E}}\right|_{\boldsymbol{F}=\boldsymbol{I}} = 2\,c_1\,\boldsymbol{I}\,,$$

$$\sum_{i=1}^{m} \left.\frac{\partial^2 \Omega_i^{\text{mel}}}{\partial \boldsymbol{E} \otimes \boldsymbol{E}}\right|_{\boldsymbol{F}=\boldsymbol{I}}\,w_i = 2\,c_1^*\sum_{i=1}^{m} \boldsymbol{r}_i \otimes \boldsymbol{r}_i\,w_i = \frac{2}{3}\,c_1^*\,\boldsymbol{I}\,, \tag{34}$$

so that

$$c_1^* \equiv 3\,c_1\,. \tag{35}$$

Finally, the purely volumetric elastic contribution to the free energy is assumed not to be affected by the micro-sphere kinematics. In consequence, we assume

$$\kappa^* \equiv \kappa\,, \tag{36}$$

whereby κ is a penalty-type compression modulus related—in case of a standard continuum model—to the Poisson ratio via $\nu = [\,3\,\kappa - 2\,\mu\,]/[\,6\,\kappa + 2\,\mu\,]$.

17

References

Alastrué, V., Martínez, M., Doblaré, M., Menzel, A., 2009a. Anisotropic micro-sphere-based finite elasticity applied to blood vessel modelling. J. Mech. Phys. Solids 57 (1), 178–203.

Alastrué, V., Martínez, M. A., Menzel, A., Doblaré, M., 2009b. On the use of non-linear transformations for the evaluation of anisotropic rotationally symmetric directional integrals. Application to the stress analysis in fibred soft tissues. Int. J. Numer. Methods Engng 79 (4), 474–504.

Ask, A., Menzel, A., Ristinmaa, M., 2010. On the modelling of electro-viscoelastic response of electrostrictive polyurethane elastomers. IOP Conf. Ser.: Mater. Sci. Engng. 10 (1), 012101.

Ask, A., Menzel, A., Ristinmaa, M., 2012a. Electrostriction in electro-viscoelastic polymers. Mech. Mater. 50, 9–21.

Ask, A., Menzel, A., Ristinmaa, M., 2012b. Phenomenological modeling of viscous electrostrictive polymers. Int. J. Non-Linear Mech. 47 (2), 156–165.

Bar-Cohen, Y. (Ed.), 2004. Electroactive Polymer (EAP) Actuators as Artificial Muscles: Reality, Potential, and Challenges, 2nd Edition. SPIE Press.

Bar-Cohen, Y., Sherrit, S., Lih, S.-S., 2001. Characterization of the electromechanical properties of EAP materials. Proc. SPIE 4329, 319–327.

Bažant, Z. P., Oh, B. H., 1983. Microplane model for fracture analysis of concrete structures. Proc. Symp. Interact. Non-Nucl. Munitions Struct., 49–55.

Bažant, Z. P., Oh, B. H., 1986. Efficient numerical integration on the surface of a sphere. Z. Angew. Math. Mech. 66 (1), 37–49.

Beatty, M. F., 1987. A class of universal relations in isotropic elasticity theory. J. Elasticity 17 (2), 113–121.

Bertoldi, K., Gei, M., 2011. Instabilities in multilayered soft dielectrics. J. Mech. Phys. Solids 59 (1), 18–42.

Blythe, T., Bloor, D., 2005. Electrical Properties of Polymers. Cambridge University Press.

Bobbio, S., 2000. Electrodynamics of Materials – Forces, Stresses, and Energies in Solids and Fluids. Academic Press.

Carol, I., Jirásek, M., Bažant, Z., 2001. A thermodynamically consistent approach to microplane theory. Part I. Free energy and consistent microplane stresses. Int. J. Solids Struct. 38 (17), 2921–2931.

Carpi, F., Kornbluh, R., Sommer-Larsen, P., Alici, G., 2011. Electroactive polymer actuators as artificial muscles: are they ready for bioinspired applications? Bioinsp. Biomim 6 (4), 045006.

Diaconu, I., Dorohoi, D.-O., Ciobanu, C., 2008. Electromechanical response of polyurethane films with different thickness. Rom. J. Physics 53, 91–97.

Dorfmann, A., Ogden, R. W., 2005. Nonlinear electroelasticity. Acta Mech. 174 (3), 167–183.

Dorfmann, A., Ogden, R. W., 2006. Nonlinear electroelastic deformations. J. Elasticity 82 (2), 99–127.

Eringen, A. C., 1989. Mechanics of Continua. Krieger.

Eringen, A. C., Maugin, G. A., 1990. Electrodynamics of Continua I – Foundations and Solid Media. Springer.

Hirano, L. A., Escote, M. T., Martins-Filho, L. S., Mantovani, G. L., Scuracchio, C. H., 2011. Development of Artificial Muscles Based on Electroactive Ionomeric Polymer-Metal Composites. Artificial Organs 35 (5), 478–483.

Hong, W., 2011. Modeling viscoelastic dielectrics. J. Mech. Phys. Solids 59 (3), 637–650.

Kornbluh, R., Pelrine, R., Eckerle, J., Joseph, J., May 1998. Electrostrictive polymer artificial muscle actuators. Proc. 1998 IEEE Int. Conf. on Robotics and Automation 3, 2147–2154.

Kovetz, A., 2000. Electromagnetic Theory. Oxford University Press.

Kuhl, E., Menzel, A., Garikipati, K., 2006. On the convexity of transversely isotropic chain network models. Phil. Mag. 86 (21-22), 3241–3258.

Kuhl, E., Steinmann, P., Carol, I., 2001. A thermodynamically consistent approach to microplane theory. Part II. Dissipation and inelastic constitutive modeling. Int. J. Solids Struct. 38 (17), 2933–2952.

Kwang, J. K., Tadokoro, S. (Eds.), 2007. Electroactive Polymers for Robotic Applications – Artificial Muscles and Sensors. Springer.

Maugin, G. A., 1988. Continuum Mechanics of Electromagnetic Solids. Vol. 33 of Applied Mathematics and Mechanics. North-Holland.

McMeeking, R. M., Landis, C. M., 7 2005. Electrostatic forces and stored energy for deformable dielectric materials. ASME J. Appl. Mech. 72 (4), 581–590.

McMeeking, R. M., Landis, C. M., Jimenez, S. M., 2007. A principle of virtual work for combined electrostatic and mechanical loading of materials. Int. J. Non-Linear Mech. 42 (6), 831–838.

Menzel, A., Waffenschmidt, T., 2009. A microsphere-based remodelling formulation for anisotropic biological tissues. Phil. Trans. R. Soc. A 367 (1902), 3499–3523.

Miehe, C., Göktepe, S., 2005. A micro–macro approach to rubber-like materials. Part II: The micro-sphere model of finite rubber viscoelasticity. J. Mech. Phys. Solids 53 (10), 2231–2258.

Miehe, C., Göktepe, S., Lulei, F., 2004. A micro-macro approach to rubber-like materials—Part I: the non-affine micro-sphere model of rubber elasticity. J. Mech. Phys. Solids 52 (11), 2617–2660.

Nalwa, H. S. (Ed.), 1995. Ferroelectric Polymers: Chemistry: Physics, and Applications. Dekker.

Ogden, R. W., Saccomandi, G., Sgura, I., 2006. On worm-like chain models within the three-dimensional continuum mechanics framework. Proc. R. Soc. A 462 (2067), 749–768.

Ogden, R. W., Steigmann, D. J., 2011. Mechanics and Electrodynamics of Magneto- and Electro-Elastic Materials. No. 527 in CISM Courses and Lectures. Springer.

Potter, M., Gouder, K., Morrison, J. F., 2011. A numerical model for electro-active polymer actuators with experimental validation. Sens. Act. A: Phys. 170 (1–2), 121–130.

Rudykh, S., deBotton, G., 2011. Stability of anisotropic electroactive polymers with application to layered media. Z. Angew. Math. Phys. 62 (6), 1131–1142.

Smith, R. C., 2005. Smart Material Systems – Model Development. Frontiers in Applied Mathematics. SIAM.

Suo, Z., 2010. Theory of dielectric elastomers. Acta Mech. Solida Sinica 23 (6), 549–578.

Tian, L., Tevet-Deree, L., deBotton, G., Bhattacharya, K., 2012. Dielectric elastomer composites. JMPS 60 (1), 181–198.

Vu, D. K., Steinmann, P., 2012. On 3-D coupled BEM–FEM simulation of nonlinear electro-elastostatics. Comput. Methods Appl. Mech. Engng. 201, 82–90.

Vu, D. K., Steinmann, P., Possart, G., 2007. Numerical modelling of non-linear electroelasticity. Int. J. Numer. Methods Engng 70 (6), 685–704.

Waffenschmidt, T., Menzel, A., 2012. Application of an anisotropic growth and remodelling formulation to computational structural design. Mech. Res. Comm. 42, 77–86.

Waffenschmidt, T., Menzel, A., Kuhl, E., 2012. Anisotropic density growth of bone—A computational micro-sphere approach. Int. J. Solids Struct. 49 (14), 1928–1946.

Wissler, M., Mazza, E., 2005. Modeling and simulation of dielectric elastomer actuators. Smart Mater. Struct. 14 (6), 1396–1402.

York, A., Dunn, J., Seelecke, S., 2010. Experimental characterization of the hysteretic and rate-dependent electromechanical behavior of dielectric electro-active polymer actuators. Smart Mater. Struct. 19 (9), 094014.

Paper B

S. Thylander, A. Menzel and M. Ristinmaa

A non-affine electro-viscoelastic microsphere model for dielectric elastomers: application to VHB 4910 based actuators

A non-affine electro-viscoelastic microsphere model for dielectric elastomers: Application to VHB 4910 based actuators

Sara Thylander[a], Andreas Menzel[a,b] and Matti Ristinmaa[a]

[a] Division of Solid Mechanics, Lund University

P.O. Box 118, S-221 00 Lund, Sweden

[b] Department of Mechanical Engineering, Institute of Mechanics, TU Dortmund

Leonhard-Euler-Str. 5, D-44227 Dortmund, Germany

Abstract

Dielectric elastomers belong to a larger group of materials, the so-called electroactive polymers, which have the capability of transforming electric energy to mechanical energy through deformation. VHB 4910 is one of the most popular materials for applications of dielectric elastomers and therefore one of the most investigated. This paper includes a new micromechanically motivated constitutive model for dielectric elastomers that incorporates nearly incompressible and viscous time-dependent behaviour often found in this type of material. A non-affine micro-sphere framework is used to transform the microscopic constitutive model to a macroscopic continuum counterpart. Furthermore the model is calibrated, through both homogeneous deformation examples and more complex finite element analysis, to VHB 4910. The model is able to capture both the purely elastic, the viscoelastic and the electro-viscoelastic properties of the elastomer and demonstrates the power and applicability of the electromechanically coupled micro-sphere framework.

1 Introduction

Electroactive polymers (EAPs) include a large variety of polymers that react to electric stimuli with deformation by different types of electromechanical coupling (such as piezo- or ferro-electrics) which all offer different advantages and disadvantages. One of the more common applications for EAPs are as actuators. It is often compared to existing actuator technologies such as shape memory alloys, which gives relatively large deformations but are slow compared to EAP, or to electroactive ceramics, which are fast but give small deformations compared to EAP, see Kornbluh et al. (2000). In terms of EAPs as actuators, one specifically interesting subgroup of EAP are the so-called dielectric elastomers (DEs). Dielectric elastomer actuators (DEAs) offer a good alternative with its combination of large strain, scalability, fast response and high efficiency, see for example Kornbluh et al. (2000); Pelrine et al. (2000a) and Pelrine et al. (2001b). Furthermore, there are also the purely elastomeric benefits of inexpensive production, commercial availability, high fracture tolerance, lightweight and easy fabrication into various complex shapes.

A DEA basically acts as a variable capacitor consisting of a thin elastomeric sheet sandwiched between two compliant electrodes. As an electric field is applied across the thickness, electrostatic forces arise leading to a thickness reduction of the elastomer. The incompressible or nearly incompressible nature of most elastomers results in an area increase, and as a result the capacitance will change. Figure 1 shows a sketch of the actuation principle. This type of actuation, where the deformation is caused by the Coulomb forces between the electrodes, is usually termed the Maxwell effect and differentiates DEAs from other EAPs in so far that the polymer itself does not contain any large electrostrictive property. Typically for films of a thickness between 10 and
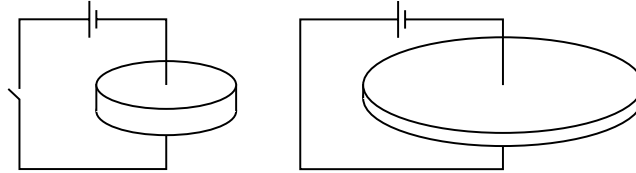

Figure 1: Principle of actuation, before actuation (left) and after actuation (right).

100 µm, a potential of $0.5 - 10$ kilovolts is required, but during operation the setup will consume only low amounts of electric power due to the electrostatic nature of the elastomer, see Rasmussen (2012). In order to reduce the operating voltages and at the same time increase the mechanical stiffness, the elastomers are often pre-stretched before they are electrically loaded. Applications include loudspeakers, optical apertures, motors and various generators, see for instance Pelrine et al. (2001a) and Pelrine et al. (2001b).

In comparisons between different possible DEA materials, VHB 4910 from 3M often stands out at as one of the more potential candidates, see Kornbluh et al. (2000); Pelrine et al. (2001b); O'Halloran et al. (2008) and Rasmussen (2012). VHB 4910 can be characterised as a non-linear viscoelastic rubbery acrylic material, capable of very large elastic strains and electrically actuated strains over 200%, see Pelrine

et al. (2000b) and Kofod et al. (2003). Numerous experimental investigations have been performed on VHB 4910. In Tagarielli et al. (2012); Hossain et al. (2012) and Hossain et al. (2015) the mechanical and electromechanical characteristics are investigated in terms of stress-strain curves from loading and unloading experiments at different strain rates as well as relaxation tests. The viscous behaviour is evident and demonstrates a non-linear rate dependent behaviour of the material with relatively long relaxation times. Mechanical, dielectric and conductive dissipation are indicated in the literature to be present, see for instance Zhao et al. (2011) and Chiang Foo et al. (2012). However, under normal conditions (room temperature and pressure) the dielectric response time is orders of magnitude smaller than the mechanical, and the conductive response time in orders of hours. In this work we focus on the mechanical dissipation effects only.

The electrical and electromechanical characterisation of VHB 4910 related to the dielectric permittivity and how this is influenced by temperature, frequency, type of electrode and pre-stretch is provided in, among others, Wissler and Mazza (2007a); McKay et al. (2009); Jean-Mistral et al. (2010); Li et al. (2011); Di Lillo et al. (2012); Vu-Cong et al. (2012, 2014) and Qiang et al. (2012). The results are, unfortunately, ambiguous and the permittivity and its dependencies remain a debated issue. Nevertheless, almost all of the above mentioned studies show an, even if sometimes small, decrease in permittivity with increased pre-stretch and a value of approximately 4.0-5.25 in an unstretched state and at room temperature. According to Qiang et al. (2012), the most influential parameter to the relative permittivity of the above mentioned factors is the pre-stretch value. Other electromechanical studies, Liu et al. (2014); Zhang et al. (2014) and Sahu et al. (2015), investigate the viscoelastic response under dynamic electrical loading and discover, among other things, that larger pre-stretch, for the same nominal electric field, results in lower amplitude of displacements and that, in the case of cyclic loading, both creep and stress relaxation depend on the number of loading cycles.

Dielectric elastomers are made up of long macromolecules, linked together through chemical crosslinks to form a three-dimensional network, able to sustain large elastic deformations. When modelling DEs, two main approaches can be distinguished; the phenomenological and the micro-mechanical ones. Examples of visco-electroelastic, phenomenologically based, continuum models of dielectric elastomers are included in Ask et al. (2012a,b); Khan et al. (2013); Büschel et al. (2013); Vogel et al. (2014) and Ask et al. (2015). In this work, a micro-mechanical framework established in Thylander et al. (2012, 2013) is used to incorporate statistical mechanics arguments on idealised chain molecules and to then link these to the macroscopic level by means of the micro-sphere formulation. The micro-sphere formulation allows for one-dimensional micromechanically motivated constitutive equations to be established and then transformed into three-dimensional counterparts via a direction average procedure over a micro-sphere. The micro-sphere theory, originally termed micro-plane theory and proposed for modelling of concrete structures, see Bažant and Oh (1983) and Carol et al. (2004), has proven useful in simulations of both rubber-like materials and biological tissue, see for instance Miehe et al. (2004); Miehe and Göktepe (2005); Menzel and Waffenschmidt (2009) and Linder et al. (2011), as well as of magneto- and electro-

3

elastically coupled materials, see Ethiraj et al. (2013) and Zäh and Miehe (2015). The novel contributions of the present electromechanically coupled micro-sphere model – as compared to Thylander et al. (2012, 2013) and other models established for dielectric elastomers – are (i) the introduction of a non-affine electromechanical kinematic quantity in combination with statistical-physics-motivated energy forms, (ii) the incorporation of viscous effects within the electromechanical micro-sphere model, and (iii) the finite-element-based identification of the underlying material parameters for experimental data for VHB 4910.

2   Balance relations

In this section we summarise the balance relations that govern a general electromechanically coupled problem. Electro-magnetic coupling is not considered and, moreover, the balance relations are restricted to the electrostatic case. Only local forms of the balance relations are presented and related boundary conditions are not explicitly mentioned. For detailed background information the reader is referred to Jackson (1962); Eringen (1989); Kovetz (2000); Dorfmann and Ogden (2005) and Saxena et al. (2014).

2.1   Basic kinematics

Positions of material particles of the body B are characterised by the vector $\boldsymbol{X}$ in a reference configuration $\mathcal{B}_0$. The motion of the body is described by the mapping $\boldsymbol{\varphi}$ which transforms the positions of material particles to the current configuration $\mathcal{B}_t$ by $\boldsymbol{x} = \boldsymbol{\varphi}(\boldsymbol{X}, t)$, whereby t represents time. The related so-called deformation gradient tensor $\boldsymbol{F}$ is defined as

$$
\begin{aligned}
\boldsymbol{F} &= \nabla_{\boldsymbol{X}} \, \boldsymbol{\varphi} \quad \text{with} \quad J = \det(\boldsymbol{F}) > 0 \quad \text{and} \\
\operatorname{cof}(\boldsymbol{F}) &= \partial_{\boldsymbol{F}} J = J \, \boldsymbol{F}^{-\mathrm{t}} \,.
\end{aligned}
\tag{1}
$$

Due to the nearly incompressible nature of polymers, the deformation gradient is assumed to be multiplicatively split into a volumetric and an isochoric part, i.e.

$$
\boldsymbol{F} = J^{1/3} \, \bar{\boldsymbol{F}} \quad \text{so that} \quad \det(\bar{\boldsymbol{F}}) = 1 \,.
\tag{2}
$$

Based on this split of the deformation gradient, two different right Cauchy-Green tensors are introduced,

$$
\boldsymbol{C} = \boldsymbol{F}^{\mathrm{t}} \cdot \boldsymbol{F} \quad \text{and} \quad \bar{\boldsymbol{C}} = \bar{\boldsymbol{F}}^{\mathrm{t}} \cdot \bar{\boldsymbol{F}} \,,
\tag{3}
$$

where $\det(\bar{\boldsymbol{C}}) = 1$ follows from eq. (2).

2.2   Gauß's law

We consider the specialisation of Maxwell's equations in the absence of magnetic fields, free electric charges and any time dependencies. Then, the spatial, i.e. in $\mathcal{B}_t$, vectorial fields of the electric displacements, $\boldsymbol{d}$, and the electric field, $\boldsymbol{e}$, satisfy

$$
\nabla_{\boldsymbol{x}} \cdot \boldsymbol{d} = 0 \quad \text{and} \quad \nabla_{\boldsymbol{x}}^{\mathrm{t}} \times \boldsymbol{e} = \boldsymbol{0} \,.
\tag{4}
$$

The divergence-free field of electric displacements, however, represents a local form of balance relation, namely Gauß's law. The spatial and material electric displacements are connected by the Piola transformation

$$\boldsymbol{D} = \boldsymbol{d} \cdot \mathrm{cof}(\boldsymbol{F}) \,. \tag{5}$$

In addition, the spatial electric field is related to its material counterpart according to

$$\boldsymbol{E} = \boldsymbol{e} \cdot \boldsymbol{F} \,. \tag{6}$$

The related referential representations in $\mathcal{B}_0$ read

$$\nabla_{\boldsymbol{X}} \cdot \boldsymbol{D} = 0 \quad \text{and} \quad \nabla_{\boldsymbol{X}}^{\mathrm{t}} \times \boldsymbol{E} = \boldsymbol{0} \,. \tag{7}$$

Since the electric field is curl-free it can be defined as the gradient of a scalar-valued field, here denoted as the electric potential $\phi(\boldsymbol{X}, t)$, such that

$$\boldsymbol{e} = -\nabla_{\boldsymbol{x}} \phi \quad \text{and} \quad \boldsymbol{E} = -\nabla_{\boldsymbol{X}} \phi \,. \tag{8}$$

The spatial electric displacements and the spatial electric field are connected by the general constitutive relation

$$\boldsymbol{d} = \varepsilon_0 \, \boldsymbol{e} + \boldsymbol{\pi} \,, \tag{9}$$

wherein ε_0 is the vacuum electric permittivity and $\boldsymbol{\pi}$ is the polarisation, which vanishes outside the body B. The referential counterpart in $\mathcal{B}_0$ is given by the Piola transformation in eq. (5), i.e.

$$\boldsymbol{D} = J \, \varepsilon_0 \, \boldsymbol{E} \cdot \boldsymbol{C}^{-1} + \boldsymbol{\Pi} \,, \tag{10}$$

with $\boldsymbol{\Pi} = \boldsymbol{\pi} \cdot \mathrm{cof}(\boldsymbol{F})$.

2.3   Balance of linear momentum

The electric field and its interaction with matter introduces additional body forces. As this work proceeds, the framework of the so-called two dipole model is adopted, so that the additional body force takes the representation $\boldsymbol{f}^{\mathrm{e}} = \nabla_{\boldsymbol{x}} \boldsymbol{e} \cdot \boldsymbol{\pi} = \nabla_{\boldsymbol{x}} \cdot \left[\boldsymbol{e} \otimes \boldsymbol{d} - \frac{1}{2} \left[\boldsymbol{e} \cdot \boldsymbol{e} \right] \boldsymbol{I} \right]$, with $\boldsymbol{I}$ being the second order identity tensor. The local, quasi-static form of balance of linear momentum (for a closed system where mass is conserved) in fully spatial representation in $\mathcal{B}_t$ then reads

$$\nabla_{\boldsymbol{x}} \cdot \boldsymbol{\sigma} + \boldsymbol{f}^{\mathrm{e}} + \rho \, \boldsymbol{f} = \boldsymbol{0} \,, \tag{11}$$

where $\boldsymbol{f}$ represents the mechanical body forces and ρ the current mass density. In general, the presence of the electric field and its interaction with matter renders the Cauchy stress $\boldsymbol{\sigma}$ to be unsymmetric. By shifting the electric body forces to the mechanical flux term a symmetric total stress tensor

$$\boldsymbol{\tau} = \boldsymbol{\sigma} + \boldsymbol{e} \otimes \boldsymbol{d} - \tfrac{1}{2} \varepsilon_0 \left[\boldsymbol{e} \cdot \boldsymbol{e} \right] \boldsymbol{I} \,, \tag{12}$$

can be introduced such that eq. (11) corresponds to

$$\nabla_{\boldsymbol{x}} \cdot \boldsymbol{\tau} + \rho \, \boldsymbol{f} = \boldsymbol{0} \,. \tag{13}$$

The referential counterpart of eq. (13) reads

$$\nabla_{\boldsymbol{X}} \cdot \boldsymbol{T} + \rho_0 \, \boldsymbol{f} = \boldsymbol{0} \,, \tag{14}$$

where $\boldsymbol{T} = \boldsymbol{\tau} \cdot \mathrm{cof}(\boldsymbol{F})$ and $\rho_0 = J \, \rho$.

2.4 First and second law of thermodynamics

The local form of the first and second law of thermodynamics in the case of electrostatics and in terms of spatial arguments reads

$$\rho \, \dot{\epsilon} = \Big[\boldsymbol{\sigma} + [\, \boldsymbol{e} \cdot \boldsymbol{\pi} \,] \, \boldsymbol{I} \Big] : \boldsymbol{l} + \boldsymbol{e} \cdot \dot{\boldsymbol{\pi}} - \nabla_{\boldsymbol{x}} \cdot \boldsymbol{q} + \rho \, h$$
$$\rho \, \dot{\eta} \geq \rho \, h / \theta - \nabla_{\boldsymbol{x}} \cdot [\, \boldsymbol{q} / \theta \,] \,, \tag{15}$$

together with boundary conditions and the entropy source and flux terms directly related to the heat source and flux. Notation $\dot{\bullet}$ refers to the material time derivative so that $\dot{\epsilon}$ is the rate of change of internal energy per unit mass and $\boldsymbol{l} = \nabla_{\boldsymbol{x}} \dot{\boldsymbol{\varphi}}$ corresponds to the spatial velocity gradient. Moreover, $\boldsymbol{q}$ represents the spatial heat flux, θ denotes the absolute temperature, h characterises a heat source per unit mass and η is the specific entropy. When referred to referential volume and area elements, these relations read

$$\rho_0 \, \dot{\epsilon} = \Big[\boldsymbol{P} + [\, \boldsymbol{F}^{-\mathrm{t}} \cdot \boldsymbol{E} \,] \otimes \boldsymbol{\Pi} \Big] : \dot{\boldsymbol{F}} + \boldsymbol{E} \cdot \dot{\boldsymbol{\Pi}} - \nabla_{\boldsymbol{X}} \cdot \boldsymbol{Q} + \rho_0 \, h$$
$$\rho_0 \, \dot{\eta} \geq \rho_0 \, h / \theta - \nabla_{\boldsymbol{X}} \cdot [\, \boldsymbol{Q} / \theta \,] \,, \tag{16}$$

wherein the relation $\dot{\boldsymbol{F}} = \nabla_{\boldsymbol{X}} \dot{\boldsymbol{\varphi}} = \boldsymbol{l} \cdot \boldsymbol{F}$ is used, and $\boldsymbol{P} = \boldsymbol{\sigma} \cdot \mathrm{cof}(\boldsymbol{F})$ as well as $\boldsymbol{Q} = \boldsymbol{q} \cdot \mathrm{cof}(\boldsymbol{F})$ are introduced as Piola stresses and referential heat flux vector, respectively.

3 Constitutive relations

The constitutive framework established in Thylander et al. (2012, 2013) is here extended to include viscoelastic contributions and altered in the sense that the elastic parts of the free energy are micromechanically motivated. All constitutive equations are derived in a thermodynamically consistent manner.

3.1 Dissipation inequality

Introducing the Helmholtz free energy $\psi = \epsilon - \theta \, \eta$ and combining eq. $(15)_a$ and $(15)_b$ as well as eq. $(16)_a$ and $(16)_b$, respectively, we obtain the dissipation inequality in spatial and material configuration for the isothermal case

$$-\rho \, \dot{\psi} + [\boldsymbol{\sigma} + [\boldsymbol{e} \cdot \boldsymbol{\pi}] \, \boldsymbol{I}] : \boldsymbol{l} + \boldsymbol{e} \cdot \dot{\boldsymbol{\pi}} \geq 0$$
$$-\rho_0 \, \dot{\psi} + \Big[\boldsymbol{P} + \big[\boldsymbol{F}^{-\mathrm{t}} \cdot \boldsymbol{E} \big] \otimes \boldsymbol{\Pi} \Big] : \dot{\boldsymbol{F}} + \boldsymbol{E} \cdot \dot{\boldsymbol{\Pi}} \geq 0 \,. \tag{17}$$

6

Next, we introduce the Legendre transformation $\Psi = \psi - \frac{1}{\rho_0}\boldsymbol{\Pi} \cdot \boldsymbol{E}$ where $\psi(\boldsymbol{F}, \boldsymbol{\Pi}, \boldsymbol{K})$ and $\Psi(\boldsymbol{F}, \boldsymbol{E}, \boldsymbol{K})$ are free energy functions, and where $\boldsymbol{K}$ are internal variables that govern the time-dependent behaviour. The dissipation inequality in material quantities then reads

$$-\rho_0\,\dot{\Psi} + \left[\boldsymbol{P} + \left[\boldsymbol{F}^{-\mathrm{t}} \cdot \boldsymbol{E}\right] \otimes \boldsymbol{\Pi}\right] : \dot{\boldsymbol{F}} - \boldsymbol{\Pi} \cdot \dot{\boldsymbol{E}} \geq 0\,. \tag{18}$$

Moreover, an augmented free energy $\Omega(\boldsymbol{F}, \boldsymbol{E}, \boldsymbol{K})$ is introduced, as proposed in Dorfmann and Ogden (2005), defined as

$$\Omega = \rho_0\,\Psi - \frac{1}{2}\varepsilon_0\,J\,\boldsymbol{C}^{-1} : [\boldsymbol{E} \otimes \boldsymbol{E}]\,. \tag{19}$$

With eq. (18) and (19) the dissipation inequality then reads as

$$\left[-\boldsymbol{T} + \frac{\partial\Omega}{\partial\boldsymbol{F}}\right] : \dot{\boldsymbol{F}} + \left[-\boldsymbol{D} - \frac{\partial\Omega}{\partial\boldsymbol{E}}\right] \cdot \dot{\boldsymbol{E}} - \frac{\partial\Omega}{\partial\boldsymbol{K}} \cdot \dot{\boldsymbol{K}} \geq 0\,. \tag{20}$$

Assuming the following relations for the total stress tensor $\boldsymbol{T}$, the dielectric displacements $\boldsymbol{D}$ and the evolution laws for the internal variables $\boldsymbol{K}$

$$\boldsymbol{T} = \frac{\partial\Omega}{\partial\boldsymbol{F}}\,, \quad \boldsymbol{D} = -\frac{\partial\Omega}{\partial\boldsymbol{E}} \quad \text{and} \quad \mathcal{D}_{red,mac} = -\frac{\partial\Omega}{\partial\boldsymbol{K}} \cdot \dot{\boldsymbol{K}} \geq 0\,, \tag{21}$$

ensures the dissipation inequality to be unconditionally fulfilled. The reduced macroscopic dissipation $\mathcal{D}_{red,mac} \geq 0$ is fulfilled by considering the solution of the initial-value problem

$$\frac{\partial\Omega}{\partial\boldsymbol{K}} + \frac{\partial\Xi(\dot{\boldsymbol{K}})}{\partial\dot{\boldsymbol{K}}} = \boldsymbol{0} \quad \text{with} \quad \boldsymbol{K}\,|_{t=0} = \boldsymbol{K}_0\,, \tag{22}$$

where Ξ is a macroscopic dissipation function with $\Xi(\boldsymbol{0}) = 0$. Assuming Ξ to be convex ensures the dissipation $\mathcal{D}_{red,mac}$ to be non-negative.

3.2 Amended free energy

Throughout this work we assume a quasi-static electric field and quasi-static but rate-dependent mechanical response. Furthermore, it is assumed that only the deformation, and not the electric field, governs the viscous behaviour so that there is no direct coupling between the electric field and the viscous deformation. The macroscopic amended free energy Ω, see Dorfmann and Ogden (2005), is defined in terms of the deformation gradient $\boldsymbol{F}$, the referential electric field $\boldsymbol{E}$ and internal variables $\boldsymbol{K}$, see eq. (19). An additive split of the free energy into volumetric and isochoric parts is adopted as is common in cases of nearly incompressible materials, where the volumetric part describes the energy associated with changes in volume and where the isochoric part describes the energy associated solely to volume-preserving deformations. The isochoric part is then further additively split into three main parts; elastic (e_∞), viscoelastic (e_v) and electroelastic (e_{el}), i.e.

$$\begin{aligned}
\Omega(\boldsymbol{F}, \boldsymbol{E}, \boldsymbol{K}) = {}& \Omega^{vol}(J) + \Omega^{e_\infty}(\bar{\boldsymbol{C}}) + \Omega^{e_v}(\bar{\boldsymbol{C}}, \boldsymbol{K}) \\
& + \Omega^{e_{el}}(\bar{\boldsymbol{C}}, \boldsymbol{E}) - \frac{1}{2}\varepsilon_0\,J\,\boldsymbol{C}^{-1} : [\boldsymbol{E} \otimes \boldsymbol{E}]\,.
\end{aligned} \tag{23}$$

7

The flux terms and related elasticity-type tensors resume the same additive structure. Due to the micromechanical approach chosen in this paper, the specific formats of the free energy associated with the isochoric deformation $\bar{C}$ are determined only in terms of microscopic independent variables, and therefore specified first in the following section. The volumetric part Ω^{vol} is taken in penalty form as

$$\Omega^{vol} = \frac{1}{2}\,\kappa\left[J-1\right]^2 , \tag{24}$$

where κ is the bulk modulus.

3.3 Evaluation of flux terms

For the mechanical flux term we consider the total, Piola type, stress tensor $\boldsymbol{T}$ and for the electrical flux term the electric displacements $\boldsymbol{D}$. These are evaluated in terms of the partial derivatives of the free energy function according to eq. (21) so that

$$
\begin{aligned}
\boldsymbol{T} = &\frac{1}{2}\,J\,\partial_J\Omega^{vol}\boldsymbol{C}^{-1} : \frac{\partial \boldsymbol{C}}{\partial \boldsymbol{F}} \\
&+ J^{-2/3}\,\partial_{\bar{C}}\left[\Omega^{e\infty} + \Omega^{ev} + \Omega^{eel}\right] : \mathbf{P} : \frac{\partial \boldsymbol{C}}{\partial \boldsymbol{F}} \\
&+ \varepsilon_0\,J\,\frac{1}{2}\bigg[\left[\boldsymbol{C}^{-1}\cdot\boldsymbol{E}\right]\otimes\left[\boldsymbol{E}\cdot\boldsymbol{C}^{-1}\right] \\
&- \frac{1}{2}\left[\boldsymbol{E}\cdot\boldsymbol{C}^{-1}\cdot\boldsymbol{E}\right]\boldsymbol{C}^{-1}\bigg] : \frac{\partial \boldsymbol{C}}{\partial \boldsymbol{F}}
\end{aligned}
\tag{25}
$$

and

$$\boldsymbol{D} = -\,\partial_{\bar{E}}\Omega^{eel} - \varepsilon_0\,J\,\boldsymbol{C}^{-1}\cdot\boldsymbol{E} , \tag{26}$$

where $\mathbf{P} = \mathbf{I} - \frac{1}{3}\,\boldsymbol{C}^{-1}\otimes\boldsymbol{C}$ and $\mathbf{I}$ denotes the fourth-order identity tensor.

4 Microsphere formulation

Elastomers or rubber-like materials basically consist of long-chain molecules connected at junction points, through chemical crosslinks, embedded into a 3-dimensional network. When modelling this type of material micromechanically motivated constitutive models are made possible through to the use of statistical mechanics. By constructing a description of each chain in the network and then introducing a suitable averaging procedure, it is possible to obtain a macroscopic constitutive equation for the continuum.

In the context of statistical mechanics, a polymer chain is idealised to consist of N, so-called Kuhn segments, of equal length l so that the total contour length L of a chain is $L = N\,l$. For an unstrained chain the end-to-end vector $\boldsymbol{r}$, between adjacent junction points, assumes the value $\|\boldsymbol{r}_0\| = r_0 = \sqrt{N}\,l$, see Treloar (1975).
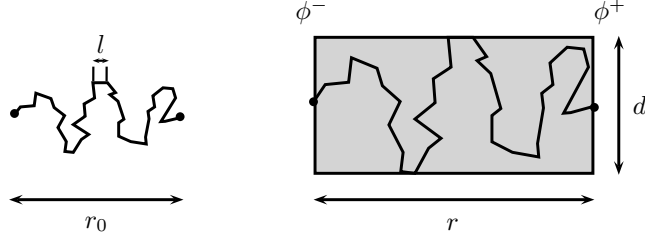
Figure 2: Sketch of idealised polymer chain (left) and microscopic quantities (right).

In this work we make use of the length stretch λ_f and the area stretch λ_c to describe the deformation of a single chain defined as

$$\lambda_f = \frac{r}{r_0} \quad \text{and} \quad \lambda_c = \left[\frac{d_0}{d} \right]^2 , \tag{27}$$

where d_0 and d are the reference and the current diameter of an imagined tube surrounding the individual chain and hence constraining the number of possible conformations. The elastic deformation on the microscopic level is governed by two separate free energies where the length stretch is linked to the energy by classical inverse Langevin statistics, and where the area stretch is linked by considering a constrained free energy for the tube part as suggested in Doi and Edwards (1986). The time dependent viscous deformation assumes a similar split into two different free energies defined in terms of the length and area stretch respectively. The elastic and viscoelastic free energies and the link between the kinematic variables on macro- and microscopic level in this work will only be summarised here. For more details see Miehe et al. (2004); Miehe and Göktepe (2005). In terms of the electric field, a scalar-valued quantity E is introduced as

$$E = -\frac{\Delta\phi}{r_0} , \tag{28}$$

so that the coupled free energy of the continuum is linked to the microscopic quantities E and λ_c. For a schematic figure of the idealised chain and the microscopical quantities introduced, see figure 2.

The macroscopic free energy Θ per unit volume of the polymer network, assumed to be initially homogeneous and isotropic on the macroscopic continuum level, corresponds to the sum of the n chain's individual energy θ_n

$$\Theta = \sum_n \theta_n . \tag{29}$$

By assuming an isotropic response of the network it is possible to replace the discrete sum in eq. (29) by a continuous average of the microscopic free energies over the surface of a micro-sphere such that

$$\Theta = n \langle \theta \rangle , \tag{30}$$

where $\langle v \rangle = \frac{1}{4\pi} \int_{\mathbb{U}^2} v(A) \, \mathrm{d}A$ can be interpreted as a direction average of v on a unit micro-sphere $\mathbb{U}^2$. In general, such integrations cannot be performed analytically, and

9

are therefore approximated with a numerical integration scheme

$$\frac{1}{4\pi} \int_{\mathbb{U}^2} v \, \mathrm{d}A \approx \sum_{i=1}^{\mathrm{nid}} v_i \, \omega_i \,, \tag{31}$$

wherein v is a scalar quantity, index i refers to an integration direction $\boldsymbol{n}_i \in \mathbb{U}^2$, with $\|\boldsymbol{n}_i\| = 1$, so that v_i is the value of v in the direction of $\boldsymbol{n}_i$ and ω_i represent integration weights. The integration directions and weights are subjected to the following constraints

$$\sum_{i=1}^{\mathrm{nid}} \omega_i = 1 \,, \quad \sum_{i=1}^{\mathrm{nid}} \boldsymbol{n}_i \, \omega_i = \boldsymbol{0} \quad \text{and} \quad \sum_{i=1}^{\mathrm{nid}} \boldsymbol{n}_i \otimes \boldsymbol{n}_i \, \omega_i = \frac{1}{3} \boldsymbol{I} \,, \tag{32}$$

so that any weighted summation over odd-order moments in $\boldsymbol{n}_i$ vanishes, whereas summations over even-order moments result in identity-type tensors. In this work, a number of 21 integration directions for the hemisphere is assumed to be efficient, so that nid $= 42$. For different integration schemes and different number of integration directions see for example Bažant and Oh (1986); Waffenschmidt et al. (2012) and Ostwald et al. (2015).

The macroscopic counterparts to eq. (27) and 28 are introduced as projections of the isochoric deformation gradient, $\bar{\boldsymbol{F}}$, and its cofactor, $\mathrm{cof}(\bar{\boldsymbol{F}})$, as well as the material electric field, $\boldsymbol{E}$, onto the directions of the unitsphere

$$\lambda_{f_i} = \|\bar{\boldsymbol{F}} \cdot \boldsymbol{n}_i\| = \sqrt{\boldsymbol{n}_i \cdot \bar{\boldsymbol{C}} \cdot \boldsymbol{n}_i} \quad \text{and} \quad \lambda_{c_i} = \|\bar{\boldsymbol{F}}^{-\mathrm{t}} \cdot \boldsymbol{n}_i\| = \sqrt{\boldsymbol{n}_i \cdot \bar{\boldsymbol{C}}^{-1} \cdot \boldsymbol{n}_i} \tag{33}$$

and

$$E_i = \boldsymbol{E} \cdot \boldsymbol{n}_i \,. \tag{34}$$

Finally, by affine and/or non-affine kinematic assumptions that relate the length and area stretch and the scalar electric field to the macroscopic deformation via the free energies, it is possible to capture the overall continuum response. In view of eq. (30) an affine model averages over the individual chain energies, while averaging over the independent variables gives a non-affine approximation, cf. Miehe et al. (2004). Hence, the following two scenarios are considered

$$\Theta = n \left\langle \theta(x) \right\rangle \qquad \text{or} \qquad \Theta = n \, \theta(\langle x \rangle) \,, \tag{35}$$

where x represent some scalar microscopic independent variables.

4.1 Dissipation inequality

A reduced microscopic dissipation $\mathcal{D}_{red,mic}$ is introduced and related to the macroscopic counterpart $\mathcal{D}_{red,mac}$ in terms of the direction average introduced with the microsphere formulation so that

$$\mathcal{D}_{red,mac} = \left\langle \mathcal{D}_{red,mic} \right\rangle \geq 0 \,. \tag{36}$$

A number of $2\,s$, where s depends on the number of viscous elements needed, kinematic internal variables $\boldsymbol{\varepsilon}_f = [\varepsilon_f^1, \varepsilon_f^2, ..., \varepsilon_f^s]$ and $\boldsymbol{\varepsilon}_c = [\varepsilon_c^1, \varepsilon_c^2, ..., \varepsilon_c^s]$ are introduced on the microscopic level so that

$$\mathcal{D}_{red,mic} = -\frac{\partial \Omega}{\partial \boldsymbol{\varepsilon}_y} \cdot \dot{\boldsymbol{\varepsilon}}_y = \boldsymbol{\beta}_y \cdot \dot{\boldsymbol{\varepsilon}}_y \geq 0 \,, \tag{37}$$

where $y = f, c$. In analogy with eq. (22), a non-negative microscopic dissipation at the microscopic level is fulfilled by considering the solution to the initial value problem

$$\frac{\partial \Omega}{\partial \boldsymbol{\varepsilon}_y} + \frac{\partial \varkappa_y}{\partial \dot{\boldsymbol{\varepsilon}}_y} = \mathbf{0} \quad \text{with} \quad \boldsymbol{\varepsilon}_y \big|_{t=0} = \mathbf{0} \,, \tag{38}$$

where $\varkappa_y$ are microscopic dissipation functions.

4.2 Amended free energy

The amended free energy in terms of microscopic independent variables are split into the same five main parts as in eq. (23). Only the parts of the free energy connected to the isochoric deformation will be evaluated in terms of the microsphere framework. In addition, we assume ε_0 to give a negligible contribution compared to the remaining contributions so that the free space part is neglected. The elastic equilibrium part $\Omega^{e\infty}$ is split into two parts, one connected to the length stretch λ_f and one to the area stretch λ_c as follows

$$\Omega^{e\infty,f}(\lambda_f) = N\,k\,T \left[\lambda_{fr}\,\mathcal{L}^{-1}(\lambda_{fr}) + \ln\left(\frac{\mathcal{L}^{-1}(\lambda_{fr})}{\sinh\left(\mathcal{L}^{-1}(\lambda_{fr})\right)} \right) \right] \,, \tag{39}$$
$$\Omega^{e\infty,c}(\lambda_c) = N\,k\,T\,U\,\lambda_c \,,$$

where $U = \alpha \left[\frac{l}{d_0} \right]^2$ and $\lambda_{fr} = \frac{\lambda_f}{\sqrt{N}}$, N is the number of chain segments, k the Boltzmann constant, T the absolute temperature, $\mathcal{L}(x) = \coth(x) - 1$ the Langevin function and α a cross-section factor. The transformation between the macroscopic and microscopic level for the elastic equilibrium parts is accomplished in the following manner

$$\Omega^{e\infty,f}(\bar{\boldsymbol{C}}) = n\,\Omega^{e\infty,f}(\langle \lambda_{f_i} \rangle_p) \,, \tag{40}$$
$$\Omega^{e\infty,c}(\bar{\boldsymbol{C}}) = n\,\langle \Omega^{e\infty,c}(\lambda_{c_i}^q) \rangle \,,$$

where $\langle v \rangle_p = \sqrt[p]{\langle v^p \rangle}$ is the p-root average of the scalar variable v and p and q are material parameters, see Miehe et al. (2004).

Furthermore, the microscopic viscous free energies are defined in terms of the length and area stretches as well as the internal variables $\boldsymbol{\varepsilon}_f$ and $\boldsymbol{\varepsilon}_c$. Note that there is no actual macroscopic format of $\boldsymbol{\varepsilon}_f$ and $\boldsymbol{\varepsilon}_c$; they are merely denoted by $\boldsymbol{K}$. In terms of the kinematic internal variables the viscous free energies are defined as

$$\Omega^{ev,y}(\lambda_y, \boldsymbol{\varepsilon}_y) = \frac{1}{2} \sum_{a=1}^{s} \mu_y^a \left[\ln(\lambda_y) - \varepsilon_y^a \right]^2 \,, \tag{41}$$

11

where $y = f, c$ and μ_y^a are material parameters, see Miehe and Göktepe (2005). The transformation between the macroscopic and microscopic level is performed in an affine manner, i.e. $\lambda_y = \lambda_{y,i}$ and $\boldsymbol{K} = \boldsymbol{\varepsilon}_y$, such that

$$\Omega^{ev,y}(\bar{\boldsymbol{C}}, \boldsymbol{K}) = n \left\langle \, \Omega^{ev,y} \left(\lambda_{y_i}, \boldsymbol{\varepsilon}_y \right) \, \right\rangle . \tag{42}$$

Specifications of the dissipation function $\varkappa_y$ and the evolution of the internal variables $\boldsymbol{\varepsilon}_y$ are summarised in appendix A. For the coupled electromechanical behaviour on the microscopic level the following simple combination of E and λ_c is used

$$\Omega^{e_{el}}(\Lambda) = c_1 \, \Lambda^m \quad \text{with} \quad \Lambda = c_2^{-2} \lambda_f^b \, E^2 \, , \tag{43}$$

where the parameter c_2 is introduced to normalise the unit of E.

4.3   Evaluation of flux terms

The flux terms $\boldsymbol{T}$ and $\boldsymbol{D}$ are evaluated in terms of the microsphere formulation as

$$\boldsymbol{T} = \frac{\partial \, n \left\langle \Omega \right\rangle}{\partial \boldsymbol{C}} : \frac{\partial \boldsymbol{C}}{\partial \boldsymbol{F}} \quad \text{and} \quad \boldsymbol{D} = - \frac{\partial \, n \left\langle \Omega \right\rangle}{\partial \boldsymbol{E}} \, , \tag{44}$$

where, again, n is the number of chains in the network. Applying the specific affine/non-affine transformations previously stated we obtain for the stresses

$$\begin{aligned}
\partial_{\bar{\boldsymbol{C}}} \Omega^{e\infty} &= n \, \partial_{\bar{\boldsymbol{C}}} \left[\, \Omega^{e\infty,f} (\langle \lambda_{f_i} \rangle_p) + \langle \, \Omega^{e\infty,c} (\lambda_{c_i}^q) \, \rangle \, \right] , \\
\partial_{\bar{\boldsymbol{C}}} \Omega^{ev} &= n \, \partial_{\bar{\boldsymbol{C}}} \left[\, \langle \, \Omega^{ev,f} (\lambda_{f_i}, \boldsymbol{\varepsilon}_f) \, \rangle + \langle \, \Omega^{ev,c} (\lambda_{c_i}, \boldsymbol{\varepsilon}_c) \, \rangle \, \right] , \\
\partial_{\bar{\boldsymbol{C}}} \Omega^{e_{el}} &= n \, \partial_{\bar{\boldsymbol{C}}} \Omega^{e_{el}} (\langle \Lambda_i \rangle) ,
\end{aligned} \tag{45}$$

and for the electric displacements

$$\partial_{\boldsymbol{E}} \Omega^{e_{el}} = n \, \partial_{\boldsymbol{E}} \Omega^{e_{el}} (\langle \Lambda_i \rangle) . \tag{46}$$

The partial derivatives that appear in eq. (45) and (46) are specified in appendix B.

5   Calibration of constitutive equations

In order to show that the chosen format is able to reproduce the behaviour of a typical dielectric elastomer, we calibrate the model to the popular acrylic elastomer VHB 4910. The polymer is produced by 3M and is a transparent adhesive tape available for commercial use. The polymer is often promoted as a good candidate for use in dielectric elastomer actuators, often due to its high actuation strain and high energy density (mechanical output energy stroke per unit volume or mass of material), see Kornbluh et al. (2000); Pelrine et al. (2001b); O'Halloran et al. (2008) and Rasmussen (2012). It can be characterised as a very soft, nearly incompressible polymer with noticeably non-linear viscoelastic behaviour.

A direct simplex method in MATLAB is used to identify the material parameters. The goal function to minimise is taken as the relative error between the experimental

data set and the corresponding set of simulated data at discrete levels of strain or time. The calibration is divided into two main parts so that the mechanical and electromechanically coupled parameters are calibrated separately. The determination of the mechanical material parameters is split into two parts, one elastic part that determines the long term equilibrium response, and one viscoelastic part that governs the time-dependent behaviour.

5.1 Elastic and viscoelastic contributions

Experimental data for the elastic and viscoelastic behaviour of VHB 4910 is found in Hossain et al. (2012). The calibration of elastic and viscoelastic parameters is performed simultaneously by comparison with experimental data from one multi-step relaxation test, several single-step relaxation tests and four different loading and unloading curves, all points equally weighted in the calibration. As experimental data for strains under homogeneous deformation were available, no Finite Element (FE) simulation is performed but a homogeneous deformation assumed and the deformation gradient $\boldsymbol{F}$ prescribed as

$$\boldsymbol{F} = \lambda \, \boldsymbol{e}_x \otimes \boldsymbol{e}_x + \lambda^{-1/2} \left[\boldsymbol{I} - \boldsymbol{e}_x \otimes \boldsymbol{e}_x \right] , \tag{47}$$

together with an uniaxial stress state in the $\boldsymbol{e}_x$-direction.

5.1.1 Elastic contribution

Five different elastic equilibrium parameters are sought; μ_e, N, p, U and q, cf. eq. (52)-(53) and table 4. The mechanical nominal, Piola type, stress in the elongation direction, here denoted $P_{xx} = \boldsymbol{e}_x \cdot \boldsymbol{P} \cdot \boldsymbol{e}_x$, corresponding to twenty discrete values of strain were available from multi- and single-step tests. The volumetric pressure term is determined from the condition that $P_{yy} = P_{zz} = 0$. The undeformed sample dimensions were 50 mm x 5 mm x 1 mm in the x, y and z-direction respectively, and the deformation was applied at a deformation velocity of 10 mm s^{-1} which was then followed by a holding period of 30 minutes. The stress values asymptomatically reached after this holding time were regarded as the elastic equilibrium stress. The experimental data and fit to values produced by the constitutive model used in this article can be seen in figure 3(a). The elastic parameters sought are listed in table 1.

Table 1: Elastic material parameters.

$$
\begin{aligned}
\mu_e \ [\text{Pa}] &= 1.1000 \cdot 10^4 \\
N &= 1.0000 \cdot 10^3 \\
p &= 2.9793 \\
U &= 8.7979 \cdot 10^{-1} \\
q &= 7.0590 \cdot 10^{-4}
\end{aligned}
$$

Table 2: Viscoelastic material parameters.

$$
\begin{aligned}
\boldsymbol{\mu}_f \ [\text{Pa}] &= [\ 5.6456 \cdot 10^5 \quad 1.0478 \cdot 10^5 \quad 7.2672 \cdot 10^4 \quad 2.5046 \cdot 10^4\ ] \\
\boldsymbol{\mu}_c \ [\text{Pa}] &= [\ 1.0890 \cdot 10^5 \quad 2.2915 \cdot 10^4 \quad 7.4475 \cdot 10^4 \quad 7.7971 \cdot 10^3\ ] \\
\boldsymbol{\delta}_f &= [\ 7.7392 \cdot 10^{-1} \quad 4.8793 \cdot 10^{-1} \quad 1.9775 \qquad 4.5454 \qquad] \\
\boldsymbol{\delta}_c &= [\ 2.4470 \qquad 7.8005 \cdot 10^{-1} \quad 1.9550 \qquad 1.0631 \qquad] \\
\boldsymbol{\tau} \ [\text{s}] &= [\ 2.7824 \qquad 3.7432 \cdot 10^2 \quad 1.2635 \cdot 10^{-1} \quad 7.4125 \cdot 10^2\ ]
\end{aligned}
$$

(a) Elastic response

(b) Viscoelastic response
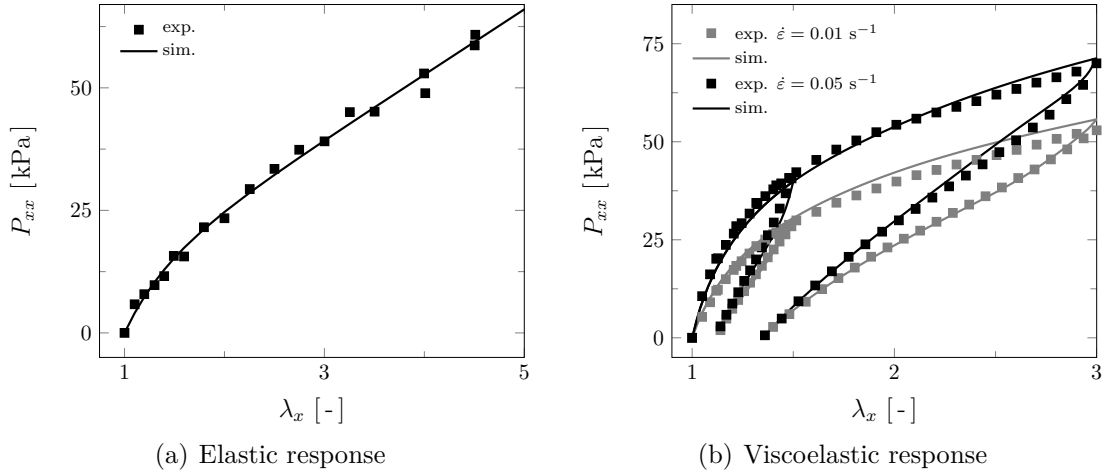
Figure 3: Elastic, (a), and viscoelastic, (b), experimental data, Hossain et al. (2012), and simulated fit.

5.1.2 Viscoelastic contribution

In order to find the viscous material parameters, four different loading-unloading curves are used. The highest and lowest strain rates together with largest and smallest maximum strain levels are chosen for the calibration. With a spectrum of relaxation times, several viscous elements need to be considered. For each viscous element introduced, five material parameters need to be identified, i.e. $\boldsymbol{\mu}_f = [\mu_f^1, \mu_f^2, ..., \mu_f^s]$, $\boldsymbol{\mu}_c = [\mu_c^1, \mu_c^2, ..., \mu_c^s]$, $\boldsymbol{\delta}_f = [\delta_f^1, \delta_f^2, ..., \delta_f^s]$, $\boldsymbol{\delta}_c = [\delta_c^1, \delta_c^2, ..., \delta_c^s]$ and $\boldsymbol{\tau}_f = \boldsymbol{\tau}_c = \boldsymbol{\tau} = [\tau^1, \tau^2, ..., \tau^s]$, see eq. (51), (54)-(55) and table 4. It is observed that a set of four viscous elements is sufficient to capture the viscoelastic behaviour with good accuracy, which corresponds to $s = 4$. The fit with the calibrated parameters for the selected loading-unloading curves can be seen in figure 3(b) and the material parameters are summarised in table 2.

5.2 Electro-viscoelastic contribution

Experimental data for the electro-viscoelastic behaviour of VHB 4910 is found in Wissler and Mazza (2007b). Experiments are performed on circular VHB 4910 membranes. The membranes are first biaxially prestrained to three different levels of

stretch ratios; $\lambda_{pre} = 3, 4$ and 5, so that they obtain an outer radius of 75 mm. At this stage the membranes are fixed in a frame, and an area of radius 7.5 mm in the center is coated with graphite powder and silicone oil on both sides of the membrane and connected to a voltage supply. Three different voltage levels are used for the calibration, namely 2000, 2500 and 3000 V. The inhomogeneous deformation that occurs at the border between the active and passive area of the membrane requires an FE simulation. An in-house built Fortran code was used for the FE simulation when calibrating the three remaining electroelastic material parameters; c_1, b and m, cf. eq. (56) and table 4. The parameter c_2, introduced to normalise the unit of the electric field E, is not calibrated but set to 1 V m^{-1}. The circular geometry of the membrane makes it possible for an axisymmetric 2D simulation. A sketch of the axisymmetric cross-section can be seen in figure 4(a) along with electrical boundary conditions in figure 4(b). Symmetry conditions also apply in the thickness direction and therefore only half of the electric potential is applied. Moreover, due to the nearly incompressible nature of the material, a four-field variational approach is implemented to prevent locking, for more details see Ask et al. (2013). The bulk modulus, κ, appearing in the volumetric free energy, is determined from the shear modulus μ_e and the Poisson's ratio which is set to 0.49.

(a)   (b)
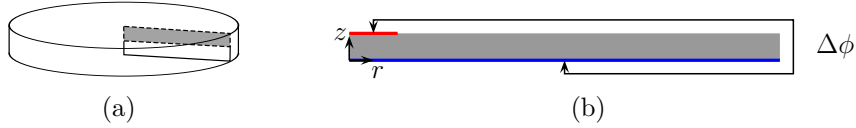
Figure 4: Sketch of axisymmetric model and boundary conditions.
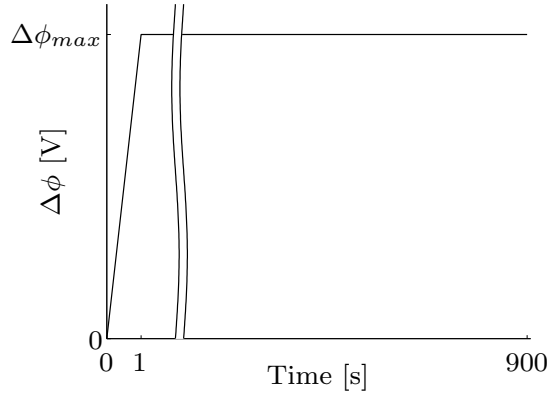
Figure 5: Load ramp function for simulation of the electro-viscoelastic response.

The simulation is divided into two steps, first the pre-stretch is applied for three meshes with initial dimensions 0.5×25, 0.5×18.75 and 0.5×15 mm^2 respectively, so that they all obtain the sought outer radius after pre-stretch. The same discretisations are used in all three cases with a 3×363 number of elements in the z- and r-direction respectively. This step is done elastically, i.e. no viscous effects are taken into account. Secondly, the electric loading is applied using the ramp function shown in figure 5 where $\Delta\phi_{max}$ varies between the three different voltage levels investigated. This
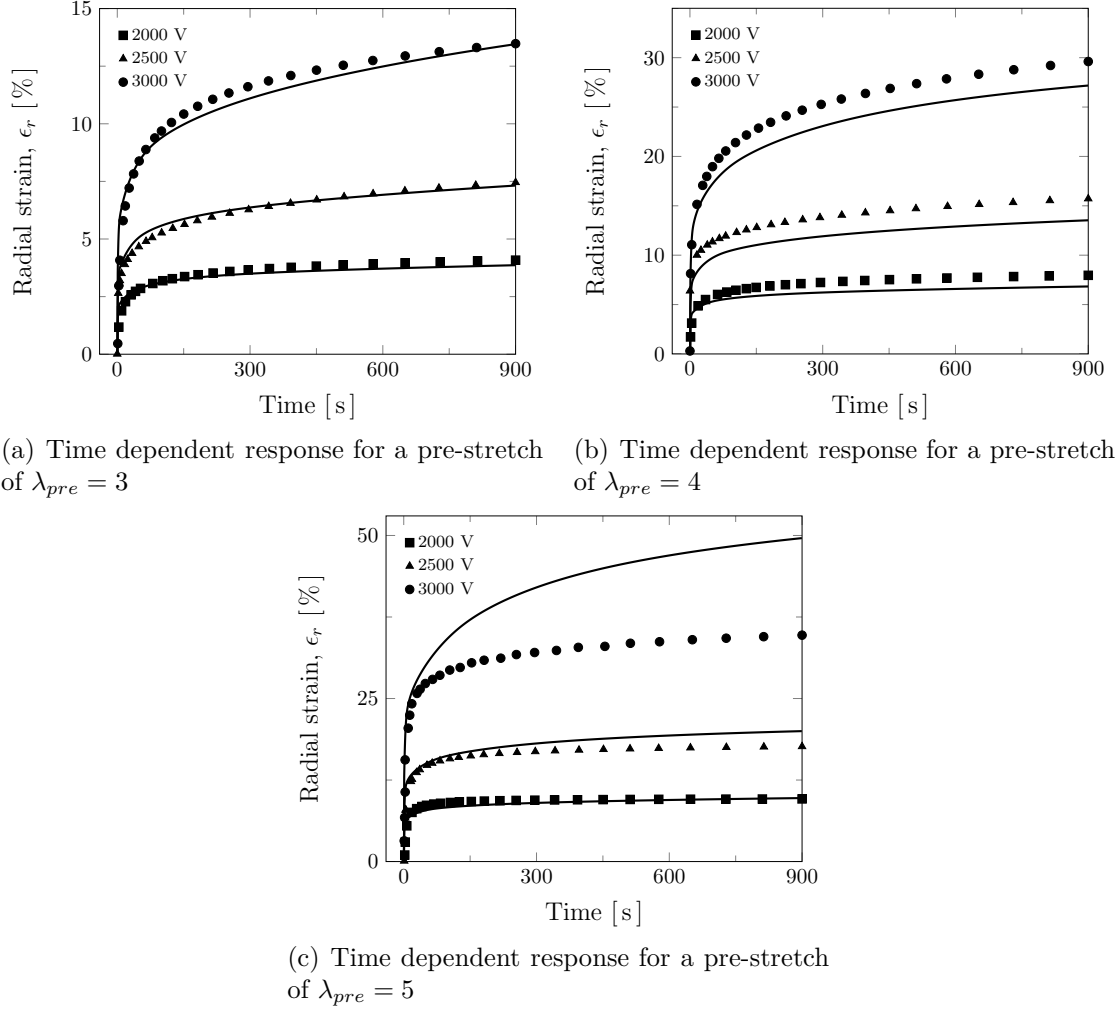
15

(a) Time dependent response for a pre-stretch of $\lambda_{pre} = 3$

(b) Time dependent response for a pre-stretch of $\lambda_{pre} = 4$

(c) Time dependent response for a pre-stretch of $\lambda_{pre} = 5$

Figure 6: Electro-viscoelastic response. Solid lines represent simulations and markers represent experiments by Wissler and Mazza (2007b).

step is carried out by considering viscous effects using the viscoelastic parameters calibrated in the previous section. During this second step, the outer radius is kept fixed. The load decreases from $\Delta\phi_{max}$ to zero over a number of 24 elements. The radial strain ϵ_r, caused by the application of voltage, of a node in the middle of the active part of the mesh is tracked and compared to the experimental results where

$$\epsilon_r = \lambda_r - 1 = \frac{r_2}{r_1}\lambda_{pre} - 1 \tag{48}$$

and where r_2 and r_1 are the radii (in the active part of the membrane) after and before activation of voltage. The fit between the FE simulation and the experiments can be seen in figures 6 and 7(a) and the material parameters are listed in table 3. Figures 6(a) - 6(c) show the electro-viscoelastic behaviour of the three different pre-stretches applied. Figure 7(a) shows the response after 900 seconds of loading. Note, that this was taken as the equilibrium response in Wissler and Mazza (2007b) and differs from the electro-elastic equilibrium response predicted by the model which can be seen in

16

(a) Response at 900 s. (b) Equilibrium response.
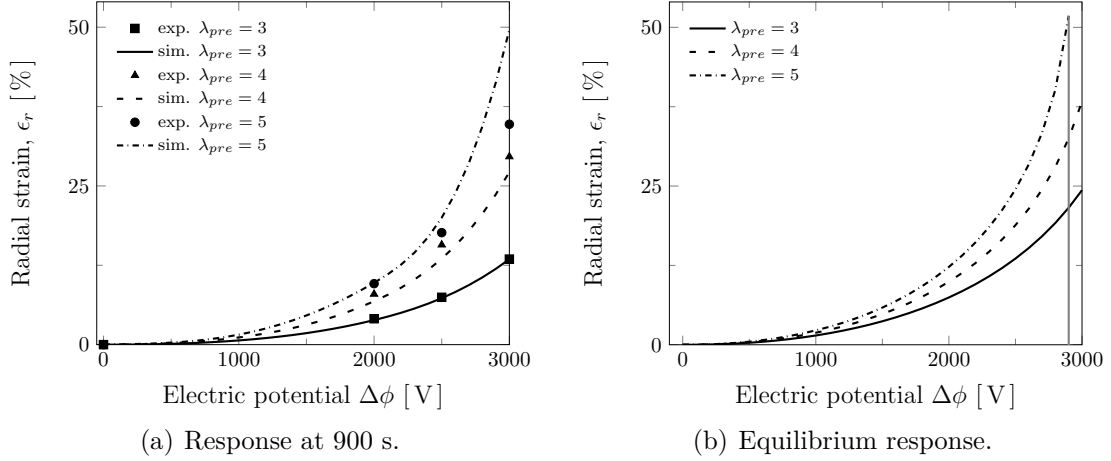
Figure 7: Electro-viscoelastic response at 900 seconds, (a), and equilibrium response, (b). Experimental data taken from Wissler and Mazza (2007b).

Table 3: Electroelastic material parameters.

$$
\begin{aligned}
c_1 \ [\mathrm{F\ m^{-1}}] &= -2.3292 \cdot 10^{-10} \\
c_2 \ [\mathrm{V\ m^{-1}}] &= 1 \\
b &= -1.3282 \\
m &= 1.0899
\end{aligned}
$$

figure 7(b). For a pre-stretch of 5 the highest voltage gives rise to numerical difficulties which eventually lead to a loss of convergence in the simulation, as is highlighted in figure 7(b) with a vertical line, indicating where the simulation stopped. Figure 8 shows a small portion of the activated membrane for $\lambda_{pre} = 4$. Figures 8(a) and 8(b) show how the load decreases over the elements and illustrate the related geometry and mesh. Figures 8(c) and 8(d) are contourplots of the mechanical (connected to Ω^{vol}, $\Omega^{e\infty}$ and Ω^{ev}) and coupled (connected to Ω^{eel}) contributions of the total nominal Piola stress in the direction of the electric field, i.e. $T_{zz} = \boldsymbol{e}_z \cdot \boldsymbol{T} \cdot \boldsymbol{e}_z$. Only a small section of the geometry, at the border between active and passive part, is shown due to the large difference between radius and thickness of the pre-stretched membrane.

6   Summary and conclusions

A micromechanically motivated constitutive model for dielectric elastomers is established using a microsphere framework. The work takes into account the time-dependent viscous and nearly incompressible behaviour, often seen in dielectric elastomers, using non-affine kinematics. The electromechanically coupled free energy is altered to fit the response of a specific choice of dielectric elastomer, namely VHB 4910 from 3M. A total of 28 material parameters are calibrated, both through pre-
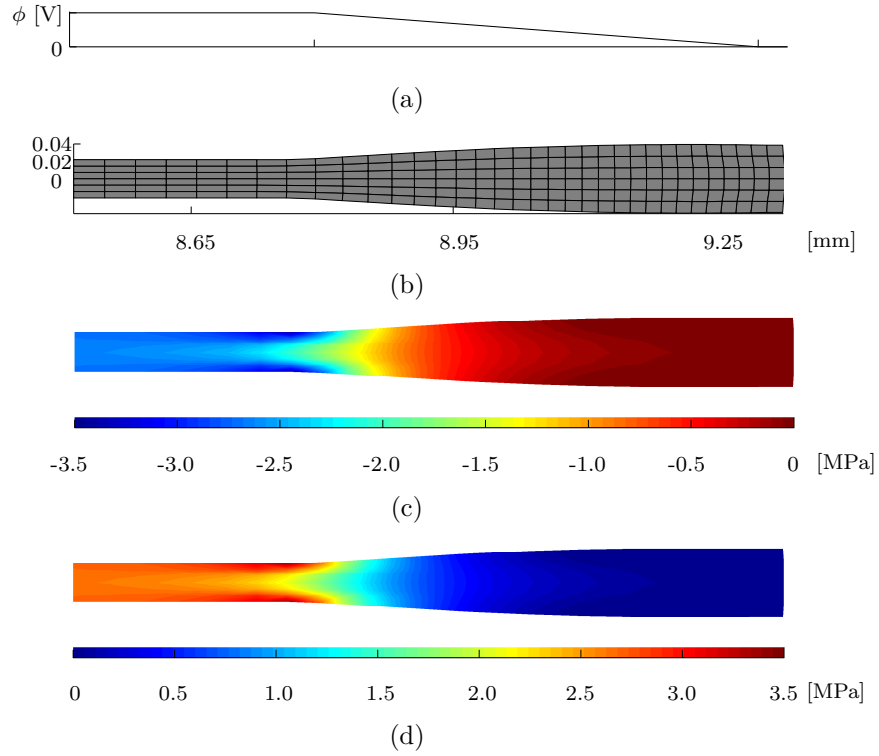
Figure 8: Electrical boundary conditions and mesh, (a)-(b), as well as contourplots of mechanical, (c), and coupled, (d), contributions of the total Piola stress T_{zz}. Only a small portion around the boundary between the active and passive part of the entire geometry is shown.

scribed homogeneous deformation examples and through finite element analysis for inhomogeneous states of deformation. The resulting set of material parameters is able to reproduce arbitrary cases in terms of loading rates, relaxation and pre-stretches. This, combined with simulated response in reasonable agreement with experiments, motivates the use of micromechanically motivated models for dielectric elastomers. Although a vast number of experiments have been made on VHB, the large, time-dependent and incompressible stretches that are involved in the electromechanically coupled FE simulations performed in this work, complicates the calibration and therefore more electromechanically coupled experiments at homogeneous states of deformation are desirable.

Acknowledgements

A   Internal variables

We adopt the model proposed in Miehe and Göktepe (2005) and split the microscopic dissipation function $\varkappa$ into two parts which assume the following form

$$\varkappa_y = \sum_{a=1}^{s} \frac{\delta_y^a}{\eta_y^a \left[1 + \delta_y^a \right]} \left[\eta_y^a |\dot{\varepsilon}_y^a| \right]^{\left[1 + \delta_y^a \right]/\delta_y^a} , \tag{49}$$

where δ_y^a and η_y^a are material parameters. Combining eq. (49) with eq. (38) then gives the following evolution equations for ε_y^a

$$\dot{\varepsilon}_y^a = \frac{1}{\eta_y^a} |\beta_y^a|^{\delta_y^a - 1} \beta_y^a \quad \text{with} \quad \varepsilon_y^a \big|_{t=0} = 0 , \tag{50}$$

where $|(\bullet)| = \sqrt{\left[\frac{(\bullet)}{\text{unit}(\bullet)} \right]^2}$ is a special unit norm operator. The time derivative of $\boldsymbol{\beta}_y$ together with eq. (50) results in the $2\,s$ differential equations

$$\dot{\beta}_y^a + \frac{1}{\tau_y^a} |\beta_y^a|^{\delta_y^a - 1} \beta_y^a = \mu_y^a \frac{\mathrm{d}}{\mathrm{d}t} \left[\ln\left(\lambda_y \right) \right] , \tag{51}$$

where $\beta_y^a \big|_{t=0} = 0$ and $\tau_y^a = \frac{\eta_y^a}{\mu_y^a}$ are relaxations times. The differential eq. (51) is solved iteratively with an Euler backward scheme. For more details regarding the microscopic dissipation function see Miehe and Göktepe (2005).

B   Flux terms

The elastic equilibrium contributions to the stresses, evaluated on the microsphere, include the following partial derivatives

$$n \, \partial_{\bar{\boldsymbol{C}}} \Omega^{e\infty,f}\left(\langle \lambda_{f_i} \rangle_p \right) \approx n \, \frac{\partial \Omega^{e\infty,f}}{\partial \lambda_f} \lambda_f^{1-p} \frac{1}{2} \sum_{i=1}^{\text{nid}} \lambda_{f_i}^{p-2} \, \boldsymbol{n}_i \otimes \boldsymbol{n}_i \, \omega_i , \tag{52}$$

$$n \, \partial_{\bar{\boldsymbol{C}}} \langle \, \Omega^{e\infty,c}\left(\lambda_{c_i}^q \right) \rangle \approx -n \, \frac{1}{2} \sum_{i=1}^{\text{nid}} \frac{\partial \Omega_i^{e\infty,c}}{\partial \lambda_{c_i}} \lambda_{c_i}^{-1} \, \tilde{\boldsymbol{n}}_i \otimes \tilde{\boldsymbol{n}}_i \, \omega_i , \tag{53}$$

where $\tilde{\boldsymbol{n}}_i = \bar{\boldsymbol{C}}^{-1} \cdot \boldsymbol{n}_i$. The visco-elastic contributions to the stresses, evaluated on the microsphere, include the following partial derivatives

$$n \, \partial_{\bar{\boldsymbol{C}}} \langle \, \Omega^{ev,f}\left(\lambda_{f_i}, \varepsilon_f^a \right) \rangle \approx n \, \frac{1}{2} \sum_{i=1}^{\text{nid}} \frac{\partial \Omega_i^{ev,f}}{\partial \lambda_{f_i}} \lambda_{f_i}^{-1} \, \boldsymbol{n}_i \otimes \boldsymbol{n}_i \, \omega_i , \tag{54}$$

$$n \, \partial_{\bar{\boldsymbol{C}}} \langle \, \Omega^{ev,c}\left(\lambda_{c_i}, \varepsilon_c^a \right) \rangle \approx -n \, \frac{1}{2} \sum_{i=1}^{\text{nid}} \frac{\partial \Omega_i^{ev,c}}{\partial \lambda_{c_i}} \lambda_{c_i}^{-1} \, \tilde{\boldsymbol{n}}_i \otimes \tilde{\boldsymbol{n}}_i \, \omega_i . \tag{55}$$

Table 4: Derivatives of the free energy function of the micro-sphere model.

$$
\begin{aligned}
\partial_J \Omega^{\mathrm{vol}} &= \kappa\,[\,J-1\,] \\
n\,\partial_{\lambda_f}\,\Omega^{e\infty,f} &= \mu_e \frac{3N-\lambda_f^2}{N-\lambda_f^2}\lambda_f \\
n\,\partial_{\lambda_{c_i}}\,\Omega^{e\infty,c} &= \mu_e\,N\,U\,q\,\lambda_{c_i}^{q-1} \\
n\,\partial_{\lambda_{f_i}}\,\Omega^{ev,f} &= \frac{1}{\lambda_{f_i}}\sum_{a=1}^{s}\beta_f^a \\
n\,\partial_{\lambda_{c_i}}\,\Omega^{ev,c} &= \frac{1}{\lambda_{c_i}}\sum_{a=1}^{s}\beta_c^a \\
n\,\partial_{\Lambda}\,\Omega^{eel} &= m\,c_1\,\Lambda^{m-1}
\end{aligned}
$$

The electro-elastic contribution to the stresses, evaluated on the microsphere, include the following partial derivatives

$$
n\,\partial_{\bar{\boldsymbol{C}}}\,\Omega^{eel}(\,\langle\,\Lambda_i\,\rangle\,) \approx n\,\frac{\partial\Omega^{eel}}{\partial\Lambda}\,\frac{1}{2}\,b\,c_2^{-2}\sum_{i=1}^{\mathrm{nid}}\lambda_{f_i}^{b-2}\,E_i^2\,\boldsymbol{n}_i\otimes\boldsymbol{n}_i\,\omega_i\,. \tag{56}
$$

The electro-elastic contribution to the electric displacements, evaluated on the micro-sphere, includes the following partial derivatives

$$
n\,\partial_{\boldsymbol{E}}\,\Omega^{eel}(\,\langle\,\Lambda_i\,\rangle\,) \approx n\,\frac{\partial\Omega^{eel}}{\partial\Lambda}\,2\,c_2^{-2}\sum_{i=1}^{\mathrm{nid}}\lambda_{f_i}^{b}\,E_i\,\boldsymbol{n}_i\,\omega_i\,, \tag{57}
$$

wherein $\Lambda = c_2^{-2}\sum_{i=1}^{\mathrm{nid}}\lambda_{f_i}^{b}\,E_i^2\,\omega_i$.

The partial derivatives with respect to variables $J, \lambda_f, \lambda_{f_i}, \lambda_{c_i}$ and Λ are summarised in Table 4 where $\mu_e = n\,k\,T$ is introduced.

References

Ask, A., Denzer, R., Menzel, A., Ristinmaa, M., 2013. Inverse-motion-based form finding for quasi-incompressible finite electroelasticity. Int. J. Numer. Methods Engng 94 (6), 554–572.

Ask, A., Menzel, A., Ristinmaa, M., 2012a. Electrostriction in electro-viscoelastic polymers. Mech. Mater. 50, 9–21.

Ask, A., Menzel, A., Ristinmaa, M., 2012b. Phenomenological modeling of viscous electrostrictive polymers. Int. J. Non-Linear Mech. 47 (2), 156–165.

Ask, A., Menzel, A., Ristinmaa, M., 2015. Modelling of Viscoelastic Dielectric Elastomers with Deformation Dependent Electric Properties. Procedia IUTAM 12, 134–144.

Bažant, Z. P., Oh, B. H., 1983. Microplane model for fracture analysis of concrete structures. Proc. Symp. Interact. Non-Nucl. Munitions Struct., 49–55.

Bažant, Z. P., Oh, B. H., 1986. Efficient numerical integration on the surface of a sphere. Z. Angew. Math. Mech. 66 (1), 37–49.

Büschel, A., Klinkel, S., Wagner, W., 2013. Dielectric elastomers – numerical modeling of nonlinear visco-electroelasticity. Int. J. Numer. Methods Engng 93 (8), 834–856.

Carol, I., Jirásek, M., Bažant, Z. P., 2004. A framework for microplane models at large strain, with application to hyperelasticity. Int. J. Solids Struct. 41 (2), 511–557.

Chiang Foo, C., Cai, S., Jin Adrian Koh, S., Bauer, S., Suo, Z., 2012. Model of dissipative dielectric elastomers. J. Appl. Phys. 111 (3), 034102.

Di Lillo, L., Schmidt, A., Carnelli, D. A., Ermanni, P., Kovacs, G., Mazza, E., Bergamini, A., 2012. Measurement of insulating and dielectric properties of acrylic elastomer membranes at high electric fields. J. Appl. Phys. 111 (2), 024904.

Doi, M., Edwards, S. F., 1986. The Theory of Polymer Networks. Clarendon Press.

Dorfmann, A., Ogden, R. W., 2005. Nonlinear electroelasticity. Acta Mech. 174 (3), 167–183.

Eringen, A. C., 1989. Mechanics of Continua. Krieger.

Ethiraj, G., Zäh, D., Miehe, C., 2013. A finite deformation microsphere model for magneto-visco-elastic response in magnetorheological elastomers. PAMM 13 (1), 197–198.

Hossain, M., Vu, D. K., Steinmann, P., 2012. Experimental study and numerical modelling of VHB 4910 polymer. Comp. Mater. Sci. 59, 65–74.

Hossain, M., Vu, D. K., Steinmann, P., 2015. A comprehensive characterization of the electro-mechanically coupled properties of VHB 4910 polymer. Arch. Appl. Mech. 85 (4), 523–537.

Jackson, D., 1962. Classical Electrodynamics. John Wiley & Sons, Inc.

Jean-Mistral, C., Sylvestre, A., Basrour, S., Chaillout, J.-J., 2010. Dielectric properties of polyacrylate thick films used in sensors and actuators. Smart Mater. Struct. 19 (7), 075019.

Khan, K. A., Wafai, H., Sayed, T. E., 2013. A variational constitutive framework for the nonlinear viscoelastic response of a dielectric elastomer. Comput. Mech. 52 (2), 345–360.

Kofod, G., Sommer-Larsen, P., Kornbluh, R., Pelrine, R., 2003. Actuation response of polyacrylate dielectric elastomers. J. Intel. Mat. Syst. Str. 14 (12), 787–793.

Kornbluh, R. D., Pelrine, R., Pei, Q., Oh, S., Joseph, J., 2000. Ultrahigh strain response of field-actuated elastomeric polymers. Proc. SPIE 3987, 51–64.

Kovetz, A., 2000. Electromagnetic Theory. Oxford University Press.

Li, B., Chen, H., Qiang, J., Hu, S., Zhu, Z., Wang, Y., 2011. Effect of mechanical pre-stretch on the stabilization of dielectric elastomer actuation. J. Phys. D: Appl. Phys 44 (15), 155301.

Linder, C., Tkachuk, M., Miehe, C., 2011. A micromechanically motivated diffusion-based transient network model and its incorporation into finite rubber viscoelasticity. J. Mech. Phys. Solids 59 (10), 2134–2156.

Liu, L., Chen, H., Sheng, J., Zhang, J., Wang, Y., Jia, S., 2014. Experimental study on the dynamic response of in-plane deformation of dielectric elastomer under alternating electric load. Smart Mater. Struct. 23 (2), 025037.

McKay, T. G., Calius, E., Anderson, I. A., 2009. The dielectric constant of 3M VHB: a parameter in dispute. Proc. SPIE 7287, 72870P–72870P–10.

Menzel, A., Waffenschmidt, T., 2009. A microsphere-based remodelling formulation for anisotropic biological tissues. Phil. Trans. R. Soc. A 367 (1902), 3499–3523.

Miehe, C., Göktepe, S., 2005. A micro–macro approach to rubber-like materials. Part II: The micro-sphere model of finite rubber viscoelasticity. J. Mech. Phys. Solids 53 (10), 2231–2258.

Miehe, C., Göktepe, S., Lulei, F., 2004. A micro-macro approach to rubber-like materials—Part I: the non-affine micro-sphere model of rubber elasticity. J. Mech. Phys. Solids 52 (11), 2617–2660.

O'Halloran, A., O'Malley, F., McHugh, P., 2008. A review on dielectric elastomer actuators, technology, applications, and challenges. J. Appl. Phys. 104 (7), 071101.

Ostwald, R., Bartel, T., Menzel, A., 2015. An energy-barrier-based computational micro-sphere model for phase-transformations interacting with plasticity. Comput. Methods Appl. Mech. Engng. 293, 232–265.

Pelrine, R., Kornbluh, R., Kofod, G., 2000a. High-Strain Actuator Materials Based on Dielectric Elastomers. Adv. Mater. 12 (16), 1223–1225.

Pelrine, R., Kornbluh, R., Pei, Q., Joseph, J., 2000b. High-speed electrically actuated elastomers with strain greater than 100%. Science 287 (5454), 836–839.

Pelrine, R., Kornbluh, R. D., Eckerle, J., Jeuck, P., Oh, S., Pei, Q., Stanford, S., 2001a. Dielectric elastomers: generator mode fundamentals and applications. Proc. SPIE 4329, 148–156.

Pelrine, R., Sommer-Larsen, P., Kornbluh, R. D., Heydt, R., Kofod, G., Pei, Q., Gravesen, P., 2001b. Applications of dielectric elastomer actuators 4329, 335–349.

Qiang, J., Chen, H., Li, B., 2012. Experimental study on the dielectric properties of polyacrylate dielectric elastomer. Smart Mater. Struct. 21 (2), 025006.

Rasmussen, L. (Ed.), 2012. Electroactivity in Polymeric Materials. Springer.

Sahu, R., Patra, K., Szpunar, J., 2015. Experimental study and numerical modelling of creep and stress relaxation of dielectric elastomers. Strain 51 (1), 43–54.

Saxena, P., Vu, D. K., Steinmann, P., 2014. On rate-dependent dissipation effects in electro-elasticity. Int. J. Non-Linear Mech. 62, 1–11.

Tagarielli, V., Hildick-Smith, R., Huber, J., 2012. Electro-mechanical properties and electrostriction response of a rubbery polymer for {EAP} applications. Int. J. Solids Struct. 49 (23–24), 3409–3415.

Thylander, S., Menzel, A., Ristinmaa, M., 2012. An electromechanically coupled micro-sphere framework: application to the finite element analysis of electrostrictive polymers. Smart Mater. Struct. 21 (9), 094008.

Thylander, S., Menzel, A., Ristinmaa, M., 2013. Corrigendum: An electromechanically coupled micro-sphere framework—application to the finite element analysis of electrostrictive polymers. Smart Mater. Struct. 22 (3), 039501.

Treloar, L. R. G., 1975. Physics of Rubber Elasticity, 3rd Edition. Clarendon Press.

Vogel, F., Göktepe, S., Steinmann, P., Kuhl, E., 2014. Modeling and simulation of viscous electro-active polymers. Eur. J. Mech. A-Solids 48, 112–128.

Vu-Cong, T., Jean-Mistral, C., Sylvestre, A., 2012. Impact of the nature of the compliant electrodes on the dielectric constant of acrylic and silicone electroactive polymers. Smart Mater. Struct. 21 (10), 105036.

Vu-Cong, T., Nguyen-Thi, N., Jean-Mistral, C., Sylvestre, A., 2014. How does static stretching decrease the dielectric constant of VHB 4910 elastomer? Proc. SPIE 9056, 90561P–90561P–8.

Waffenschmidt, T., Menzel, A., Kuhl, E., 2012. Anisotropic density growth of bone—A computational micro-sphere approach. Int. J. Solids Struct. 49 (14), 1928–1946.

Wissler, M., Mazza, E., 2007a. Electromechanical coupling in dielectric elastomer actuators. Sens. Act. A: Phys. 138 (2), 384–393.

Wissler, M., Mazza, E., 2007b. Mechanical behavior of an acrylic elastomer used in dielectric elastomer actuators. Sens. Act. A: Phys. 134 (2), 494–504.

Zäh, D., Miehe, C., 2015. Multiplicative electro-elasticity of electroactive polymers accounting for micromechanically-based network models. Comput. Methods Appl. Mech. Engng. 286, 394–421.

Zhang, J., Wang, Y., McCoul, D., Pei, Q., Chen, H., 2014. Viscoelastic creep elimination in dielectric elastomer actuation by preprogrammed voltage. Appl. Phys. Lett. 105 (21), 212904.

Zhao, X., Koh, S. J. A., Suo, Z., 2011. Nonequilibrium thermodynamics of dielectric elastomers. Int. J. Appl. Mech. 03 (02), 203–217.

Paper C

S. Thylander, A. Menzel and M. Ristinmaa

Towards control of viscous effects in acrylic-based actuator applications

Towards control of viscous effects in acrylic-based actuator applications

Sara Thylander[a], Andreas Menzel[a,b] and Matti Ristinmaa[a]

[a] Division of Solid Mechanics, Lund University

P.O. Box 118, S-221 00 Lund, Sweden

[b] Department of Mechanical Engineering, Institute of Mechanics, TU Dortmund

Leonhard-Euler-Str. 5, D-44227 Dortmund, Germany

Abstract

Dielectric elastomers offer clear advantages over more traditional and conventional materials when soft, light-weight, noise-less actuator applications with large deformations are considered. However, the viscous time-dependent behaviour associated with most elastomers limit the number of possible applications. For this purpose, the possibility of controlling the viscous response by regulating the applied electric potential is explored. The constitutive model chosen is calibrated to fit the electro-viscoelastic response of an acrylic elastomer often used in dielectric elastomer actuators. The response of both homogeneous deformation examples and inhomogeneous finite element boundary value problems, chosen to mimic existing applications, are presented. Control of both force and displacement quantities is successfully achieved.

1 Introduction

Dielectric elastomers (DEs) are non-conducting polymers with low elastic modulus. A thin elastomeric film coated on both sides with compliant electrodes constitutes the basic setup of a dielectric elastomer actuator (DEA). When the electrodes are connected to an electric field the opposite charges attract each other. As a result the thickness decreases and the in-plane area increases. The latter being a consequence of the incompressible nature of most elastomers. Actuation based on this, often called the Maxwell effect, is the main actuation mechanism in DEs, but some inherent electrostriction due to small amounts of crystallinity can also be found, see Romasanta et al. (2015). Although all dielectric materials will experience this type of electrostatic effect, two of the most investigated and used types are silicone- and acryclic-based. This is mainly due to their combination of low elastic modulus and high specific energy density, see Carpi et al. (2011b). In a comparison between silicone- and acrylic-based electroactive actuators, the former is advantageous due to smaller viscous effects, while the latter is favorable in applications requiring strains larger than 10% due to a lower secant modulus, see Michel et al. (2010). Acrylic-based dielectric elastomers have shown great potential in applications where muscle-like actuation (soft, noise-less) is needed. Its high energy density as well as large-strain actuation and fast response characteristics enable light-weight, easy to shape and comparably low-cost components. Areas of applications where acrylic-based DEs successfully replaced more traditional materials include tactile feedback, see Carpi et al. (2010, 2012) and Ren et al. (2014), loudspeakers, see Heydt et al. (2006); Graf and Maas (2012) and Hosoya et al. (2015), tunable lenses, see Carpi et al. (2011a) and Blum et al. (2012), micropumps, see Loverich et al. (2006) and generators in energy harvest systems, see Kornbluh et al. (2011) and Chiba et al. (2013). Two illustrations are provided in figure 1. The increased interest in this field of applications has yielded a first standard for assessment and comparison between different materials and devices, see Carpi et al. (2015).
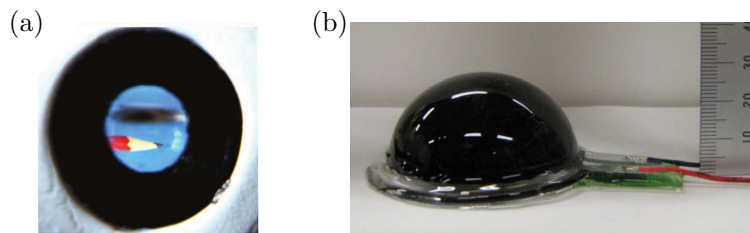
(a) (b)

Figure 1: Examples of applications including dielectric elastomers. (a) Tunable lens from Carpi et al. (2011a). Reprinted with permission. Copyright 2011 WILEY-VCH Verlag GmbH & Co. KGaA, Weinheim. (b) Loudspeaker. Reprinted with permission from Hosoya et al. (2015). Copyright 2015, Acoustic Society of America.

In terms of applications the rate-dependent viscous effects found in acrylic-based materials often need to be controlled. The dissipative processes taking place in a DEA can be divided into three main categories; viscoelastic, dielectric and conductive. The viscoelastic and dielectric relaxation are due to processes on the molecular level in

terms of slippage between polymer chains and reorientation of dipoles respectively. Conductive relaxation, due to the presence of a leakage current as a result of the transport of electrons and ions, is a long-range motion. The three dissipative processes take place on different time scales, ranging from milliseconds (dielectric), minutes (viscoelastic) to hours (conductive), see Suo (2010); Zhao et al. (2011) and Chiang Foo et al. (2012).

As applications including DEAs continue to increase, the need rises for reliable and robust material models based on profound understanding of the underlyings physics. The time-dependent behaviour of DEAs needs to be taken into account in order to successfully mimic existing applications. To meet this requirement, much of the recent work on DEA, both in terms of modelling and experiments, deals with its time-dependent effects. Recent observations found in Miles et al. (2015) of the dissipative behaviour of DEAs includes an experimental investigation of viscous effects analysed by using the Bayesian uncertainty analysis. In Park and Nguyen (2013) the shear and bulk relaxation times and its connection to electromechancial instability is examined by using a viscoelastic finite element model. Experiments related to viscoelastic instabilities in DE transducers are investigated in Kollosche et al. (2015). Different voltage waveforms and their impact on dissipation are investigated in Zhang et al. (2016). An assessment of the efficiency of a dielectric elastomer generator in relation to viscous effects can be found in Bortot et al. (2016).

In this work, the electro-viscoelastic model developed within the micro-sphere framework in Thylander et al. (2012, 2013), further extended to include viscous behaviour as well as non-affine kinematics and calibrated to VHB 4910 in Thylander et al. (2016), is utilised to show the effect of dissipative processes in common acrylics-based DE applications. The possibility of controlling these viscous effects by regulating the applied electric potential difference is investigated. This possibility may allow further enhancement of applications. Similar attempts to eliminate problems coherent with dissipative effects can be found in, for example, Zhang et al. (2014b) and Zhang et al. (2014a). Both contributions are able to successfully eliminate creep under the assumption of homogeneous deformation by tuning of the applied electric potential difference. In this work we extend this analysis to inhomogeneous deformation states as well as to include control with respect to both deformation and force quantities. In Zhang et al. (2015) a dynamic viscoelastic model for dielectric elastomers is established for study of oscillations and stability evolution. The effect of creep is successfully eliminated by tuning the in-plane tensile forces that comprises the pre-stretch of a DEA. In this work the inertial forces are not taken into account. The principle of the control is illustrated by means of two examples under homogeneous states of deformation and is then further explored in two finite element (FE) boundary value problems (BVPs). The finite element examples implemented are chosen to resemble existing DE applications.

2 Basic relations

This section summarises the basic relations that govern a general quasi-electrostatic but time dependent electromechanically coupled problem. For brevity, the relations

used in this work are merely summarised, for full background theory we refer to the references stated in each subsection.

2.1 Kinematics

Consider the position of a material particle denoted by the vector $\boldsymbol{X}$ in the material configuration $\mathcal{B}_0$ and by the vector $\boldsymbol{x} = \boldsymbol{\varphi}(\boldsymbol{X}, t)$ in the spatial configuration $\mathcal{B}_t$, in which $\boldsymbol{\varphi}$ denotes the point space map and t represents time. The deformation gradient tensor $\boldsymbol{F}$ is defined as $\boldsymbol{F} = \nabla_{\boldsymbol{X}}\, \boldsymbol{\varphi}$ with the related determinant, $J = \det(\boldsymbol{F}) > 0$, and cofactor, $\mathrm{cof}(\boldsymbol{F}) = \partial_{\boldsymbol{F}} J = J\, \boldsymbol{F}^{-\mathrm{t}}$. In view of modelling the nearly incompressible nature of elastomers a multiplicative split of the deformation gradient is introduced with an isochoric part $\bar{\boldsymbol{F}}$, such that $\boldsymbol{F} = J^{1/3}\, \bar{\boldsymbol{F}}$ and where $\det(\bar{\boldsymbol{F}}) = 1$ follows. Based on this split of the deformation gradient, two different right Cauchy-Green tensors can be introduced, $\boldsymbol{C} = \boldsymbol{F}^{\mathrm{t}} \cdot \boldsymbol{F}$ and $\bar{\boldsymbol{C}} = \bar{\boldsymbol{F}}^{\mathrm{t}} \cdot \bar{\boldsymbol{F}}$ so that $\det(\bar{\boldsymbol{C}}) = 1$ follows. For a more detailed description on kinematics of solid continua see Ogden (1997).

2.2 Electric field quantities

This work is restricted to quasi-electrostatics and electromagnetic coupling is not considered. In this case the electric quantities of interest are the electric field, the electric displacement and the polarization, here denoted $\boldsymbol{e}$, $\boldsymbol{d}$ and $\boldsymbol{\pi}$ in the spatial configuration and $\boldsymbol{E}$, $\boldsymbol{D}$ and $\boldsymbol{\Pi}$ in the material configuration. The interdependence of these electric quantities, in the spatial configuration, is governed by

$$\boldsymbol{d} = \varepsilon_0\, \boldsymbol{e} + \boldsymbol{\pi}\,, \tag{1}$$

where ε_0 denotes the vacuum electric permittivity. The referential counterpart is given by

$$\boldsymbol{D} = J\, \varepsilon_0\, \boldsymbol{E} \cdot \boldsymbol{C}^{-1} + \boldsymbol{\Pi}\,, \tag{2}$$

where $\boldsymbol{E} = \boldsymbol{e} \cdot \boldsymbol{F}$, $\boldsymbol{D} = \boldsymbol{d} \cdot \mathrm{cof}(\boldsymbol{F})$ and $\boldsymbol{\Pi} = \boldsymbol{\pi} \cdot \mathrm{cof}(\boldsymbol{F})$. For a full background description on electromagnetic theory see Kovetz (2000).

2.3 Balance equations

In the absence of magnetic fields, free electric charges and any time dependencies we consider the specialisation of Maxwell's equations where the spatial vectorial fields of the electric displacements, $\boldsymbol{d}$, and electric field, $\boldsymbol{e}$, satisfy

$$\nabla_{\boldsymbol{x}} \cdot \boldsymbol{d} = 0 \quad \text{and} \quad \nabla_{\boldsymbol{x}}^{\mathrm{t}} \times \boldsymbol{e} = \boldsymbol{0}\,. \tag{3}$$

The referential representations in $\mathcal{B}_0$ read

$$\nabla_{\boldsymbol{X}} \cdot \boldsymbol{D} = 0 \quad \text{and} \quad \nabla_{\boldsymbol{X}}^{\mathrm{t}} \times \boldsymbol{E} = \boldsymbol{0}\,. \tag{4}$$

The curl-free electric field enables a representation of the electric field as the gradient of a scalar-valued field, here taken as the electric potential, $\phi(\boldsymbol{X}, t)$, such that

$$\boldsymbol{e} = -\nabla_{\boldsymbol{x}}\, \phi \quad \text{and} \quad \boldsymbol{E} = -\nabla_{\boldsymbol{X}}\, \phi\,. \tag{5}$$

4

The additional body force introduced by the electric field and its interaction with matter is taken as $\boldsymbol{f}^{\mathrm{e}} = \nabla_{\boldsymbol{x}} \boldsymbol{e} \cdot \boldsymbol{\pi} = \nabla_{\boldsymbol{x}} \cdot \left[\boldsymbol{e} \otimes \boldsymbol{d} - \frac{1}{2} [\boldsymbol{e} \cdot \boldsymbol{e}] \boldsymbol{I} \right]$, with $\boldsymbol{I}$ being the second order identity tensor, cf. Dorfmann and Ogden (2005). The introduction of this body force renders the Cauchy stress $\boldsymbol{\sigma}$ to be, in general, unsymmetric. The spatial representation of the quasi-static form of the balance of linear momentum (for a closed system where mass is conserved) then reads

$$\nabla_{\boldsymbol{x}} \cdot \boldsymbol{\sigma} + \boldsymbol{f}^{\mathrm{e}} + \rho \, \boldsymbol{f} = \boldsymbol{0} \,, \tag{6}$$

where $\boldsymbol{f}$ represents the mechanical body force and ρ the current mass density. By shifting the electric body force to the mechanical flux term a symmetric total stress tensor $\boldsymbol{\tau} = \boldsymbol{\sigma} + \boldsymbol{e} \otimes \boldsymbol{d} - \frac{1}{2} \varepsilon_0 [\boldsymbol{e} \cdot \boldsymbol{e}] \boldsymbol{I}$ can be introduced such that eq. (6) corresponds to

$$\nabla_{\boldsymbol{x}} \cdot \boldsymbol{\tau} + \rho \, \boldsymbol{f} = \boldsymbol{0} \,. \tag{7}$$

The material counterpart of eq. (7) reads

$$\nabla_{\boldsymbol{X}} \cdot \boldsymbol{T} + \rho_0 \, \boldsymbol{f} = \boldsymbol{0} \,, \tag{8}$$

where $\boldsymbol{T} = \boldsymbol{\tau} \cdot \mathrm{cof}(\boldsymbol{F})$ and $\rho_0 = J \rho$. For further details on the interaction of electromechanically coupled continua the reader is referred to Maugin (1988).

2.4 Constitutive relations

An amended free energy Ω, see Dorfmann and Ogden (2005), is defined in terms of the deformation gradient $\boldsymbol{F}$, the referential electric field $\boldsymbol{E}$ and internal variables $\boldsymbol{K}$. We assume that the viscous behaviour is governed only by deformation and not by the electric field, thereby neglecting dielectric and conductive dissipative effects. Motivated by experimental observations of the (almost) incompressible behaviour of acrylic-based DEs, an additive split of the free energy into volumetric and isochoric parts is adopted. The isochoric part is further additively split into three main parts; elastic (e_∞), viscoelastic (e_v) and electroelastic (e_{el}), see Ask et al. (2012b,a); Büschel et al. (2013) and Denzer and Menzel (2014), so that

$$\begin{aligned} \Omega(\boldsymbol{F}, \boldsymbol{E}, \boldsymbol{K}) \;\; &= \Omega^{vol}(J) + \Omega^{e\infty}(\bar{\boldsymbol{C}}) + \Omega^{ev}(\bar{\boldsymbol{C}}, \boldsymbol{K}) \\ &\quad + \Omega^{e_{el}}(\bar{\boldsymbol{C}}, \boldsymbol{E}) - \tfrac{1}{2}\varepsilon_0 \, J \, \boldsymbol{C}^{-1} : [\boldsymbol{E} \otimes \boldsymbol{E}] \,. \end{aligned} \tag{9}$$

The free space part, connected to ε_0, is assumed to give negligible contribution and is disregarded hereafter. The following relations for the total stress tensor, $\boldsymbol{T}$, the dielectric displacements, $\boldsymbol{D}$, and the evolution of the internal variables, $\boldsymbol{K}$, ensures thermodynamic consistency, see Thylander et al. (2016),

$$\boldsymbol{T} = \frac{\partial \Omega}{\partial \boldsymbol{F}}, \quad \boldsymbol{D} = -\frac{\partial \Omega}{\partial \boldsymbol{E}} \quad \text{and} \quad -\frac{\partial \Omega}{\partial \boldsymbol{K}} \cdot \dot{\boldsymbol{K}} \geq 0 \,. \tag{10}$$

Constructing a convex dissipation function $\Phi(\dot{\boldsymbol{K}})$ and considering the solution to the initial value problem $\partial_{\boldsymbol{K}} \Omega + \partial_{\dot{\boldsymbol{K}}} \Phi = \boldsymbol{0}$ with $\boldsymbol{K}(t = 0) = \boldsymbol{K}_0$ ensures a positive macroscopic viscous dissipation $\mathcal{D}_{mac} = -\frac{\partial \Omega}{\partial \boldsymbol{K}} \cdot \dot{\boldsymbol{K}}$. The specific constitutive framework and free energy contributions as well as the dissipation function are presented in section 3.

3 Specific constitutive framework and model

In this work we consider the constitutive model established in Thylander et al. (2016). This particular model is based on a non-affine micro-sphere framework established in Miehe et al. (2004) and Miehe and Göktepe (2005), and enables the use of micromechanically motivated and statistical physics-based constitutive relations.

3.1 Scalar-valued kinematic and electric quantities

The specific formats of the free energy associated with isochoric deformation are evaluated in terms of two kinematically independent microscopical variables; the length stretch λ_f and the area stretch λ_c, together with one electric scalar-valued quantity, E, to describe the electric field, i.e.

$$\lambda_f = \frac{r}{r_0}, \quad \lambda_c = \left[\frac{d_0}{d}\right]^2 \quad \text{and} \quad E = -\frac{\Delta\phi}{r_0}, \tag{11}$$

where r_0 and r are the initial and current end-to-end distances of an individual polymer chain, d_0 and d are the reference and current diameters of an imagined tube surrounding an individual chain and $\Delta\phi$ denotes a difference in electric potential. The macroscopic counterparts to the length and area stretch, as well as the scalar-valued electric field, are introduced as projections of the isochoric deformation gradient, $\bar{\boldsymbol{F}}$, and its cofactor, $\mathrm{cof}(\bar{\boldsymbol{F}})$, and the material electric field, $\boldsymbol{E}$, in direction $\boldsymbol{r}_i$ with $\boldsymbol{r}_i \cdot \boldsymbol{r}_i = 1$, such that

$$\lambda_{f_i} = \|\bar{\boldsymbol{F}} \cdot \boldsymbol{r}_i\|, \quad \lambda_{c_i} = \|\mathrm{cof}(\bar{\boldsymbol{F}}) \cdot \boldsymbol{r}_i\| \quad \text{and} \quad E_i = \boldsymbol{E} \cdot \boldsymbol{r}_i. \tag{12}$$

The microscopic counterpart of the internal variables $\boldsymbol{K}$, are denoted by $\boldsymbol{\epsilon}_f$ and $\boldsymbol{\epsilon}_c$. For more details regarding the microscopic internal variables, see Miehe and Göktepe (2005).

3.2 Microsphere formulation

The macroscopic free energy of the continuum is derived in view of the so-called microsphere approach. The framework and specific free energies are briefly summarised here for the reader's convenience, for further details see Carol et al. (2004); Miehe et al. (2004); Miehe and Göktepe (2005); Linder et al. (2011) and Thylander et al. (2016) and references cited therein. The framework rests on the postulate that the free energy at the macroscopic level, $\Omega(\boldsymbol{F}, \boldsymbol{E}, \boldsymbol{K})$, can be derived from a direction average, here denoted $\langle \bullet \rangle$, of a microscopic counterpart $\hat{\Omega}$ over the surface of a unit micro-sphere $\mathbb{U}^2$, i.e.

$$\langle v \rangle = \frac{1}{4\pi} \int_{\mathbb{U}^2} v(A) \, \mathrm{d}A, \tag{13}$$

where v represents a scalar-valued quantity. The integral average can be approximated as a discrete summation over nid integration directions such that

$$\frac{1}{4\pi} \int_{\mathbb{U}^2} v \, \mathrm{d}A \approx \sum_{i=1}^{\mathrm{nid}} v_i \, \omega_i, \tag{14}$$

6

wherein the index i refers to a referential integration direction, $\boldsymbol{r}_i \in \mathbb{U}^2$, with $\|\boldsymbol{r}_i\| = 1$, so that v_i is the value of v in the direction of $\boldsymbol{r}_i$. The scalars ω_i represent non-negative integration weights constrained by $\sum_{i=1}^{\text{nid}} \omega_i = 1$. Also, for the integration scheme chosen as this work proceeds, the integration directions $\boldsymbol{r}_i$ are subjected to constraints, namely $\sum_{i=1}^{\text{nid}} \boldsymbol{r}_i \omega_i = \boldsymbol{0}$ and $\sum_{i=1}^{\text{nid}} \boldsymbol{r}_i \otimes \boldsymbol{r}_i \omega_i = \frac{1}{3} \boldsymbol{I}$. Following Bažant and Oh (1986), 21 integration directions for the hemisphere are assumed to be efficient, so that nid $= 42$. In terms of the microsphere formulation the macroscopic free energy, $\Omega(\boldsymbol{F}, \boldsymbol{E}, \boldsymbol{K})$, is evaluated, in both affine and non-affine manners, so that affine contributions shall be based on $\langle \hat{\Omega}(\lambda_f, \lambda_c, E, \boldsymbol{\epsilon}_f, \boldsymbol{\epsilon}_c) \rangle$ whereas non-affine contributions shall be referred to $\hat{\Omega}(\langle \lambda_f, \lambda_c, E, \boldsymbol{\epsilon}_f, \boldsymbol{\epsilon}_c \rangle)$. The respective forms of affine and non-affine transformations for each part of the free energy are specified in the following section.

3.3   Amended free energy

The specific contributions to the free energy are taken from Thylander et al. (2016), where the formats for the purely mechanical parts can also be found in Miehe and Göktepe (2005). The underlying material parameters were calibrated to fit the response of a popular dielectric elastomer, namely VHB 4910. The volumetric part, Ω^{vol}, is defined in terms of macroscopic quantities directly,

$$\Omega^{vol} = \frac{1}{2}\kappa \left[J - 1 \right]^2 , \tag{15}$$

where κ is the bulk modulus. The isochoric parts are derived from the microscopic counterparts via the following non-affine and affine transformations

$$
\begin{aligned}
\Omega^{e\infty,f}(\bar{\boldsymbol{C}}) &= n\, \hat{\Omega}^{e\infty,f}(\langle \lambda_{f_i} \rangle_p) \\
\Omega^{e\infty,c}(\bar{\boldsymbol{C}}) &= n\, \langle\, \hat{\Omega}^{e\infty,c}(\lambda_{c_i}^q) \,\rangle ,
\end{aligned}
\tag{16}
$$

where p and q are material parameters and where n is the number of polymer chains. Moreover, $\langle v \rangle_p = \sqrt[p]{\langle v^p \rangle}$ represents the p-root average of the scalar variable v, see Miehe et al. (2004). The viscous and electromechanically coupled free energies are transformed through

$$
\begin{aligned}
\Omega^{ev}(\bar{\boldsymbol{C}}, \boldsymbol{K}) &= n\, \langle\, \hat{\Omega}^{ev,f}(\lambda_{f_i}, \boldsymbol{\epsilon}_f) + n\, \langle\, \hat{\Omega}^{ev,c}(\lambda_{c_i}, \boldsymbol{\epsilon}_c) \,\rangle \\
\Omega^{eel}(\bar{\boldsymbol{C}}, \boldsymbol{E}) &= n\, \hat{\Omega}^{eel}(\langle \Lambda_i \rangle) ,
\end{aligned}
\tag{17}
$$

where $\boldsymbol{\epsilon}_f$ and $\boldsymbol{\epsilon}_c$ represent microscopic internal variables. The kinematic quantity $\Lambda_i = c_2^{-2} \lambda_f^b E^2$ is a function of λ_{f_i} and E_i and the parameter c_2 is introduced to normalise the unit of the electric field. Additional material parameters introduced by the coupled free energy include b, m and c_1, see table 1. The material parameters are calibrated so that the format reproduces a non-linear relation between the electric displacement, $\boldsymbol{D}$, and the electric field, $\boldsymbol{E}$. Note, that no specific macroscopic format of $\boldsymbol{\epsilon}_f$ and $\boldsymbol{\epsilon}_c$ is introduced but merely denoted by $\boldsymbol{K}$. The specific formats of the free energy in terms of microscopic independent variables are summarised in table 1. Related material parameters used are listed in table 2. The microscopic dissipation

7

Table 1: Free energy contributions and dissipation function in terms of microscopic quantities. Material parameters needed are summarised in table 2. Furthermore, N is the number of Kuhn segments in an idealised polymer chain, U is a material parameter related to the constraining tube, k is the Boltzmann constant, T the absolute temperature and $\mathcal{L}$ the Langevin function, for more details the reader is referred to Miehe and Göktepe (2005).

$$
\begin{aligned}
\hat{\Omega}^{e\infty,f}(\lambda_f) &= N\,k\,T\left[\lambda_{fr}\,\mathcal{L}^{-1}(\lambda_{fr}) + \ln\left(\frac{\mathcal{L}^{-1}(\lambda_{fr})}{\sinh\left(\mathcal{L}^{-1}(\lambda_{fr})\right)}\right)\right], \qquad \lambda_{fr} = \frac{\lambda_f}{\sqrt{N}} \\
\hat{\Omega}^{e\infty,c}(\lambda_c) &= N\,k\,T\,U\,\lambda_c \\
\hat{\Omega}^{e v,\alpha}(\lambda_\alpha, \boldsymbol{\epsilon}_\alpha) &= \frac{1}{2}\sum_{a=1}^{s} \mu_\alpha^a\left[\ln(\lambda_\alpha) - \epsilon_\alpha^a\right]^2, \qquad \alpha \in [f,c] \\
\hat{\Omega}^{e el}(\lambda_f, E) &= c_1\,\Lambda^m, \qquad \Lambda = c_2^{-2}\lambda_f^b\,E^2 \\
\varkappa_\alpha &= \sum_{a=1}^{s} \frac{\delta_\alpha^a}{\eta_\alpha^a\left[1+\delta_\alpha^a\right]}\left[\eta_\alpha^a\,|\dot{\epsilon}_\alpha^a|\right]^{[1+\delta_\alpha^a]/\delta_\alpha^a}, \qquad \alpha \in [f,c]
\end{aligned}
$$

$\mathcal{D}_{mic}$ is introduced in a similar manner in terms of a direction average so that $\mathcal{D}_{mac} = \langle\mathcal{D}_{mic}\rangle \geq 0$, see Miehe and Göktepe (2005). For each viscous element considered, a number of $2 \times s$ microscopic internal variables, $\boldsymbol{\epsilon}_f$ and $\boldsymbol{\epsilon}_c$, are introduced such that

$$
\mathcal{D}_{mic} = -\frac{\partial\Omega}{\partial\boldsymbol{\epsilon}_\alpha}\cdot\dot{\boldsymbol{\epsilon}}_\alpha \geq 0 \qquad \alpha \in [f,c]. \tag{18}
$$

In this case $s = 4$ was considered sufficient. Similar to the macroscopic setting, the microscopic dissipation remains non-negative by considering the solution to the initial problem

$$
\frac{\partial\Omega}{\partial\boldsymbol{\epsilon}_\alpha} + \frac{\partial\varkappa_\alpha}{\partial\dot{\boldsymbol{\epsilon}}_\alpha} = \mathbf{0} \qquad \alpha \in [f,c], \tag{19}
$$

where $\varkappa_\alpha(\dot{\boldsymbol{\epsilon}}_\alpha)$ is a convex dissipation function with $\boldsymbol{\epsilon}_\alpha|_{t=0} = \mathbf{0}$. The microscopic dissipation function is listed in table 1 whereas the macroscopic dissipation function Φ is not further specified.

4 Numerical examples - control of viscous behaviour

Two different states under homogeneous deformations and two inhomogeneous FE examples are presented. In all cases we consider the electro-viscoelastic model from Thylander et al. (2016) together with calibrated material parameters, found in table 2, for the electro-viscoelastic response of the dielectric elastomer VHB 4910. The material considered is prone to visco-elastic effects. In many applications it is important to be able to control the time-dependent deformation or forces induced by the electric field in order to enable, i.e. predict and design, new and for refinement of existing

Table 2: Material parameters calibrated for VHB 4910, Thylander et al. (2016), wherein $\mu_e = n\,k\,T$ and $\tau_\alpha^a = \eta_\alpha^a / \mu_\alpha^a$ for $\alpha \in \{f, c\}$.

$$
\begin{aligned}
\mu_e\ [\text{Pa}] &= 1.1000 \cdot 10^4 \\
N &= 1.0000 \cdot 10^3 \\
p &= 2.9793 \\
U &= 8.7979 \cdot 10^{-1} \\
q &= 7.0590 \cdot 10^{-4}
\end{aligned}
$$

$$
\begin{aligned}
\boldsymbol{\mu}_f\ [\text{Pa}] &= \begin{bmatrix} 5.6456 \cdot 10^5 & 1.0478 \cdot 10^5 & 7.2672 \cdot 10^4 & 2.5046 \cdot 10^4 \end{bmatrix} \\
\boldsymbol{\mu}_c\ [\text{Pa}] &= \begin{bmatrix} 1.0890 \cdot 10^5 & 2.2915 \cdot 10^4 & 7.4475 \cdot 10^4 & 7.7971 \cdot 10^3 \end{bmatrix} \\
\boldsymbol{\delta}_f &= \begin{bmatrix} 7.7392 \cdot 10^{-1} & 4.8793 \cdot 10^{-1} & 1.9775 & 4.5454 \end{bmatrix} \\
\boldsymbol{\delta}_c &= \begin{bmatrix} 2.4470 & 7.8005 \cdot 10^{-1} & 1.9550 & 1.0631 \end{bmatrix} \\
\boldsymbol{\tau}\ [\text{s}] &= \begin{bmatrix} 2.7824 & 3.7432 \cdot 10^2 & 1.2635 \cdot 10^{-1} & 7.4125 \cdot 10^2 \end{bmatrix}
\end{aligned}
$$

$$
\begin{aligned}
c_1\ [\text{F m}^{-1}] &= -2.3292 \cdot 10^{-10} \\
c_2\ [\text{V m}^{-1}] &= 1 \\
b &= -1.3282 \\
m &= 1.0899
\end{aligned}
$$

applications. This possibility is considered in the presented examples which consider typical deformation patterns and geometries found in existing applications.

For this reason we consider a bisection algorithm to compensate for viscous effects by controlling the applied voltage. The bisection algorithm is constructed to find the difference in applied electric potential, $\Delta\phi$, within the interval $[\Delta\phi_{min} - \Delta\phi_{max}]$ that minimises the relative difference between the electro-elastic and electro-viscoelastic case with respect to a chosen scalar control degree of freedom (e.g. displacement or force), here denoted c, i.e. eliminating large parts of the viscous effects. The response is checked at each load step but could, for faster simulations, be checked less often. A sketch of the algorithm is presented in table 3. When control with respect to forces is considered, we evaluate the sum of the nodal internal forces over a specified part of the boundary. Note, that the specific model considers applications with a response time of minutes and consequently only the viscous type of dissipation is included. For the reader's convenience we introduce the following abbreviations for the four different cases presented; electro-elastic (EE), electro-viscoelastic (EV), electro-viscoelastic including control with respect to displacement (EVD) and electro-viscoelastic including control with respect to force (EVF).

4.1 Homogeneous deformation

We consider two homogeneous deformation examples; uniaxial compression and pure shear, see figure 2. Both cases assume the same initial shape of a cube with side lengths of 1 mm. The difference in electric potential, $\Delta\phi$, is applied in the z-direction and the displacements at the boundaries are specified to obtain the sought deformation.

Table 3: Sketch of bisection algorithm implemented. c_{EE} and c_{EV} denote the electro-elastic and electro-viscoelastic control degrees of freedom.

load $c_{EE}(t)$ from electro-elastic solution
declare starting guess $\Delta\phi$ and interval $\Delta\phi_{max}$, $\Delta\phi_{min}$
for $i = 1$ to nbr steps
    $t = t + \Delta t$
    calculate residual $R = \dfrac{c_{EE}(t) - c_{EV}(\Delta\phi(t))}{c_{EE}(t)}$
    while $|R| > $ TOL
        if $|c_{EE}(t)| \leq |c_{EV}(\Delta\phi(t))|$
            $\Delta\phi_{max} = \Delta\phi$
            $\Delta\phi = \Delta\phi - \dfrac{\Delta\phi_{max} - \Delta\phi_{min}}{2}$
        else
            $\Delta\phi_{min} = \Delta\phi$
            $\Delta\phi = \Delta\phi + \dfrac{\Delta\phi_{max} - \Delta\phi_{min}}{2}$
        end
        obtain solution, $c_{EV}(\Delta\phi(t))$ to BVP by means of FE or constitutive driver
        update residual $R = \dfrac{c_{EE}(t) - c_{EV}(\Delta\phi(t))}{c_{EE}(t)}$
    end
    accept $c_{EV}(\Delta\phi(t))$ and $\Delta\phi(t)$ and save
end

A maximum of 5 kV is ramped up linearly over a period of 0.5 seconds and then kept constant for 900 seconds. In both homogeneous deformation examples Poisson's ratio is set to 0.498.
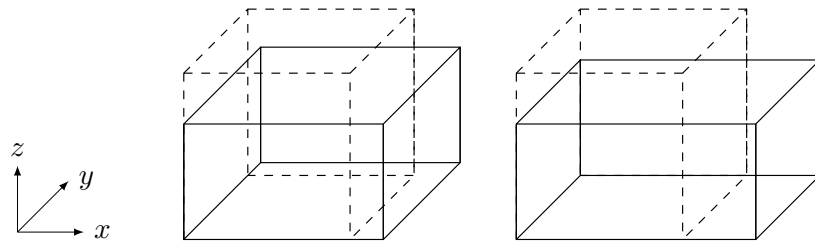
Figure 2: Sketch of homogeneous deformation examples used, uniaxial compression (left) and pure shear (right). Dashed lines indicate the initial shape and solid lines indicate the deformed shape.

4.1.1 Uniaxial compression

The first homogeneous deformation considers a cube that undergoes uniaxial compression with the resulting deformation gradient

$$\boldsymbol{F} = \lambda\,\boldsymbol{e}_z \otimes \boldsymbol{e}_z + \frac{1}{\sqrt{\lambda}}\left[\boldsymbol{I} - \boldsymbol{e}_z \otimes \boldsymbol{e}_z\right]. \qquad (20)$$

The displacement in the x-direction, $\Delta x = x - X$, of the electro-elastic case is compared to that of the electro-viscoelastic case, and the relative difference between the two is minimised by controlling the electric potential $\Delta\phi$.
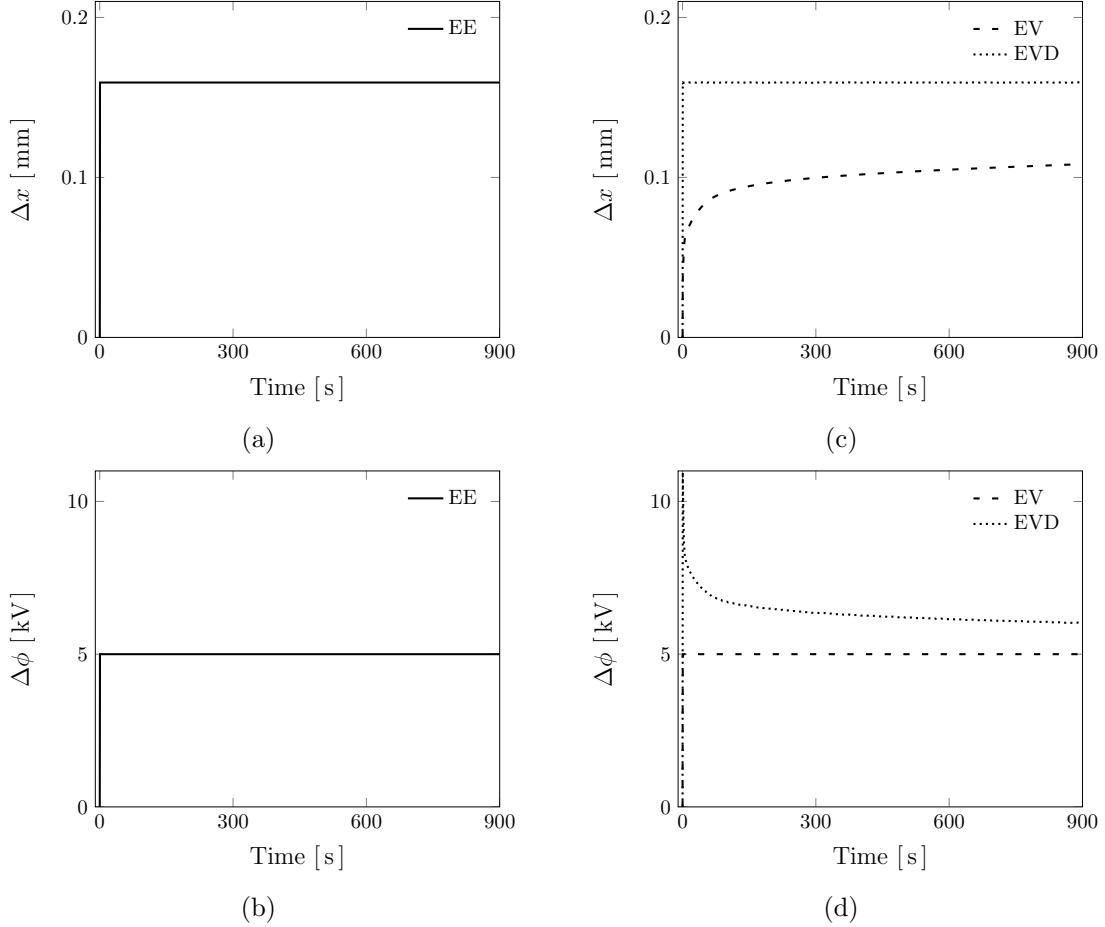
Figure 3: Uniaxial compression: displacement, Δx, and difference in electric potential, $\Delta\phi$, of the EE case in (a) and (b) and of EV and EVD in (c) and (d) respectively. Note, that $\Delta\phi$ is the input to the system, whereas Δx is the response.

In figures 3(a) and 3(b) the response of the EE case is shown where a constant displacement Δx is obtained (after the load ramp) for a given constant load $\Delta\phi$. The EV results are shown in figures 3(c) and 3(d) with dashed lines. As expected, for the same given constant value of $\Delta\phi$, the displacements Δx do not reach their final value immediately but start off at a lower value and asymptotically converge towards the value of the EE case over time. The last loading case, marked with dotted lines in

11

figures 3(c) and 3(d), considers the EVD case. The displacements follow the same path as in the EE case, however it requires the electric potential $\Delta\phi$ to start off at a significantly higher value and then to gradually decrease to that of the EE case.

4.1.2 Pure shear

The second homogeneous example considers a cube that undergoes pure shear with the following deformation gradient

$$\boldsymbol{F} = \frac{1}{\lambda}\, \boldsymbol{e}_x \otimes \boldsymbol{e}_x + \lambda\, \boldsymbol{e}_z \otimes \boldsymbol{e}_z + \boldsymbol{e}_y \otimes \boldsymbol{e}_y\,. \tag{21}$$

The force in the y-direction, f_y, of the electro-elastic case is compared to that of the electro-viscoelastic case, and the relative difference between them is minimised by controlling the electric potential. The force is evaluated as the sum of the nodal internal forces on one side of the cube.
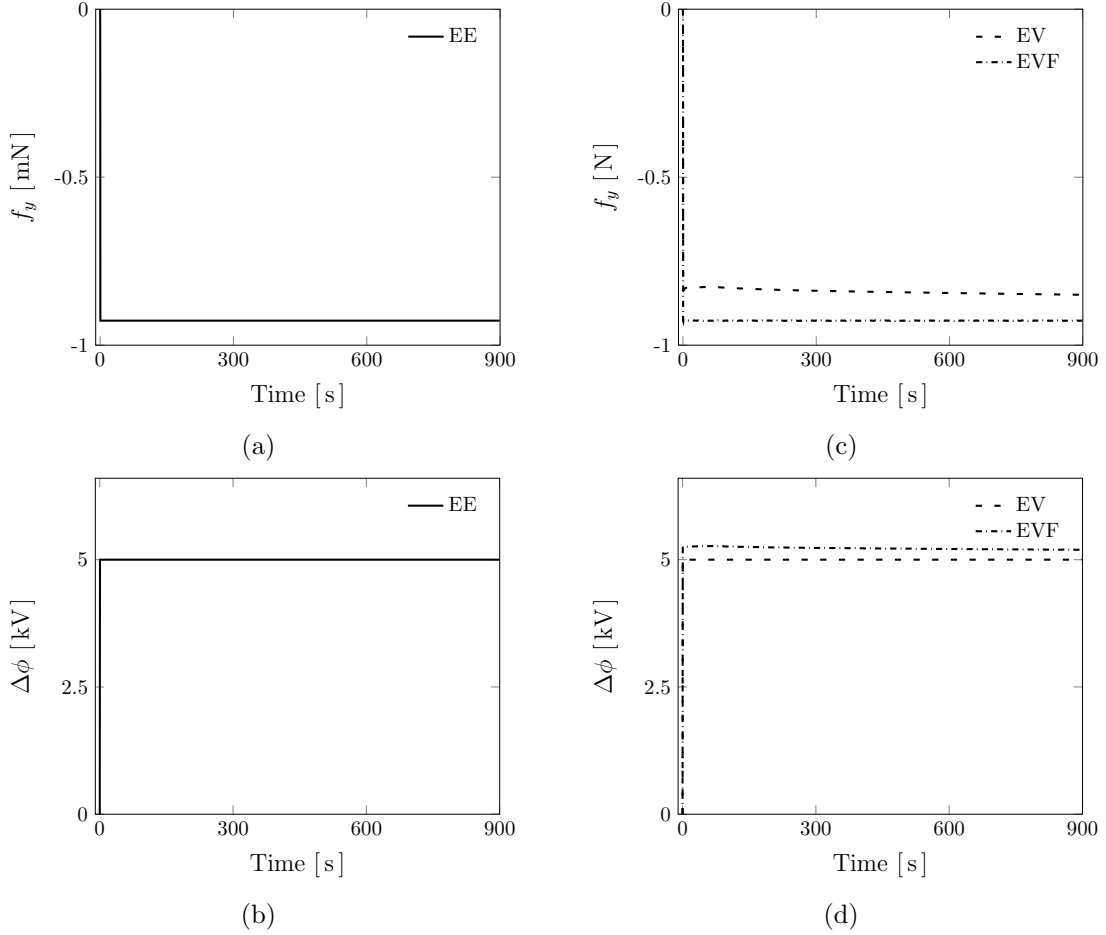
Figure 4: Pure shear: force, f_y, and difference in electric potential, $\Delta\phi$, of the EE case in (a) and (b) and of EV and EVF in (c) and (d) respectively. Note, that $\Delta\phi$ is the input to the system, whereas f_y is the response.

In figures 4(a) and 4(b) the response of the EE case is shown where a constant force, f_y, is obtained for a given constant load, $\Delta\phi$. The EV results are shown in

figures 4(c) and 4(d) with dashed lines. For the same given constant value of $\Delta\phi$, the force f_y starts at a lower value which increases asymptotically towards the EE response over time. The response from the EVF case is marked with dotted lines in figures 4(c) and 4(d). Naturally, the dotted line in figure 4(c), representing the forces in the EVF case, follows the constant value of the electro-elastic case, while the electric potential in figure 4(d) starts off at a slightly higher value and then gradually decreases to that of the EE case.

4.2 Finite element examples

Dielectric elastomers offer a combination of properties that could be very advantageous compared to traditional materials for a variety of applications, such as tactile displays and optical instruments, see for example Frediani et al. (2014) and Shian et al. (2013). Here, two different DEA types of applications are considered, chosen to represent two important types of inhomogeneous deformation cases. The first simulation involves large pre-stretches and the second involves a bending type state of deformation. Both simulations make use of axi-symmetric Q1P0-elements. The control of either displacement or force is conducted using the same framework as for the example under homogeneous states of deformation, cf. table 3. For the FE simulations a Poisson's ratio of 0.49 is used.

4.2.1 Actuator with pre-stretch

The geometry and boundary conditions treated in Thylander et al. (2016) for a pre-stretch of $\lambda_{pre} = 3$ are used to demonstrate the effect of control in applications involving large pre-stretches. A thin membrane of initial thickness, $h_0 = 1$ mm and radius, $R_0 = 25$ mm is pre-stretched to a radius, $R_1 = 75$ mm. A central inner radius, $r_1 = 7.5$ mm is then coated with compliant electrodes on both sides and loaded electrically. The coated area constitutes the active region of the actuator. A difference in electric potential of $\Delta\phi = 5$ kV is applied to the active area, linearly increasing for 1 second and then kept constant for 60 seconds. The electrically induced increase in the radius of the coated area, $\Delta r = r_2 - r_1$, relaxes the radial tensile force of the passive parts from $f_{r,1}$ to $f_{r,2}$. For this BVP, control with respect to both displacement and force is employed so that adjustments of the electric potential are made with reference to (i) control of the radius of the boundary between the active and passive part of the membrane, Δr and (ii) control of the change in the sum of radial internal forces at the outer boundary of the passive layer, $\Delta f_r = f_{r,2} - f_{r,1}$. These two situations are illustrated in figure 5. The FE mesh consists of 1080 elements, with higher resolution around the boundary between the active and passive parts. Symmetry in the thickness direction allows for simulation of only half the structure. For more details regarding the setup the reader is referred to Thylander et al. (2016). Figure 7 shows the results of the simulated response in terms of displacements, Δr, radial force, Δf_r, and corresponding electric potential, $\Delta\phi$. The EE response, in terms of a constant displacement, force and electric potential, can be seen in figures 7(a)-7(c). The corresponding EV response can be seen in figures 7(d)-7(f), marked with dashed lines.
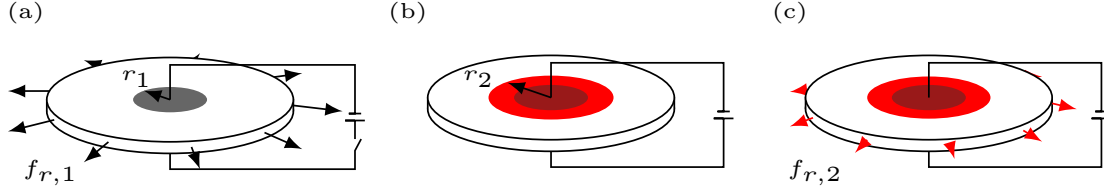
Figure 5: Illustration of setup in FE example with pre-stretch. (a) pre-stretched but not electrically activated setup, (b) displacement control with respect to Δr and (c) force control with respect to Δf_r.

The EV response in terms of displacements and forces starts off at lower values compared to the EE case and then gradually move towards the EE response. The black dotted and black dash-dotted lines in figures 7(d)-7(f) represent the EVD and EVF results respectively. The electric potential in both the EVD and EVF cases, seen in figure 7(f), starts at a larger value than it does in the EE case and then gradually decreases over time. This discrepancy is larger for the EVD case than it is for the EVF case, a tendency that seems consistent with the examples under homogeneous states of deformation. In both control cases, the radial displacement, figure 7(d), and force, figure 7(e), follows the electro-elastic response.
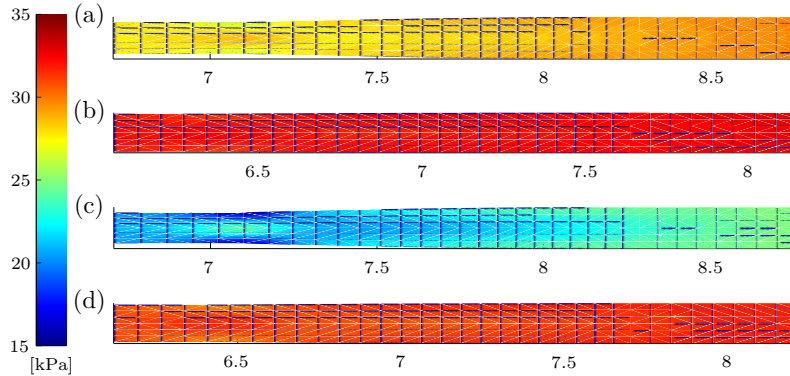
Figure 6: Actuator with pre-stretch: radial total stress, T_{rr}, at $t = 1$ second for the EE, EV, EVD and EVF case in (a), (b), (c) and (d) respectively. Only a small region around the boundary between the active and passive layer is plotted. Dimensions are given in millimetres.

In figure 6 the total radial stress, T_{rr}, for the four cases EE, EV, EVD and EVF at $t = 1$ second are shown. Only a small section of the area at the boundary between the active and passive layers is shown. As expected, and as already indicated in figure 7(d) the radial displacement of the EE case in figure 6(a) and the EVD case in figure 6(c) is conform while the stresses, as also indicated in figure 7(d), are more relaxed from the initial pre-stretched tensile stresses in the EVD case than they are in the EE case. From a comparison between the EE case in figure 6(a) and the EVF case in figure 6(d) it is clear that the radial displacements do not match while the forces in this case corresponds better. Note, that the force is controlled at the outer boundary of the passive part which is not shown in figure 6. The same conclusions can be drawn from figures 7(d) and 7(e).

14
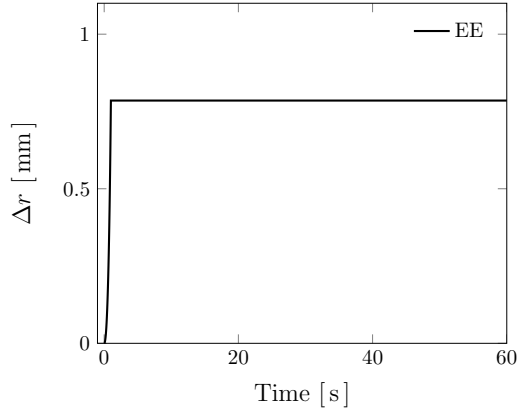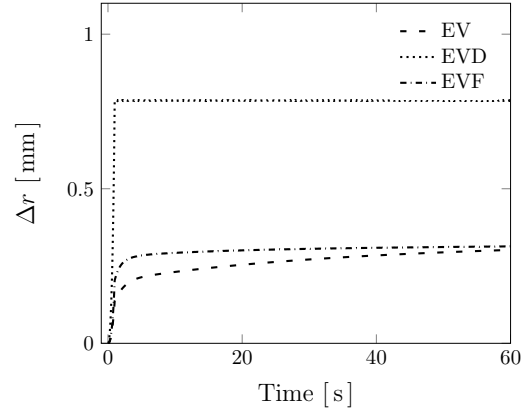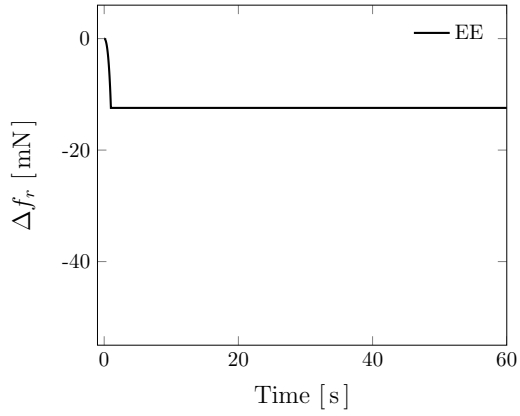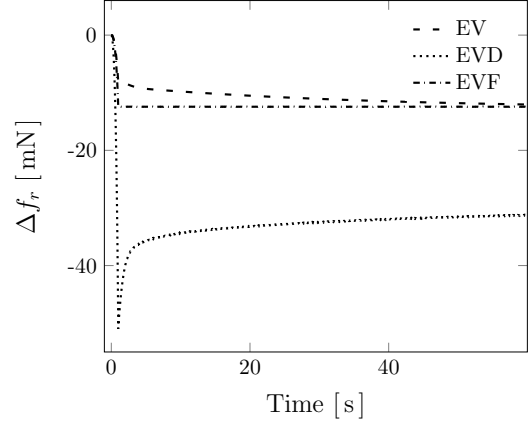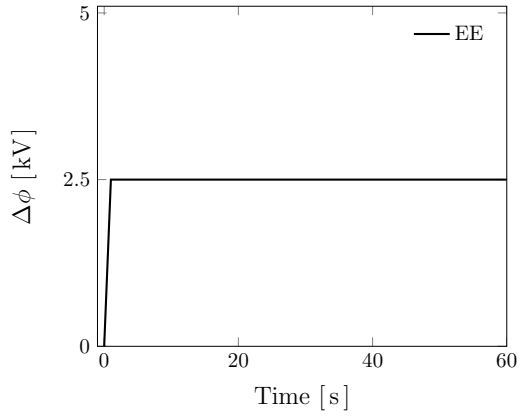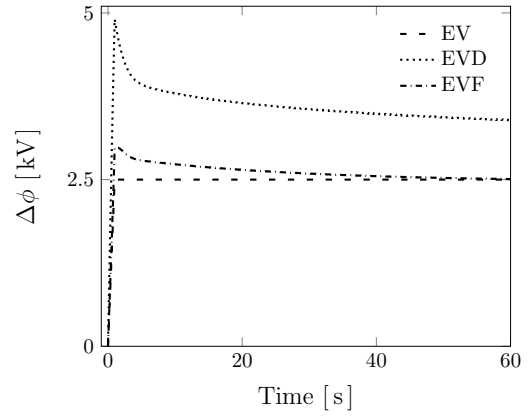
Figure 7: Actuator with pre-stretch: displacement, Δr, change in radial force, Δf_r, and difference in electric potential, $\Delta \phi$, for the EE case in (a), (b) and (c) and for the EV, EVD and EVF cases in (d), (e) and (f) respectively. Note, that $\Delta \phi$ is the input to the simulation whereas Δr and Δf are the responses of the system.

15

4.2.2 Hemisphere-type application

Certain DE applications, including for example loudspeakers, involve hemispherical types of deformation. The geometry and applied load along with boundary conditions chosen for this second FE example give rise to a bending mode which is able to reproduce the overall shape sought in these applications. The specific geometry and boundary conditions chosen to mimic this mode of deformation are illustrated in figure 8. A maximum difference in electric potential, $\Delta\phi$, of 500 V is increased linearly for 0.5 seconds and then kept constant for 60 seconds. Control of the viscous behaviour is performed with respect to the z-displacement of the top central node. The FE mesh consists of 1250 elements, with 10 elements in the thickness direction and equidistantly distributed over the radius.
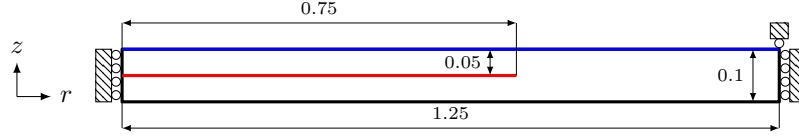
Figure 8: Initial shape of hemisphere-type example. The red line indicates a non-zero electric potential while the blue line indicates zero electric potential. Dimensions are given in millimetres.

The results from the simulations are shown in figures 9-13. In figures 9(a) and 9(b) the constant displacement Δz and the constant electric potential $\Delta\phi$ representing the EE case are shown. The dashed lines in figures 9(c) and 9(d) represent, as before, the EV case and the dotted lines depict the EVD case. The results of the EV and EVD cases follow the same trends as in previous examples with lower initial axial displacements in the EV case and with a dramatically higher initial electric potential in the EVD case. Figure 10 shows the response at $t = 0.5$ seconds, in terms of radial total stress T_{rr} of the EE, EV and EVD cases in (a), (b) and (c) respectively. The overall shape of the EVD case closely matches the EE shape although control with respect to displacement of only one node (central, middle) is considered. Figure 11 shows the corresponding results in terms of axial electric displacement, D_z.

Figures 12 and 13 show the evolution of the radial stress T_{rr} in the EV and EVD cases respectively. The contour plots show the results at $t = 1, 30$ and 60 seconds in (a), (b) and (c) respectively. As expected, the overall level of magnitude of the stresses is higher in the EVD case, shown in figure 13, than in the EV case, shown in figure 12. The level of magnitude of the stresses in the EV case stays roughly the same for the three different levels of deformation in figure 12 while the differences in stress levels are more prominent in the EVD case in figure 13 due to the initial significantly higher electric potential, as also indicated in figure 9(d). After this initial peak, where the stresses are at its highest level, the difference in electric potential gradually decreases generating a very small difference in radial stress between figure 13(b) and figure 13(c).
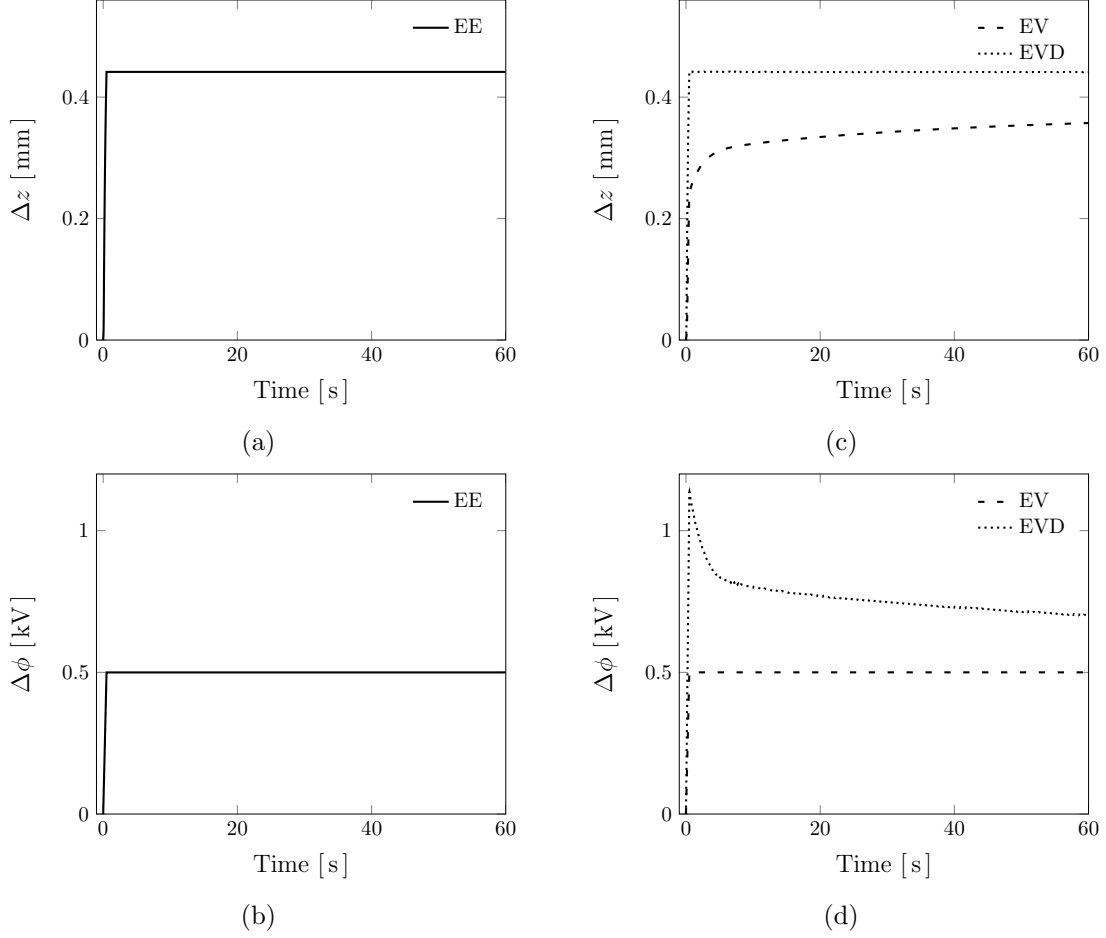
Figure 9: Hemisphere-type application: displacement, Δz, and difference in electric potential, $\Delta\phi$, of the EE case in (a) and (b) and of the EV and EVD in (c) and (d) respectively. Note, that $\Delta\phi$ is the input to the system, whereas Δz is the response.

5 Summary and outlook

A non-affine microsphere model with application to control of viscous effects has been presented. The integration of control with respect to both displacement and force was successfully implemented. The examples under homogeneous states of deformation and finite element examples show similar characteristics. When control with respect to displacement is considered, the change in electric potential is significantly higher compared to when control with respect to force is considered. A sharp drop in electric potential after the load ramp is completed is found in all cases considering control with respect to displacement. In practise, this peak could be smoothed out at the expense of a temporarily larger error during a brief initial period without influencing the overall deformation much. The overall shape of the electro-elastic case in the hemisphere-type application is successfully recaptured in the controlled electro-viscoelastic case although only control of displacement with respect to one single node is considered. With the model used here and with a similar bisection algorithm at hand it is possible to construct a load function that reconstructs a preferred electro-elastic response with

17
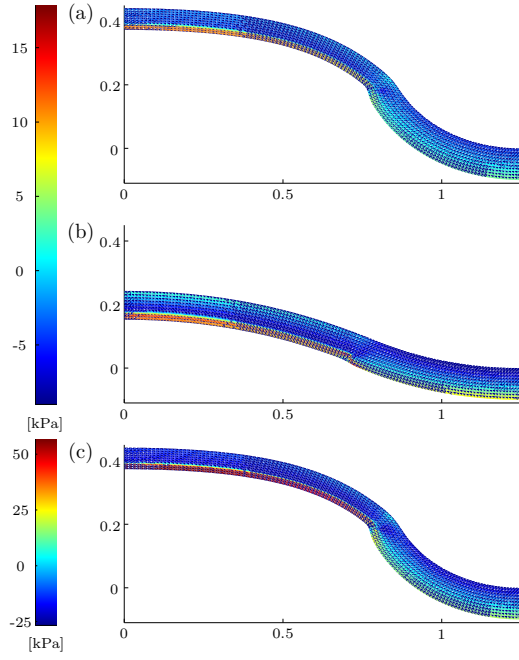
Figure 10: Hemisphere-type application: radial total stress, T_{rr}, at $t = 0.5$ seconds for EE, EV and EVD in (a), (b) and (c) respectively. Dimensions are given in millimetres.
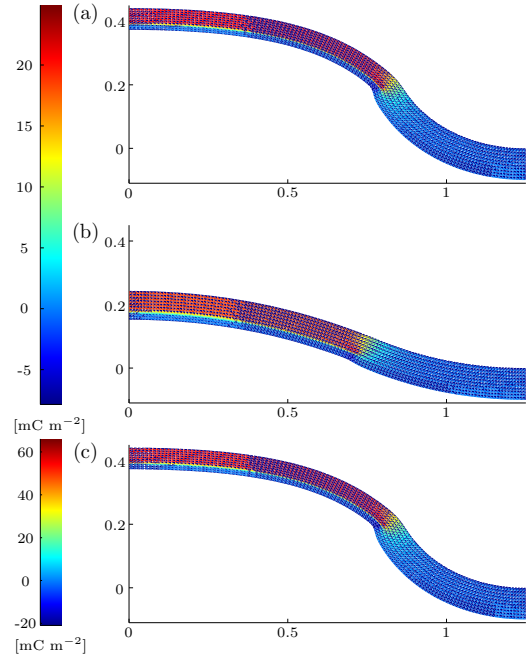
Figure 11: Hemisphere-type application: electric displacement, D_z, at $t = 0.5$ seconds for EE, EV and EVD in (a), (b) and (c) respectively. Dimensions are given in millimetres.
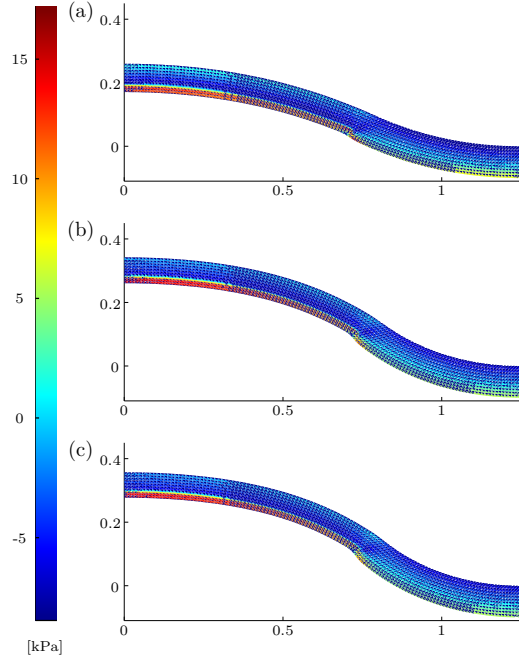

Figure 12: Hemisphere-type application: evolution of radial total stress, T_{rr}, in the EV case for three different time steps. In (a) $t = 1$, (b) $t = 30$ and (c) $t = 60$ seconds. Dimensions are given in millimetres.
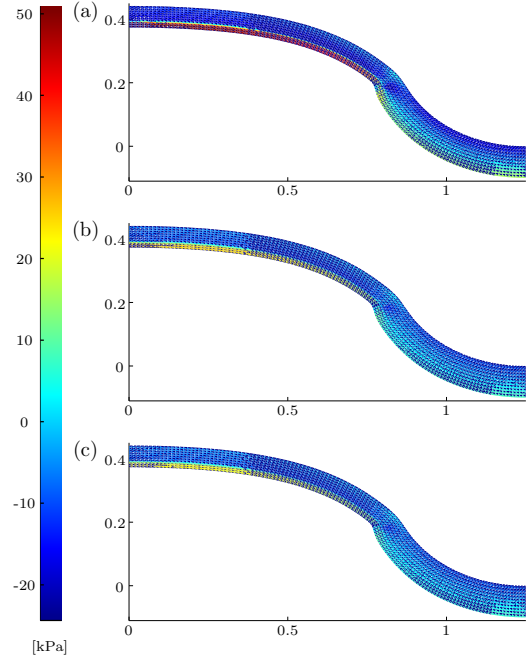
Figure 13: Hemisphere-type application: evolution of radial total stress, T_{rr}, in the EVD case for three different time steps. In (a) $t = 1$, (b) $t = 30$ and (c) $t = 60$ seconds. Dimensions are given in millimetres.

respect to either displacement or force. Future work on enhancements of DE applications includes for example optimised positioning of electrodes, extension to stacked actuators as well as inclusion of inertia effects.

Acknowledgements

References

Ask, A., Menzel, A., Ristinmaa, M., 2012a. Electrostriction in electro-viscoelastic polymers. Mech. Mater. 50, 9–21.

Ask, A., Menzel, A., Ristinmaa, M., 2012b. Phenomenological modeling of viscous electrostrictive polymers. Int. J. Non-Linear Mech. 47 (2), 156–165.

Bažant, Z. P., Oh, B. H., 1986. Efficient numerical integration on the surface of a sphere. Z. Angew. Math. Mech. 66 (1), 37–49.

Blum, M., Büeler, M., Grätzel, C., Giger, J., Aschwanden, M., 2012. Optotune focus tunable lenses and laser speckle reduction based on electroactive polymers. Proc. SPIE 8252, 825207–825207–11.

Bortot, E., Denzer, R., Menzel, A., Gei, M., 2016. Analysis of viscoelastic soft dielectric elastomer generators operating in an electrical circuit. Int. J. Solids Struct. 78–79, 205–215.

Büschel, A., Klinkel, S., Wagner, W., 2013. Dielectric elastomers – numerical modeling of nonlinear visco-electroelasticity. Int. J. Numer. Methods Engng 93 (8), 834–856.

Carol, I., Jirásek, M., Bažant, Z. P., 2004. A framework for microplane models at large strain, with application to hyperelasticity. Int. J. Solids Struct. 41 (2), 511–557.

Carpi, F., Anderson, I., Bauer, S., Frediani, G., Gallone, G., Gei, M., Graaf, C., Jean-Mistral, C., Kaal, W., Kofod, G., Kollosche, M., Kornbluh, R., Lassen, B., Matysek, M., Michel, S., Nowak, S., O'Brien, B., Pei, Q., Pelrine, R., Rechenbach, B., Rosset, S., Shea, H., 2015. Standards for dielectric elastomer transducers. Smart Mater. Struct. 24 (10), 105025.

Carpi, F., Frediani, G., Rossi, D. D., June 2012. Electroactive elastomeric actuators for biomedical and bioinspired systems. In: 2012 4th IEEE RAS EMBS International Conference on Biomedical Robotics and Biomechatronics (BioRob). pp. 623–627.

Carpi, F., Frediani, G., Tarantino, S., De Rossi, D., 2010. Millimetre-scale bubble-like dielectric elastomer actuators. Polym. Int. 59 (3), 407–414.

Carpi, F., Frediani, G., Turco, S., De Rossi, D., 2011a. Bioinspired tunable lens with muscle-like electroactive elastomers. Adv. Func. Mater. 21 (21), 4152–4158.

Carpi, F., Kornbluh, R., Sommer-Larsen, P., Alici, G., 2011b. Electroactive polymer actuators as artificial muscles: are they ready for bioinspired applications? Bioinsp. Biomim 6 (4), 045006.

Chiang Foo, C., Cai, S., Jin Adrian Koh, S., Bauer, S., Suo, Z., 2012. Model of dissipative dielectric elastomers. J. Appl. Phys. 111 (3), 034102.

Chiba, S., Waki, M., Wada, T., Hirakawa, Y., Masuda, K., Ikoma, T., 2013. Consistent ocean wave energy harvesting using electroactive polymer (dielectric elastomer) artificial muscle generators. Appl. Energ. 104, 497–502.

Denzer, R., Menzel, A., 2014. Configurational forces for quasi-incompressible large strain electro-viscoelasticity – Application to fracture mechanics. Eur. J. Mech. A-Solids 48, 3–15.

Dorfmann, A., Ogden, R. W., 2005. Nonlinear electroelasticity. Acta Mech. 174 (3), 167–183.

Frediani, G., Mazzei, D., De Rossi, D. E., Carpi, F., 2014. Wearable wireless tactile display for virtual interactions with soft bodies. Front. Bioeng. Biotechnol. 2 (31).

Graf, C., Maas, J., 2012. Acoustic transducer based on dielectric elastomers. Proc. SPIE 8340, 83401G–83401G–11.

Heydt, R., Kornbluh, R., Eckerle, J., Pelrine, R., 2006. Sound radiation properties of dielectric elastomer electroactive polymer loudspeakers. Proc. SPIE 6168, 61681M–61681M–8.

Hosoya, N., Baba, S., Maeda, S., 2015. Hemispherical breathing mode speaker using a dielectric elastomer actuator. J. Acoust. Soc. Am. 138 (4), EL424–EL428.

Kollosche, M., Kofod, G., Suo, Z., Zhu, J., 2015. Temporal evolution and instability in a viscoelastic dielectric elastomer. J. Mech. Phys. Solids 76, 47–64.

Kornbluh, R. D., Pelrine, R., Prahlad, H., Wong-Foy, A., McCoy, B., Kim, S., Eckerle, J., Low, T., 2011. From boots to buoys: promises and challenges of dielectric elastomer energy harvesting. Proc. SPIE 7976, 797605–797605–19.

Kovetz, A., 2000. Electromagnetic Theory. Oxford University Press.

Linder, C., Tkachuk, M., Miehe, C., 2011. A micromechanically motivated diffusion-based transient network model and its incorporation into finite rubber viscoelasticity. J. Mech. Phys. Solids 59 (10), 2134–2156.

Loverich, J. J., Kanno, I., Kotera, H., 2006. Concepts for a new class of all-polymer micropumps. Lab Chip 6, 1147–1154.

Maugin, G. A., 1988. Continuum Mechanics of Electromagnetic Solids. Vol. 33 of Applied Mathematics and Mechanics. North-Holland.

Michel, S., Zhang, X. Q., Wissler, M., Löwe, C., Kovacs, G., 2010. A comparison between silicone and acrylic elastomers as dielectric materials in electroactive polymer actuators. Polym. Int. 59 (3), 391–399.

Miehe, C., Göktepe, S., 2005. A micro–macro approach to rubber-like materials. Part II: The micro-sphere model of finite rubber viscoelasticity. J. Mech. Phys. Solids 53 (10), 2231–2258.

Miehe, C., Göktepe, S., Lulei, F., 2004. A micro-macro approach to rubber-like materials—Part I: the non-affine micro-sphere model of rubber elasticity. J. Mech. Phys. Solids 52 (11), 2617–2660.

Miles, P., Hays, M., Smith, R., Oates, W., 2015. Bayesian uncertainty analysis of finite deformation viscoelasticity. Mech. Mater. 91, Part 1, 35–49.

Ogden, R. W., 1997. Non-linear Elastic Deformations. Dover.

Park, H. S., Nguyen, T. D., 2013. Viscoelastic effects on electromechanical instabilities in dielectric elastomers. Soft Matter 9, 1031–1042.

Ren, Z., Niu, X., Chen, D., Hu, W., Pei, Q., 2014. A new bistable electroactive polymer for prolonged cycle lifetime of refreshable Braille displays. Proc. SPIE 9056, 905621–905621–9.

Romasanta, L. J., Lopez-Manchado, M. A., Verdejo, R., 2015. Increasing the performance of dielectric elastomer actuators: A review from the materials perspective. Prog. Polym. Sci 51, 188–211.

Shian, S., Diebold, R. M., Clarke, D. R., Apr 2013. Tunable lenses using transparent dielectric elastomer actuators. Opt. Express 21 (7), 8669–8676.

Suo, Z., 2010. Theory of dielectric elastomers. Acta Mech. Solida Sinica 23 (6), 549–578.

Thylander, S., Menzel, A., Ristinmaa, M., 2012. An electromechanically coupled micro-sphere framework: application to the finite element analysis of electrostrictive polymers. Smart Mater. Struct. 21 (9), 094008.

Thylander, S., Menzel, A., Ristinmaa, M., 2013. Corrigendum: An electromechanically coupled micro-sphere framework—application to the finite element analysis of electrostrictive polymers. Smart Mater. Struct. 22 (3), 039501.

Thylander, S., Menzel, A., Ristinmaa, M., 2016. A non-affine electro-viscoelastic microsphere model for dielectric elastomers: Application to VHB 4910 based actuators. J. Intel. Mat. Syst. Str.

Zhang, J., Chen, H., Li, B., 2014a. A method of tuning viscoelastic creep in charge-controlled dielectric elastomer actuation. EPL (Europhysics Letters) 108 (5), 57002.

Zhang, J., Chen, H., Li, B., McCoul, D., Pei, Q., 2015. Coupled nonlinear oscillation and stability evolution of viscoelastic dielectric elastomers. Soft Matter 11, 7483–7493.

Zhang, J., Li, B., Chen, H., Pei, Q., 2016. Dissipative performance of dielectric elastomers under various voltage waveforms. Soft Matter 12, 2348–2356.

Zhang, J., Wang, Y., McCoul, D., Pei, Q., Chen, H., 2014b. Viscoelastic creep elimination in dielectric elastomer actuation by preprogrammed voltage. Appl. Phys. Lett. 105 (21), 212904.

Zhao, X., Koh, S. J. A., Suo, Z., 2011. Nonequilibrium thermodynamics of dielectric elastomers. Int. J. Appl. Mech. 03 (02), 203–217.

Paper D

S. Thylander, A. Menzel, M. Ristinmaa, S. Hall and J. Engqvist

Measurements of the electro-viscoelastic response of an acrylic elastomer using three-dimensional surface digital image correlation

Measurements of the electro-viscoelastic response of an acrylic elastomer using three-dimensional surface digital image correlation

Sara Thylander[a], Andreas Menzel[a,b], Matti Ristinmaa[a],
Stephen Hall[a] and Jonas Engqvist[a]

[a] Division of Solid Mechanics, Lund University
P.O. Box 118, S-221 00 Lund, Sweden

[b] Department of Mechanical Engineering, Institute of Mechanics, TU Dortmund
Leonhard-Euler-Str. 5, D-44227 Dortmund, Germany

Abstract

Experimental investigations are carried out with respect to the electromechanically coupled and time-dependent behaviour of an acrylic elastomer, namely VHB 4910. For the electromechanically coupled experiments different biaxial pre-stretches are considered and full-field measurements are made using three-dimensional surface digital image correlation. Both equi-biaxial and non equi-biaxial pre-stretches are investigated. The experimental data acquired are intended to be used for better understanding of the complex material behaviour found in VHB 4910 as well as for calibration and improvement of existing constitutive models. Special emphasis lies on measurements of the thickness change of biaxially pre-stretched specimens as it plays a critical role in view of electromechanical instabilities. For completeness, cyclic uniaxial tests of the purely mechanical response are performed and compared to similar experiments found in the literature.

1

1 Introduction

Dielectric elastomers (DEs) represent a subset of electroactive polymers characterised by a low elastic modulus with the ability to achieve very large actuated strains. Acrylic- and silicone-based DEs are the most widely used materials in dielectric elastomer actuators (DEAs) due to their high specific energy as well as large and relatively fast actuation response; see Carpi et al. (2011b) and Kornbluh et al. (2000). The main DEA configuration consists of a thin elastomer sandwiched between two compliant electrodes. Under the application of an electric field the two electrodes will attract each other due to accumulated opposing charges on the surfaces of the electrodes. This so-called Maxwell effect, leads to a local decrease of the thickness and an associated increase, due to (quasi) incompressibility of the elastomer, of the in-plane area perpendicular to the electric field. To decrease the elastomer thickness, avoid wrinkling, due to compressive in-plane loading during actuation, and ultimately to avoid electrical breakdown, the elastomer is often pre-stretched before being electrically activated. The material behaviour of dielectric elastomers is complex and involves electromechanical coupling, finite deformations, time-dependent mechanical and electrical responses and electromechanical instabilities.

VHB 4910 is an acrylic-based elastomer and a popular candidate for DEA applications. The elastomer is characterised as a very soft polymer with a highly non-linear elastic and viscoelastic response, a relatively high dielectric constant and can give actuated areal strains greater than 100%, see e.g. Pelrine et al. (2000). VHB is used as electromechanical transducers in a variety of applications such as: loudspeakers, see Graf and Maas (2012) and Hosoya et al. (2015); tunable lenses, see Carpi et al. (2011a), Blum et al. (2012) and Shian et al. (2013); and energy harvesting devices, see Kornbluh et al. (2011) and Chiba et al. (2013) amongst others. Due to its popularity, a considerable amount of experimental investigations have been performed on VHB 4910. Recent studies include the analysis of the quasi-static and viscoelastic behaviour, see eg. Hossain et al. (2012) and Sahu and Patra (2016), as well as of the quasi-static and electro-viscoelastic behaviour, see Hossain et al. (2015), Kollosche et al. (2015) and Jiang et al. (2015).

One topic gaining significant attention in recent literature deals with different modes of instabilities occurring in DEAs, many of which involve inhomogeneous deformations. One of the most common modes investigated is the, so-called, pull-in instability with its associated wrinkle formation and electric breakdown. Pull-in instability causes the membrane in the DEA to drastically reduce its thickness and may eventually lead to electric breakdown. In view of this specific instability, the pre-stretch and corresponding thickness of the dielectric elastomer membrane in an actuator is of great practical importance, as they can both delay or suppress the rapid thinning of the membrane due to higher mechanical stiffness, see for example Pelrine et al. (2000), Kofod et al. (2003), Huang et al. (2012), Zhao and Wang (2014) and Wang et al. (2011). To enhance the reliability and increase the efficiency of existing and potential DEA applications, it is necessary to understand and include these phenomena into constitutive models. Measuring the thickness during loading is, however, not a straightforward task. Furthermore, due to the elastomers' soft nature, the need

for a non-contact measurement technique is apparent, see Carpi et al. (2015). For this purpose we propose the use of three-dimensional surface digital image correlation (DIC) to measure the thickness change during electromechanical testing.

In DIC the displacement field of the surface of a specimen is acquired by correlating pixel subsets in a reference image of the specimen to pixel subsets of images of the specimen in a deformed state. If no natural pattern is present on the sample, a random speckle pattern must first be applied to enable the correlation. By using two cameras, calibrated for stereovision, it is possible to resolve not only the in-plane components, but also the out-of-plane component of the surface deformation field. The use of DIC reveals inhomogeneous deformation behaviour which is not visible when using conventional deformation measurement techniques and is ideal for validation of constitutive models. DIC has been utilized to characterize the material response of a wide range of materials under different loading conditions. With regard to VHB, DIC investigations of the aerodynamic and fluid-structural response can be found in Hays et al. (2013, 2016). To the authors' knowledge, no DIC analysis concerning the electromechanical response of VHB has been published previously.

As most experimental investigations of DEAs tend to focus on the macroscopic deformation, presented in terms of overall or point-wise responses that lack spatial resolution, the objective of this paper is to provide local deformation data for electromechanical loading. To this end, we use the method of DIC to obtain the full surface deformation fields of a VHB-DEA for a range of different biaxial pre-stretches. With the help of the deformation field obtained from the digital image correlation, together with the assumption of incompressibility, it is possible to investigate the thickness change during electrical loading. For completeness, we also consider the purely mechanical, time-dependent response using uniaxial cyclic tests and compare our results to similar investigations found in the literature.

2   Experiments

Both purely viscoelastic and the coupled electro-viscoelastic behaviours of VHB 4910 are investigated. First, the viscoelastic properties are analysed using standard uniaxial tests at different strain rates with measurements of the macroscopic stress-strain relation. Secondly, the electro-viscoelastic behaviour of biaxially pre-stretched VHB membranes is analysed by using three-dimensional surface DIC. All experiments were carried out at room temperature.

2.1   Material

The material used in the experiments is the commercial elastomer VHB 4910 manufactured by 3M. The material is capable of dealing with very large strains and is characterised as an acrylic elastomer. Mechanical and dielectric properties of VHB 4910 are listed in Biggs et al. (2013). The specimens were cut to desired size from three different roll sizes, all with a thickness of 1 mm.

2.2 Visco-elastic response

A VHB 4910 membrane, of initial cross section of 25×1 mm and gauge length of 50 mm^2 is subjected to a displacement controlled, uniaxial cyclic loading path according to figure 1. To avoid compressive stresses, the displacements are cycled around 50 % of the maximum stretch. Three different stretch rates, namely $\dot\lambda \in [5 \cdot 10^{-4}, 0.01, 0.05]$, and two different maximum stretch levels, $\lambda_{max} \in [1.5, 3]$, resulting in six different combinations, are investigated. The stretch rate and maximum stretch levels are chosen in order to enable a comparison with results from Hossain et al. (2012) and Sahu and Patra (2016). Also, as indicated in figure 1, ten cycles are performed for each combination. The specimens are tested using a MTS hydraulic loading frame. Displacement and speed are controlled by an Instron 8500 control system. The force is measured with a U9C force transducer (Hottinger Baldwin Messtechnik) calibrated to 100 N. Force and displacement are recorded using the software LabView. Each specimen is fixed in custom-built grips and placed in the tensile machine, see figure 2.
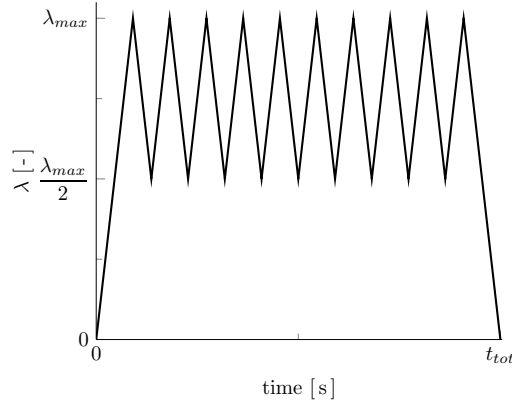
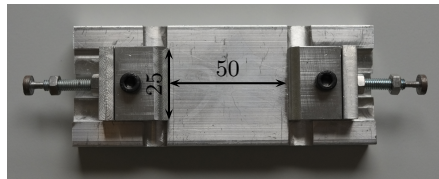**Figure 1:** Sketch of the applied load path used for uniaxial cyclic tests.

Figure 2: Picture of grips and holder used for uniaxial cyclic tests. Dimensions are given in millimetres.

The results from the uniaxial cyclic tests are shown in figures 3(a)-(f). Figures 3(a), (c) and (e) show the nominal stress vs. stretch for the three stretch rates used and for both maximum stretch levels. Figures 3(b), (d) and (f) show the effect of stress softening during cyclic loading for the respective stretch rates and maximum stretch levels. The nominal stress in axial direction follow from the assumption of a homogeneous state of deformation as force per initial cross sectional area.
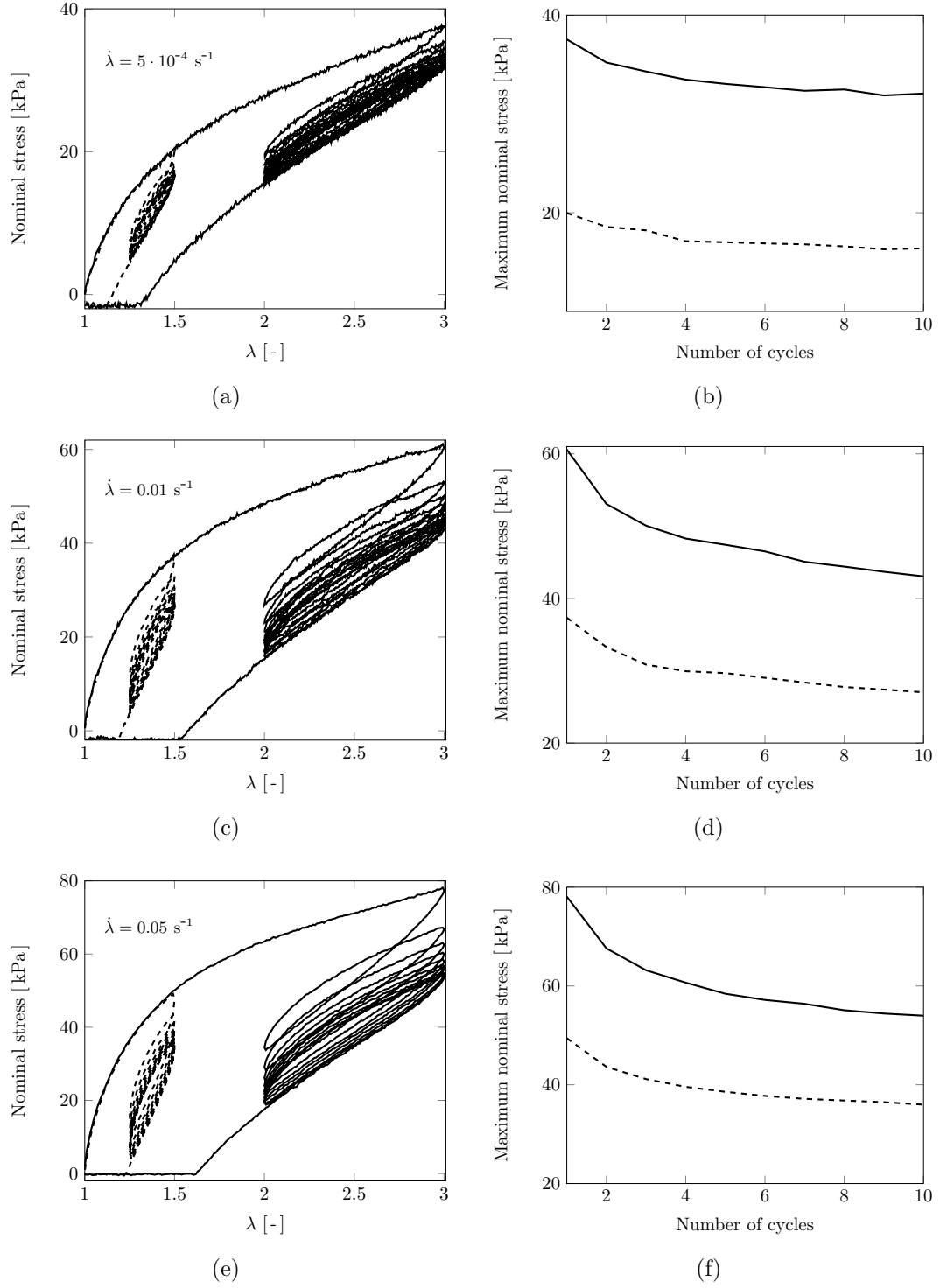
4

Figure 3: Uniaxial cyclic tests where figures (a), (c) and (e) reveal the stress-stretch relation and (b), (d) and (f) show the effect of stress softening during cyclic loading.

The results from two experimental studies, i.e. Hossain et al. (2012) and Sahu and Patra (2016), of the mechanical response of VHB 4910 are reproduced here for comparison purposes. Both articles involve several uniaxial investigations, but only those comparable to the tests performed in this work are selected. The reproduced graphs can be seen in figures 4(a)-(b) and 5(a)-(b). Figure 4 shows the loading and un-loading curves for two different strain rates, namely $\dot{\varepsilon} = 0.05$ and $\dot{\varepsilon} = 0.01$ s^{-1}, at two different maximum stretch levels, i.e. $\lambda_{max} = 1.5$ and $\lambda_{max} = 3$. In figure 5(a) the relation between stress and stretch from the first and last cycle of a cyclic tensile test is shown. The specific response considers a strain rate of $\dot{\varepsilon} = 0.05$ s^{-1} and a maximum stretch level of $\lambda_{max} = 4$. In figure 5(b) stress softening during seven cycles is presented.
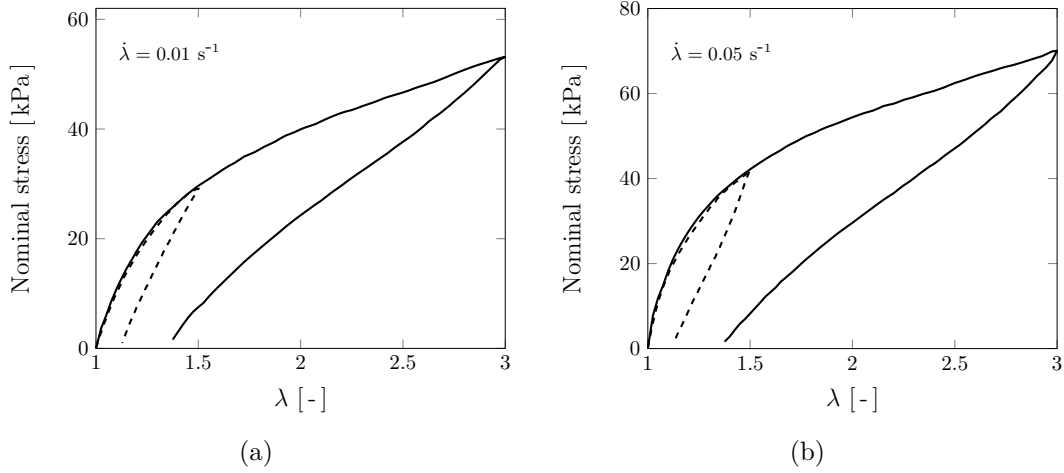

Figure 4: Loading and un-loading curves reproduced from Hossain et al. (2012).
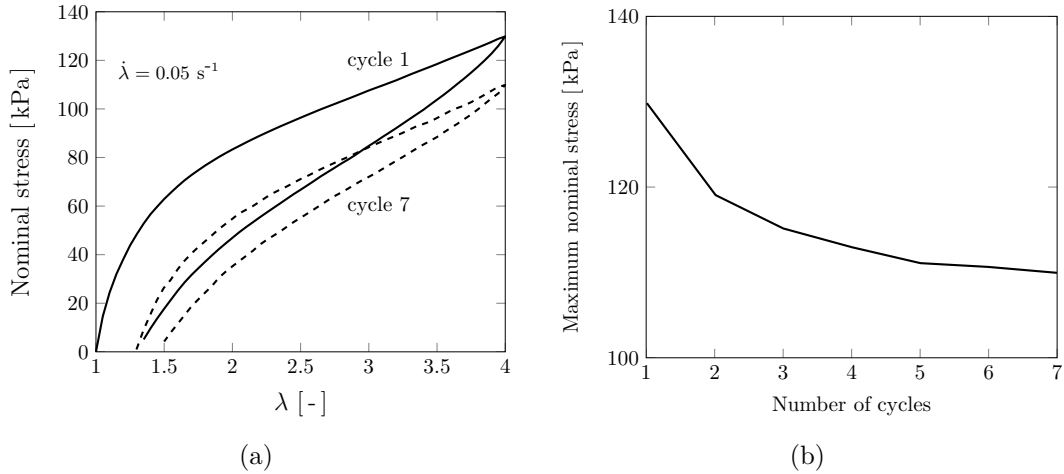

Figure 5: Cyclic loading and un-loading curves reproduced from Sahu and Patra (2016).

The cyclic test results shown in figures 3(a), (c) and (e) reveal clear hysteresis behaviour, which, as expected, is larger for increasing strain rates. From figures 3(b),

(d) and (f) the effect of stress softening is apparent. However, after ten cycles, the maximum stress is rather stable, in line with results reported in Sahu and Patra (2016). As with hysteresis, this stress softening effect is larger and more pronounced for higher strain rates. Both phenomena are strong indicators of a history dependency and it is crucial to take them into account when designing applications. The comparison between figures 3(c) and 4(a), as well as between figures 3(e), 4(b) and 5(a), reveals some differences in stress magnitude. The recorded levels of stress from Sahu and Patra (2016) are consistently highest and results from Hossain et al. (2012) are consistently at the lowest stress levels. Experiments performed in this paper fall in between, in terms of stress level.

2.3 Electro-viscoelastic response

The electro-viscoelastic behaviour of VHB 4910 is investigated using biaxially pre-stretched circular actuators. The specimens are first manually pre-stretched in a custom built device, see pictures in figure 6, and then fixed in a circular frame with radius $r_f = 75$ mm. A central circular area with radius $r_e = 7.5$ mm on both sides of the elastomer is then coated with a graphite powder to act as compliant electrodes. To connect the electrodes to the voltage supply, thin lines of graphite powder are applied from the center outwards to the edge of the specimen. Copper tape is attached to the frame and connected to the thin lines of graphite powder with a mixture of carbon grease and carbon black particles. Three different pre-stretch ratios are investigated, i) $\lambda_x \times \lambda_y = 2 \times 2$, ii) $\lambda_x \times \lambda_y = 1.5 \times 1.5$ and iii) $\lambda_x \times \lambda_y = 1.5 \times 2$. The different stretch ratios are established by drawing a circle, or ellipse respectively for the non-equibiaxial pre-stretch, with radius $r_i = r_f/\lambda_i$, where $i \in [x, y]$, onto the un-stretched specimen. The specimen is then stretched so that the circle, or ellipse respectively, obtained the radius of the plastic frame and $r = r_f$, cf. figures 7(a) and 7(b). Note, that two different configurations of the pre-stretch device have been used. For the equi-biaxial tests six arms are used while for the non equi-biaxial tests only four arms are used, see figures 6(a) and 6(b) respectively.

Before actuation of the initially transparent VHB elastomer, a random speckle pattern is applied to the entire surface of the specimen, including the frame, with a white, water-based spray-paint to enable image correlation during the experiment. The entire sample is then placed on a black background to further distinguish the speckle pattern, see figure 7(a). A maximum of 5000 V is applied to the specimen, ramped up in two steps during a total of 0,5 seconds. The voltage is then kept constant for 15000 seconds, see figure 8.

2.4 Digital image correlation

The displacements in the pre-stretched elastomer actuator, caused by the application of the electric field, are measured using three-dimensional surface digital image correlation. The images are recorded using two Prosilica GT6600 29-Megapixel digital cameras from Allied Vision Technologies throughout each test. Before each test the cameras are calibrated for stereo-vision using the commercial software Vic-3D from
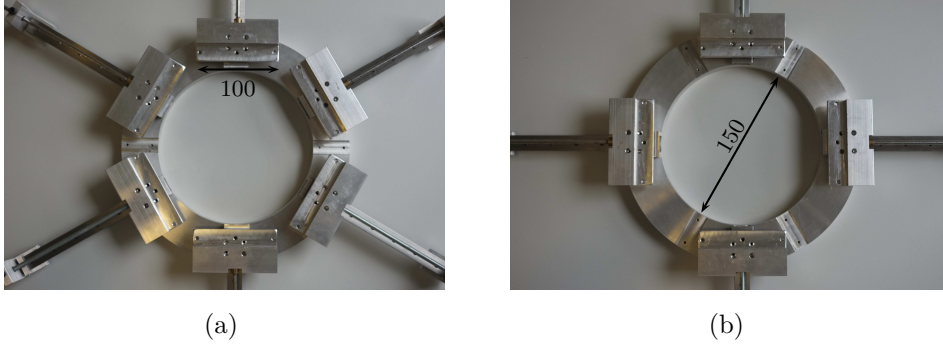
Figure 6: Picture of custom built device used for pre-stretching the membranes for equi-biaxial tests in 6(a) and for non equi-biaxial tests in 6(b). Dimensions are given in millimetres.
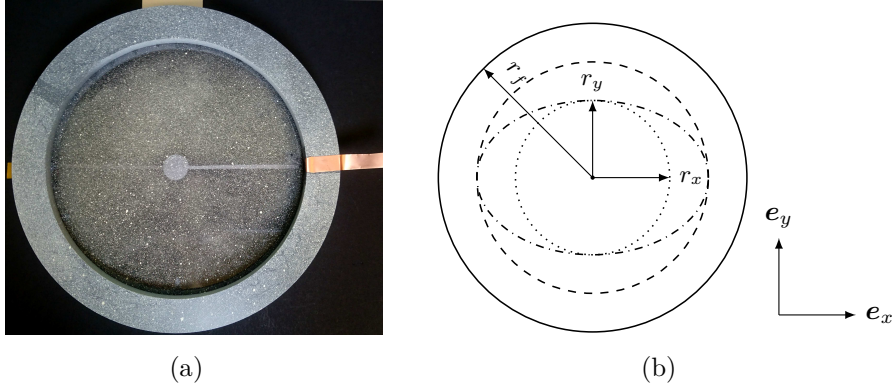

Figure 7: Picture of pre-stretched sample in frame including applied electrode and speckle pattern in 7(a) and sketch of initial radii used for control of pre-stretch in 7(b). The dotted circle in 7(b) represent $\lambda_x \times \lambda_y = 2 \times 2$, the dashed represent $\lambda_x \times \lambda_y = 1.5 \times 1.5$ and the dash-dotted circle represents $\lambda_x \times \lambda_y = 1.5 \times 2$.

Correlated Solutions, enabling the analysis of both in-plane and out-of-plane deformation. The calibration is performed with a reference grid image placed at different positions and at different angles, for more details see Correlated Solutions (2010). The maximum calibration error, defined as the standard deviation between the measured position of the reference grid points and the theoretical position of the reference grid points, is 0.062 pixels.

The correlation between each image is made using VIC 3D with the correlation window and step sizes of 37×37 and 7 pixels, respectively. With an image pixel size of approximately 44 µm, a physical DIC correlation window size of approximately 1.63×1.63 mm^2 is obtained. During the experiments the cameras are set up to take images at a fixed time interval. The pixel subset of each image of the actuated sample was correlated with the corresponding subset of an initial, undeformed reference image. The acquired displacement fields were used to calculate the displacement gradient and full-field strain using an in-house developed code in Matlab. The three unknown terms of the deformation gradient gradient, i.e. $\frac{\partial x}{\partial Z}$, $\frac{\partial y}{\partial Z}$ and $\frac{\partial z}{\partial Z}$, are calculated using the
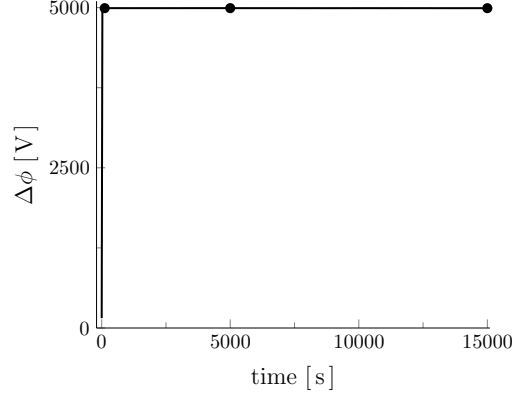
Figure 8: Sketch of applied load path used for biaxial tests.

assumptions of homogeneous deformation through the thickness and incompressibility such that

$$\frac{\partial x}{\partial Z} = \frac{\partial y}{\partial Z} = 0 \quad \text{and} \quad \frac{\partial z}{\partial Z} = \det^{-1}\left(\begin{bmatrix} \dfrac{\partial x}{\partial X} & \dfrac{\partial x}{\partial Y} \\ \dfrac{\partial y}{\partial X} & \dfrac{\partial y}{\partial Y} \end{bmatrix}\right). \tag{1}$$

The corresponding strains are calculated using the closest neighbour points on a regular 7 pixel grid.

The DIC results are shown in contour plots of principal stretches at three representative time steps, marked with dots in figure 8, and as radial profiles. Furthermore, the displacement of the boundary of the electrode is tracked in the two in-plane directions (x- and y-direction) during loading. Note, that the stretches presented here represent only the part of the deformation gradient caused by activation of the electric field and do not include the initial pre-stretch. Therefore $\boldsymbol{F}_{tot} = \boldsymbol{F}_{act} \cdot \boldsymbol{F}_{ini}$, where $\boldsymbol{F}_{act}$ is the deformation caused by the electric field and $\boldsymbol{F}_{ini}$ is the initial deformation caused by the pre-stretch,

$$\begin{aligned} \boldsymbol{F}_{act} &= \lambda_1 \boldsymbol{e}_1 \otimes \boldsymbol{e}_1 + \lambda_2 \boldsymbol{e}_2 \otimes \boldsymbol{e}_2 + \frac{1}{\lambda_1 \lambda_2} \boldsymbol{e}_3 \otimes \boldsymbol{e}_3 \,, \\ \boldsymbol{F}_{ini} &= \lambda_x \boldsymbol{e}_x \otimes \boldsymbol{e}_x + \lambda_y \boldsymbol{e}_y \otimes \boldsymbol{e}_y + \frac{1}{\lambda_x \lambda_y} \boldsymbol{e}_z \otimes \boldsymbol{e}_z \,, \end{aligned} \tag{2}$$

where λ_i, $i \in [1, 2, 3]$, denotes the principal stretch to the corresponding principal direction $\boldsymbol{e}_i$.

The principal stretches λ_1, λ_2 and λ_3 can be seen as contour plots in figures 9, 11 and 13. For the in-plane stretches, λ_1 and λ_2, the principal directions are also plotted. Averaged radial profiles of the principal stretches can be seen in figures 10, 12 and 14. For the non equi-biaxial pre-stretch, radial profiles in both x- and y-directions are shown. The radial profiles are extracted by averaging the displacements in an angular section of $\pm 10°$ along the x- and y-directions. Figure 15 shows the growth of the electrode radius for the respective pre-stretches. In these figures, growth in both x- and y-directions is plotted for each case.
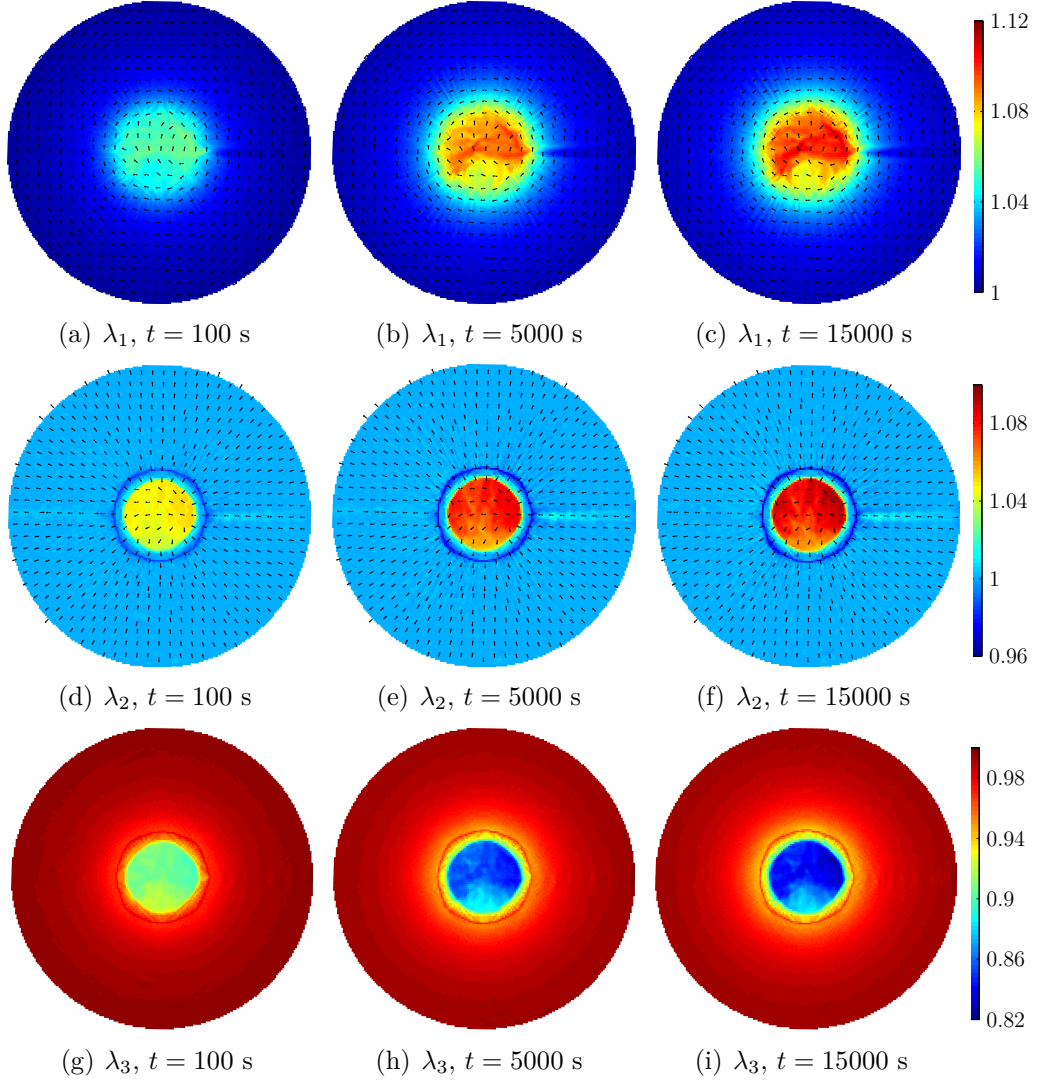
9

Figure 9: Initial equi-biaxial stretch $\lambda_x \times \lambda_y = 2 \times 2$: principal stretch contour plots at three different time steps. Arrows in the two top rows indicate corresponding principal directions. Note, that for better visualization only a radius of 30 mm is plotted.
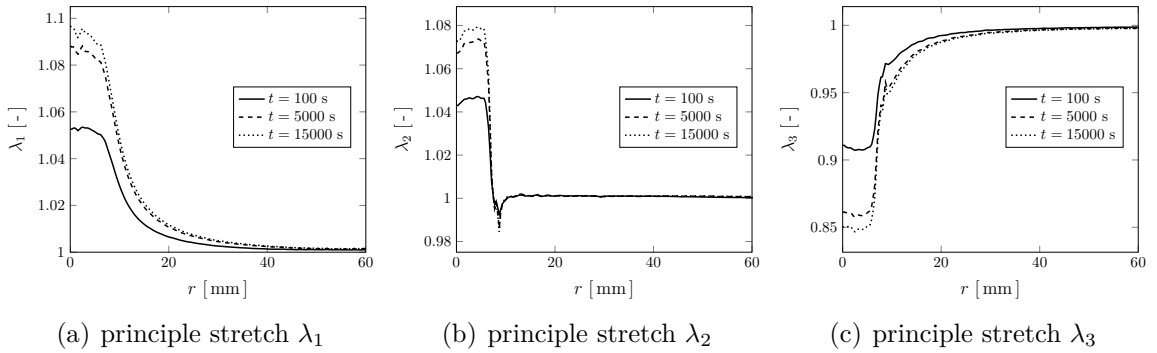

Figure 10: Initial equi-biaxial stretch $\lambda_x \times \lambda_y = 2 \times 2$: radial profiles of principal stretch as a function of distance r from the center. All profiles are calculated from azimuthal averages.

10

(a) λ_1, $t = 100$ s   (b) λ_1, $t = 5000$ s   (c) λ_1, $t = 15000$ s

(d) λ_2, $t = 100$ s   (e) λ_2, $t = 5000$ s   (f) λ_2, $t = 15000$ s

(g) λ_3, $t = 100$ s   (h) λ_3, $t = 5000$ s   (i) λ_3, $t = 15000$ s
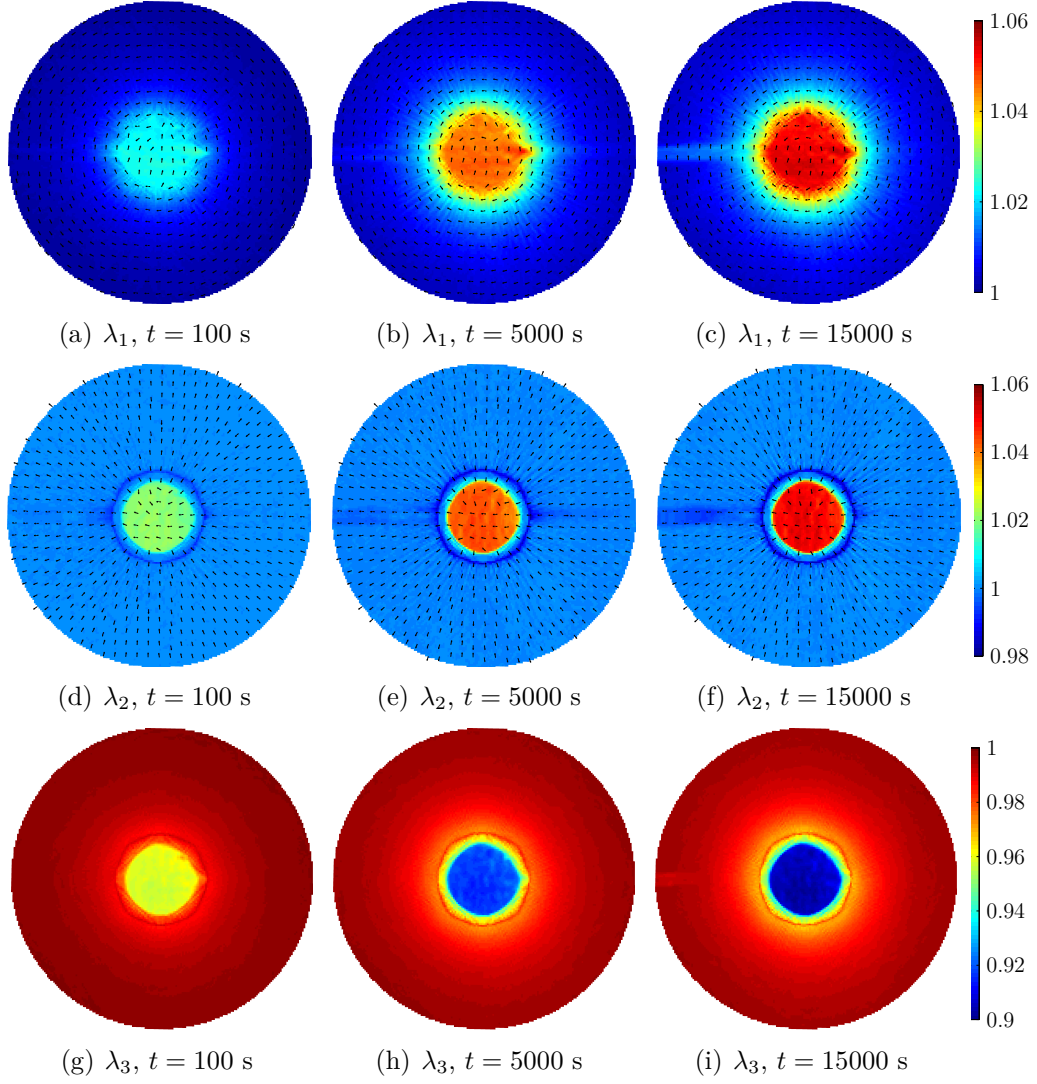
Figure 11: Initial equi-biaxial stretch $\lambda_x \times \lambda_y = 1.5 \times 1.5$: principal stretch contour plots at three different time steps. Arrows in the two top rows indicate corresponding principal directions. Note, that for better visualization only a radius of 30 mm is plotted.
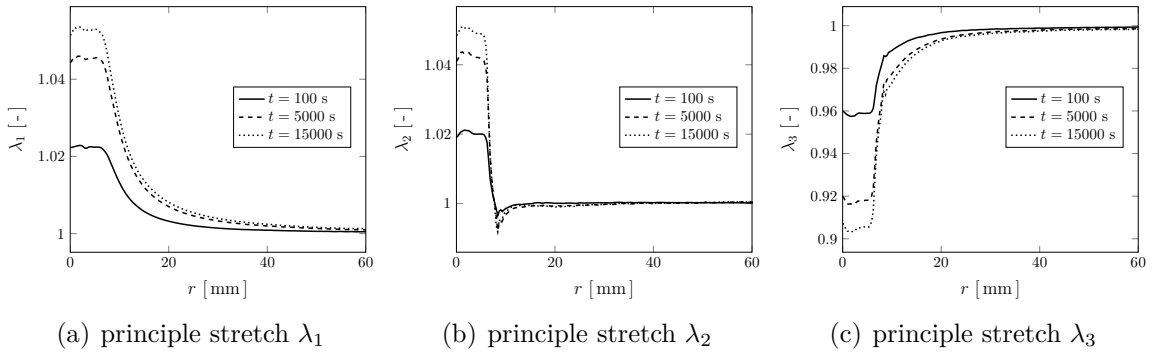

(a) principle stretch λ_1 (b) principle stretch λ_2 (c) principle stretch λ_3

Figure 12: Initial equi-biaxial stretch $\lambda_x \times \lambda_y = 1.5 \times 1.5$: radial profiles of principal stretch as a function of distance r from the center. All profiles are calculated from azimuthal averages.

11

(a) λ_1, $t = 100$ s   (b) λ_1, $t = 5000$ s   (c) λ_1, $t = 15000$ s

(d) λ_2, $t = 100$ s   (e) λ_2, $t = 5000$ s   (f) λ_2, $t = 15000$ s

(g) λ_3, $t = 100$ s   (h) λ_3, $t = 5000$ s   (i) λ_3, $t = 15000$ s
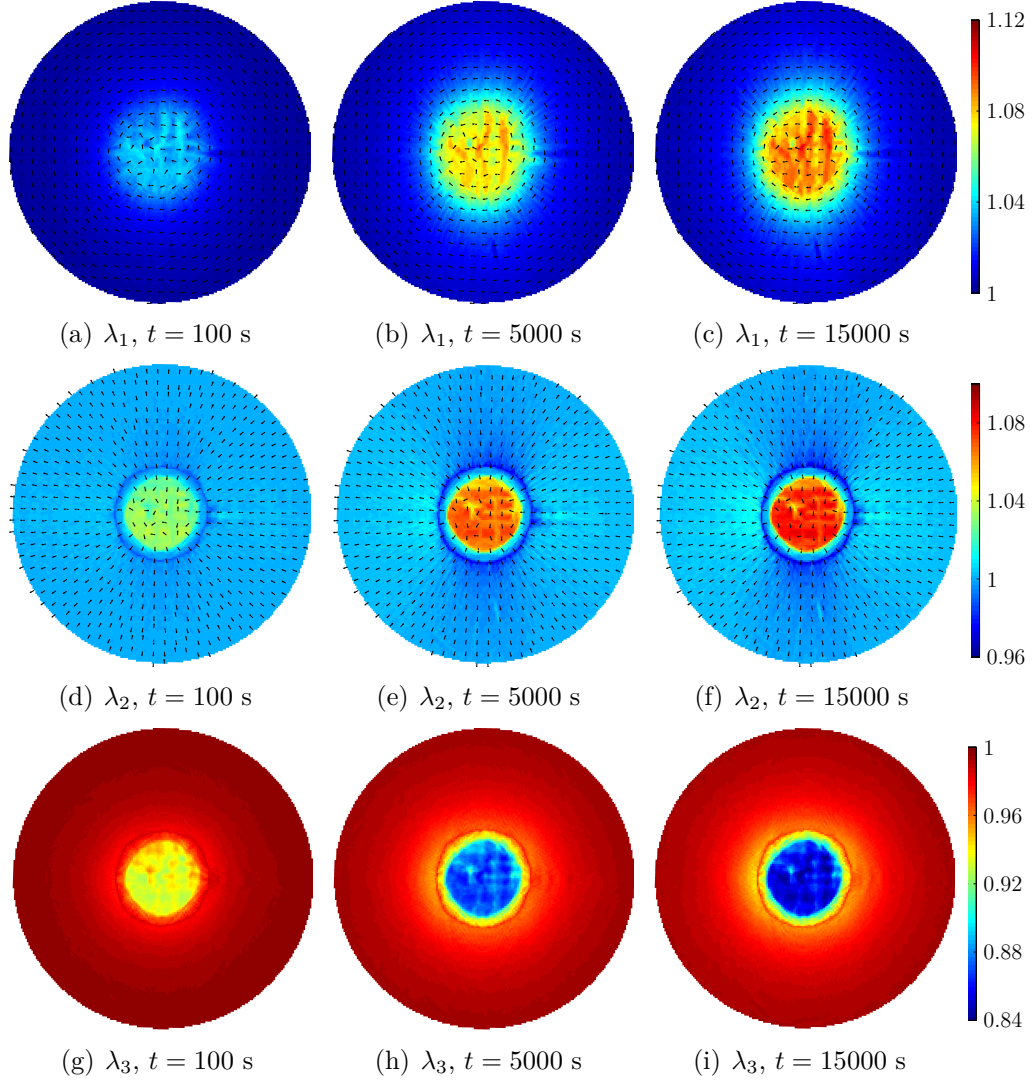
Figure 13: Initial non equi-biaxial stretch $\lambda_x \times \lambda_y = 1.5 \times 2$: principal stretch contour plots at three different time steps. Arrows in the two top rows indicate corresponding principal directions. Note, that for better visualization only a radius of 30 mm is plotted.
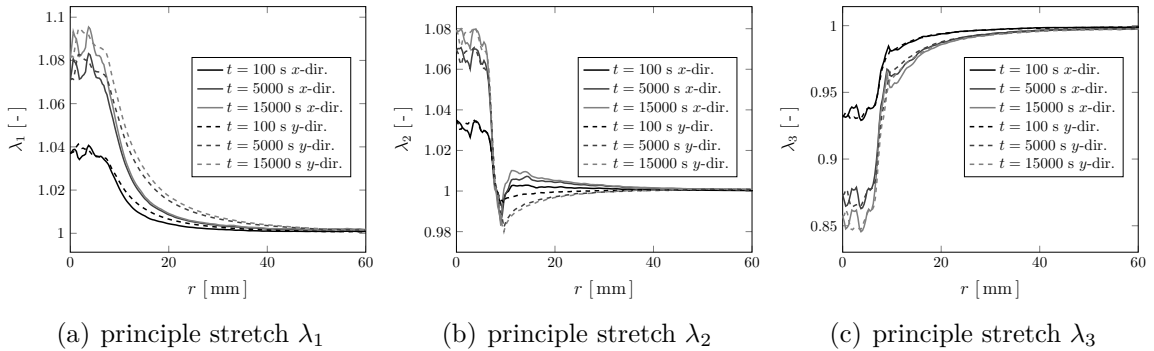

(a) principle stretch λ_1 (b) principle stretch λ_2 (c) principle stretch λ_3

Figure 14: Initial non equi-biaxial stretch $\lambda_x \times \lambda_y = 1.5 \times 2$: radial profiles of principal stretch as a function of distance r from the center. All profiles are calculated from azimuthal averages.
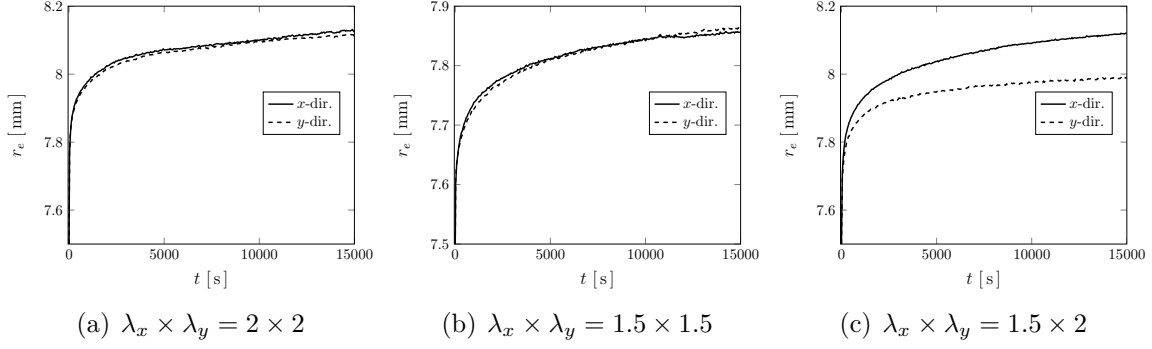
12

(a) $\lambda_x \times \lambda_y = 2 \times 2$ (b) $\lambda_x \times \lambda_y = 1.5 \times 1.5$ (c) $\lambda_x \times \lambda_y = 1.5 \times 2$

Figure 15: Radius of electrode r_e vs. time t for each of the initially biaxial pre-stretches.

3 Discussion

The contour plots of principal stretches, seen in figures 9, 11 and 13, all show clear inhomogeneous deformations. As expected, this effect is largest in the actuated area. The figures also reveal that the thin graphite coated lines connected to the electrode area influence the stretch fields. At these relatively low levels of pre-stretch, small wrinkles at the boundary between the active and passive part are visible, see especially contour plots of λ_1 and λ_2 in figures 9(c), 9(f), 11(c), 11(f), 13(c) and 13(f).

The tests reveal the major principal stretches to be oriented in the circumferential direction of the plane even though the circumferential and radial principal stretches have roughly the same magnitude. However, within the area of the electrode the principal directions are slightly different and seem to be more aligned with the x- and y-directions, cf. contour plots in figures 9(c), 11(c) and 13(c).

The radial profiles in figures 10, 12 and 14 illustrate the evolution of the inhomogeneous deformation over time, both within the electrode as well as at the boundary between the active and passive part of the actuator. The largest differences are found in the interface between the active and passive part, but it is clear that the electrode areas also shows inhomogeneous deformations. The effect of the interface is most pronounced for the principal stretch λ_2, seen in figures 10(b), 12(b) and 14(b), where deformation goes from tensile to compressive over a small change in radius. The compressive deformations are also evident in the contour plots considering λ_2 in figures 9, 11 and 13 and could be one of the triggers for the existence of small wrinkles.

For a non equi-biaxial pre-stretch, represented in figures 13, 14 and 15(c), the response shows a direction dependence. From figures 13(d)-(f), which consider the principal stretch λ_1, a slightly elliptical mode is revealed. The major principal stretches, here determined to be in the circumferential direction, are largest in the direction of highest pre-stretch, and the radial stretches are largest in the direction of lowest pre-stretch. For the radial profiles, seen in figure 14, two different radial profiles are plotted in each subfigure. The two profiles represent the response in two orthogonal directions aligned with the directions of the pre-stretch. The difference is largest for the principal stretches λ_1 and λ_2, see figures 14(a) and 14(b) respectively, and for $10 < r < 30$ mm.

As become evident from figure 15, the viscous effects are largest directly after

application of the load. However, for the combinations of pre-stretch and difference in electric potential investigated in this paper, figures 15(a)-(c) indicate that creep is present, even after 15000 seconds.

4   Summary

The experimental investigations reported in this work include both uniaxial cyclic tests and electro-mechanical tests with full-field measurements of deformation. Combined, they provide a basis for calibration of constitutive models of acrylic-based actuators. The uniaxial tests can be used for calibration of the purely mechanical and time-dependent responses. The use of full-field measurements allows the heterogeneous responses of electro-actuation of samples to be captured and could be used for validation of coupled electromechanical finite element simulations. A comparison of the uniaxial cyclic tests performed here with similar investigations found in the literature revealed that the results showed the same overall behaviour of stress softening and hysteresis. Results from the three-dimensional surface DIC analysis enabled spatially-resolved measurements of the thickness change during electric loading of biaxially pre-stretched VHB 4910 specimens. Previously thickness measurements have been lacking from reported experiments on electro-actuation of such materials. The inhomogeneity of the deformation observed at the interface between the active and passive part of the specimen indicates that conventional measuring techniques, such as an extensometer, are insufficient to understand the deformation processes. Furthermore, from the measured out-of-plane deformation it is possible to resolve the surface shape during loading which will be particularly helpful when studying complex behaviours connected to instabilities, such as wrinkling and pull-in phenomena.

Acknowledgements

References

Biggs, J., Danielmeier, K., Hitzbleck, J., Krause, J., Kridl, T., Nowak, S., Orselli, E., Quan, X., Schapeler, D., Sutherland, W., Wagner, J., et al., 2013. Electroactive polymers: developments of and perspectives for dielectric elastomers. Angew. Chem. Int. Edit. 52 (36), 9409–9421.

Blum, M., Büeler, M., Grätzel, C., Giger, J., Aschwanden, M., 2012. Optotune focus tunable lenses and laser speckle reduction based on electroactive polymers. Proc. SPIE 8252, 825207–825207–11.

Carpi, F., Anderson, I., Bauer, S., Frediani, G., Gallone, G., Gei, M., Graaf, C., Jean-Mistral, C., Kaal, W., Kofod, G., Kollosche, M., Kornbluh, R., Lassen, B., Matysek, M., Michel, S., Nowak, S., O'Brien, B., Pei, Q., Pelrine, R., Rechenbach, B., Rosset, S., Shea, H., 2015. Standards for dielectric elastomer transducers. Smart Mater. Struct. 24 (10), 105025.

Carpi, F., Frediani, G., Turco, S., De Rossi, D., 2011a. Bioinspired tunable lens with muscle-like electroactive elastomers. Adv. Func. Mater. 21 (21), 4152–4158.

Carpi, F., Kornbluh, R., Sommer-Larsen, P., Alici, G., 2011b. Electroactive polymer actuators as artificial muscles: are they ready for bioinspired applications? Bioinsp. Biomim 6 (4), 045006.

Chiba, S., Waki, M., Wada, T., Hirakawa, Y., Masuda, K., Ikoma, T., 2013. Consistent ocean wave energy harvesting using electroactive polymer (dielectric elastomer) artificial muscle generators. Appl. Energ. 104, 497–502.

Correlated Solutions, 2010. Vic-3D Testing Guide. www.correlatedsolutions.com.

Graf, C., Maas, J., 2012. Acoustic transducer based on dielectric elastomers. Proc. SPIE 8340, 83401G–83401G–11.

Hays, M. R., Hart, A., Guettler, A., Ukeiley, L., Oates, W. S., 2016. Fluid–structural dynamic characterization of an electroactive membrane wing. J. Intel. Mat. Syst. Str. 27 (11), 1510–1522.

Hays, M. R., Morton, J., Dickinson, B., Chakravarty, U. K., Oates, W. S., 2013. Aerodynamic control of micro air vehicle wings using electroactive membranes. J. Intel. Mat. Syst. Str. 24 (7), 862–878.

Hosoya, N., Baba, S., Maeda, S., 2015. Hemispherical breathing mode speaker using a dielectric elastomer actuator. J. Acoust. Soc. Am. 138 (4), EL424–EL428.

Hossain, M., Vu, D. K., Steinmann, P., 2012. Experimental study and numerical modelling of VHB 4910 polymer. Comp. Mater. Sci. 59, 65–74.

Hossain, M., Vu, D. K., Steinmann, P., 2015. A comprehensive characterization of the electro-mechanically coupled properties of VHB 4910 polymer. Arch. Appl. Mech. 85 (4), 523–537.

Huang, J., Shian, S., Diebold, R. M., Suo, Z., Clarke, D. R., 2012. The thickness and stretch dependence of the electrical breakdown strength of an acrylic dielectric elastomer. Appl. Phys. Lett. 101 (12).

Jiang, L., Betts, A., Kennedy, D., Jerrams, S., 2015. Investigation into the electromechanical properties of dielectric elastomers subjected to pre-stressing 49, 754–760.

Kofod, G., Sommer-Larsen, P., Kornbluh, R., Pelrine, R., 2003. Actuation response of polyacrylate dielectric elastomers. J. Intel. Mat. Syst. Str. 14 (12), 787–793.

Kollosche, M., Kofod, G., Suo, Z., Zhu, J., 2015. Temporal evolution and instability in a viscoelastic dielectric elastomer. J. Mech. Phys. Solids 76, 47–64.

Kornbluh, R. D., Pelrine, R., Pei, Q., Oh, S., Joseph, J., 2000. Ultrahigh strain response of field-actuated elastomeric polymers. Proc. SPIE 3987, 51–64.

Kornbluh, R. D., Pelrine, R., Prahlad, H., Wong-Foy, A., McCoy, B., Kim, S., Eckerle, J., Low, T., 2011. From boots to buoys: promises and challenges of dielectric elastomer energy harvesting. Proc. SPIE 7976, 797605–797605–19.

Pelrine, R., Kornbluh, R., Pei, Q., Joseph, J., 2000. High-speed electrically actuated elastomers with strain greater than 100%. Science 287 (5454), 836–839.

Sahu, R. K., Patra, K., 2016. Rate-dependent mechanical behavior of VHB 4910 elastomer. Mech. Adv. Mater. Struc. 23 (2), 170–179.

Shian, S., Diebold, R. M., Clarke, D. R., Apr 2013. Tunable lenses using transparent dielectric elastomer actuators. Opt. Express 21 (7), 8669–8676.

Wang, Q., Tahir, M., Zhang, L., Zhao, X., 2011. Electro-creasing instability in deformed polymers: experiment and theory. Soft Matter 7, 6583–6589.

Zhao, X., Wang, Q., 2014. Harnessing large deformation and instabilities of soft dielectrics: Theory, experiment, and application. Appl. Phys. Rev. 1 (2).